Design and Engineering of Slippery Liquid-Infused Porous Surfaces by LbL Technique for Icephobic Surfaces and Hydrodynamic Cavitation

by

ARAZ SHEIBANI AGHDAM

Submitted to the Graduate School of Engineering and Natural Sciences

in partial fulfillment of the requirements for the degree of

Doctor of Philosophy

Sabanci University

Fall 2020

Design and Engineering of Slippery Liquid-Infused Porous Surfaces by LbL Technique for Icephobic Surfaces and Hydrodynamic Cavitation

APPROVED BY:

[redacted]

[redacted]

[redacted]

[redacted]

DATE OF APPROVAL:

ABSTRACT

Design and Engineering of Slippery Liquid-Infused Porous Surfaces by LbL Technique for Icephobic Surfaces and Hydrodynamic Cavitation

ARAZ SHEIBANI AGHDAM

Materials Science and Nano-Engineering, Ph.D. Thesis 2020
Dissertation Supervisor: Prof. Dr. Fevzi Çakmak Cebeci

Keywords: SLIPS, Layer-by-Layer Assembly, Icephobic Surfaces, Cavitation on SLIPS

Abstract:

In this thesis a phenomenon that had been observed in nature and has been explained by fluid dynamics and surface engineering, was mimicked to study its properties and potential applications. The slippery liquid-infused porous surfaces (SLIPS) technology, which is inspired by pitcher plant, has been developed using Layer-by-Layer (LbL) assembly technique. The roughness of the surface was provided by deposition of a thin film of silica nanoparticles on a substrate and then the porosities of the surface was filled by a lubricant to have a non-stick, ultra-repellent, self-healing, icephobic and hydrophobic SLIPS.

The charged silica nanoparticles with a diameter range of 40 to 80nm were synthesized using Stöber method and their size and surface charge were adjusted by controlling the TEOS/Ammonia ratio. The synthesized silica nanoparticles were deposited on the surface of the substrate using LbL assembly technique via dip coating and fluidic coating methods. The SEM, AFM, UV-Vis and

ellipsometry results confirmed the deposition of a rough coating with root mean square roughness of 30 to 15nm, young modules of 5.3Gpa, 98% transparency in visible region and thickness of 100 to 200 nm. The icephobic porosities of the assembled thin films, which were filled by a lubricant were evaluated using a homemade ice adhesion strength measurement setup in an environmental chamber. The ice adhesion strength of the prepared SLIPS was measured as less than 5kPa. The cycling and aging tests, which were carried out on the SLIPS showed 35% reduction in the icephobicity of the SLIPS after 100 days and the ice adhesion strength of the coatings was about 5 times lower than untreated samples even after 50 icing deicing cycles.

Surface topography and properties have an important influence on the generation of cavitating flow in microscale. For studying the effect of SLIPS and the surface roughness on the cavitating flow, the designed SLIPS structure was layer-by-layer assembled using fluidic method on the hydrodynamic cavitation microchips with various hydraulic diameters. The microfluidic devices were exposed to upstream pressures varying from 1 to 7.23 MPa and it has been observed that the inception of the cavitating flow and supercavitation condition have been occurred at much lower pressures in comparison with non-treated microfluidic devices. Introducing the cellulose nanofiber-stabilized perfluoropentane droplets to the SLIPS assembled micro channels, reduced the upstream pressure down to 1.7 MPa for generation of the supercavitation flow pattern within the device. The cellulose nanofibers were assessed by AFM after the cavitation process and it was observed that they were left undamaged during the cavitation process due to the lower upstream pressure, which in turn, increased the regeneration potential of the droplets for closed-loop applications.

ÖZET

Buzfobik Yüzeyler ve Hidrodinamik Kavitasyon için LbL Tekniği ile Kaygan Sıvı Doldurulmuş Gözenekli Yüzeylerin Tasarımı ve Mühendisliği

ARAZ SHEIBANI AGHDAM

Malzeme Bilimi ve Nano-Mühendislik, Doktora Tezi 2020

Tez Danışmanı: Doç. Dr. Fevzi Çakmak Cebeci

Anahtar Kelimeler: SLIPS, Tabaka tabaka kaplama, Buzfobik Yüzeyler, SLIPS Üzerinde Kavitasyon

Özet:

Bu tez kapsamında yapılan çalışmalar, doğada gözlemlenen, yüzey mühendisliği ve akışkanlar dinamiği ile incelenerek açıklanabilen bir olayın, özelliklerinin ve potansiyel uygulamalarının ortaya çıkarılması için incelenmesi ve taklit edilerek çalışılmasını üzerinedir. Sürahi bitkisinden esinlenilerek hazırlanmış, kaygan sıvı doldurulmuş gözenekli yüzey (SLIPS) teknolojisi, tabaka tabaka (LbL) ince film kaplama tekniği kullanılarak geliştirilmiştir. Yüzeyin pürüzlülüğü, ince bir silika nanoparçacık filminin bir altlık üzerine birikilmesiyle elde edilmiştir ve ardından oluşturulan yüzeyin gözenekleri, yapışmaz, itici, kendi kendine düzenlenebilen, buzfobik ve hidrofobik SLIPS mimarisini oluşturmak için bir yağlama maddesiyle doldurulmuştur.

Çapı 40 ila 80 nm arasında değişen negatif yüklü silika nanoparçacıklar Stöber yöntemi kullanılarak sentezlenmiştir ve TEOS / amonyak oranı kontrol edilerek boyutları ve yüzey yüklerinin miktarı kontrol edilmiştir. Sentezlenen silika nanoparçacıklar, daldırmalı kaplama ve akışkan kaplama yöntemleri ile LbL ince-film kaplama tekniği kullanılarak altlığın yüzeyinde biriktirilmiştir. SEM, AFM, UV-Vis ve elipsometri sonuçları, elde edilen ince filmlerin yüzey pürüzlülüğünün 30 ila 15 nm arasında olduğu, Young modül değerinin 5,3Gpa, görünür bölgede %98 geçirgenlik ve 100 ila 200 nm kontrol edilebilen bir kalınlığa sahip bir kaplamanın elde edildiğini gösterilmiştir. Bir yağlayıcı ile doldurulmuş gözenekli ince film kaplamaların buzfobik özellikleri kendi yaptığımız çevresel koşullandırma kabini içinde bir buz yapışma mukavemeti ölçüm düzeneği kullanılarak değerlendirilmiştir. Elde edilen SLIPS mimarisinin buz yapışma mukavemeti 5 kPa'dan az olarak elde edilmiştir, belirtilen değer literatüre göre oldukça iyidir. SLIPS üzerinde gerçekleştirilen döngü ve yaşlandırma testleri, 100 gün sonra SLIPS'nin buz fobisite özelliklerinde %35'lik bir azalma göstermiştir ve kaplamaların buz yapışma mukavemeti, 50 buz çözme döngüsünden sonra bile referans test örneklerden yaklaşık beş kat daha düşüktür. Yağlayıcının tekrarlanmasıyla başlangıçtaki özellikler tekrar elde edilmiştir.

Yüzey topografyası ve özellikleri, mikro ölçekte kavitasyonlu akış oluşumunda önemli bir etkiye sahiptir. SLIPS ve yüzey pürüzlülüğünün kavitasyon akışı üzerindeki etkisini incelemek için tasarlanan SLIPS yapısı, çeşitli hidrolik çaplara sahip hidrodinamik kavitasyon mikroçipleri üzerinde akışkan yöntem ile tabaka tabaka kaplama yöntemi kullanılarak elde edilmiştir. Mikroakışkan cihazlar, 1 ila 7.23 MPa arasında değişen yukarı akış basınçlarına maruz bırakılmıştır ve kavitasyonlu akış ve süper kavitasyon durumunun başlangıcının, işlem görmemiş mikroakışkan cihazlara kıyasla çok daha düşük basınçlarda meydana geldiği gözlenmiştir. Selüloz nanofiberle stabilize edilmiş perfloropentan damlacıklarının mikro kanallarda SLIPS yapısının oluşturulmasıyla, cihaz içinde süper kavitasyon akış modelinin elde edilmesi için yukarı akış basıncını 1.7 MPa'ya kadar düşürüldüğü tespit edilmiştir. Selüloz nanolifler kavitasyon işleminden sonra AFM kullanılarak incelenmiş ve daha düşük giriş basıncı nedeniyle kavitasyon sürecinde hasarsız oldukları görülmüştür, elde edilen sonuçlar kapalı döngü uygulamalarında damlacıkların rejenerasyon potansiyelini artırdığı görülmüştür.

To my father whose determination is as strong as the mountain,
To my mother whose heart is as vast as the ocean,
To my sister whose support is as much as a shining sun,
To my brother-in-law whose courage is as high as the blue sky,
, And to *Pamir* whose dreams are as deep as life

ACKNOWLEDGMENTS

I would like to express my sincere gratitude to my advisor, Professor Fevzi Çakmak Cebeci, for the continuous support of my Ph.D. and related studies, for his guidance, encouragement and immense knowledge. Thank you for being an inspiration and a role model for the rest of my life.

Very special thanks go to Dr. Morteza Ghorbani and Prof. Dr. Ali Koşar for their patient guidance, encouragement and excellent advises throughout the research.

I am truly grateful to my parents, sister, brother-in-law, little Pamir, Homa khala and her husband Mr. Rezgi for supporting me spiritually when the times got rough throughout my PhD and my life in general.

I would also like to thank my lab mates Dr. Esin Ateş Güvel, Dr. Yonca Belce, Zeki Semih Pehlivan, Melike Barak, and Deniz Köken, for all the fun we had while struggling with experiments and thanks to all my beloved friends, Dr. Vahid, Sajjad, Kaveh, Sanaz, Tamay, Pouya, Golnaz, Shahrzad, Maryam, Nilufar, Ali and Nilufar, which your friendship made my life a wonderful experience.

Table of Contents

ABSTRACT iv

ÖZET vi

ACKNOWLEDGMENTS ix

Table of Contents x

List of tables xiii

List of Figures xiv

Introduction and State of Art 1

1 Chapter One 3

- 1-1 Introduction 4
- 1-2 Experiments 7
  - 1-2-1 Materials 7
  - 1-2-2 Synthesizing nanoparticles 7
  - 1-2-3 DLS and Zeta potential measurements 7
- 1-3 Results and discussion 8
- 1-4 Conclusion 10
- 1-5 References 10

2 Chapter Two 12

- 2-1 Abstract 13
- 2-2 Introduction 13
- 2-3 Experimental section 17
- 2-4 Results and discussion 20
- 2-5 Conclusions 36

2-6 References 37

3 Chapter Three 42

3-1 Abstract 43

3-2 Introduction 43

3-3 Methods and Materials 46

3-3-1 Methods and materials for creating SLIPS 46

3-3-2 Experimental Procedure and Configurations 48

3-3-3 Characterization 50

3-4 Results and discussion 50

3-4-1 Surface properties 50

3-4-2 The effect of the SLIPS and LBL assembled silica nanoparticles on the inception of the cavitation phenomenon 53

3-4-3 The effect of the LbL assembled SLIPS on the development of the cavitating flow 59

3-5 Concluding 65

3-6 References 65

4 Chapter Four 68

4-1 Introduction 70

4-2 Methods and Materials 71

4-2-1 Fabrication of the microfluidics device 71

4-2-2 Surface Modifications of the device 72

4-2-3 Preparation of Cellulose nanofibers (CNFs) 73

4-2-4 Preparation of CNF-stabilized PFC5 droplets 73

4-3 Characterization 73

4-3-1 Atomic force microscopy (AFM) 73

4-3-2 Scanning electron Microscopy (SEM) 74

4-3-3 Ellipsometry measurements 74
4-3-4 Contact angle measurements and contact angle hysteresis 74
4-3-5 Cavitation experiments 74
4-4 Results and Discussion 75
4-4-1 Surface modification by layer-by-layer (LBL) assembled silica nanoparticles 75
4-4-2 Assembly of CNF-stabilized PFC5 droplets 77
4-4-3 Hydrodynamic cavitation measurements 78
4-5 Conclusions 84
4-6 References 85
5 Chapter Five 88
5-1 Conclusion 89
5-2 Outlook 91
5-3 Research Outcomes 93

List of tables

Table 2-1. Measured silica nanoparticle sizes by DLS and SEM when [TEOS]/[NH3]aq ratio was varied during nanoparticle synthesis 20
Table 2-2. Structure and nanoparticle size of thin films 22
Table 2-3. AFM surface topography at the nano- and microscale 23
Table 2-4. The thickness and void fraction of thin films measured using ellipsometry 26
Table 2-5 Nanomechanical properties of thin films 27
Table 2-6. Weibull parameters of thin films 29
Table 2-7. AWCA and WCAH of substrates and thin films 32
Table 2-8 Weibull parameters of thin films for different aging periods 33
Table 2-9 Weibull parameters of thin films for different iced/deiced cycles 35
Table 3-1 The detailed properties of the microfluidic devices 49
Table 3-2 DLS size and Zeta potential of synthesized and mixed silica nanoparticles 52
Table 4-1 Dimensions for the different parts of the microfluidic devices 72

List of Figures

Figure 1-1 The mechanism of silica nanoparticles growth 5

Figure 1-2 Average diameter of particles as a function of bath temperature [11] 6

Figure 1-3 Zeta potential of silica nanoparticles in different pHs [14] 6

Figure 1-4 Size changes of silica nanoparticles with the ratio of the TEOS/Ammonia 9

Figure 1-5 SEM images, number distribution of DLS measurments and Zeta petential of the a) Silica nanoparticles with diameter of 45nm b) Silica nanoparticles with diameter of 70nm c) Silica nanoparticles with diameter of 100nm. All the scale bars are 200nm. 9

Figure 1-6 Size changes of nanoparticles in the baths with different TEOS/Ammonia ratios by time 10

Figure 2-1 Chemical structure of SPS, PAH and SiO_2 18

Figure 2-2 Schematic representation of LbL deposition of different polyelectrolytes and nanoparticles on the surface for creating a rough tetralayer thin film structure. 18

Figure 2-3 Ice mold, substrate and ice holder of the home-built icephobicity test setup 20

Figure 2-4 SEM image of silica NPs A-N1 (38.6 nm), B-N2 (67.9 nm), C-N3 (83.7 nm), D-N1&N3 (a mixture of 38.6 nm and 83.7 nm) silica nanoparticles. All scale bars are 200 nm. 21

Figure 2-5 SEM images of A-(PAH||SPS)5||(PAH||NP)10 architecture using 38.6 nm silica nanoparticles B-(PAH||SPS)5||(PAH||NP)10 architecture using 83.7 nm silica nanoparticles: all scale bars are 200 nm 23

Figure 2-6 SEM images of A- ((PAH||SPS)5||(PAH||NP)10)2 architecture using 38.6 nm silica nanoparticles, B-((PAH||SPS)5||(PAH||NP)10)2 architecture using 83.7 nm silica nanoparticles 4, C-((PAH||SPS)5||(PAH||NP)10)2 architecture using (1:1) mixture of 38.6 nm and 83.7 nm silica nanoparticles. All scale bars are 200 nm. 25

Figure 2-7 AFM images of A-Glass, B-((PAH||SPS)5||(PAH||NP)10)2 architecture using (1:1) mixture of 38.6 nm and 83.7 nm silica nanoparticles 26

Figure 2-8 Temperature changes of the refrigerator and different surfaces by time 29

Figure 2-9 Weibull distribution of the ice adhesion strength of substrates and modified surfaces. 29

Figure 2-10 UV-Vis transmittance of Glass+S5+PFDTS+Fomblin Oil+PFDTS 32

Figure 2-11 Weibull distribution of the ice adhesion strength of the aged samples for 5, 10, 20, 50 and 100 days. 33

Figure 2-12 Change in ice adhesion strength of σ_o by ageing 34
Figure 2-13 Weibull distribution of the ice adhesion strength of the cyclic iced/deiced samples for 5, 10, 20, 50 cycles 35
Figure 3-1 a-Peristatic pump and a home-made Polyelectrolyte Distributer System (PDS) b-schematic of Layer by Layer assembled polyelectrolytes and nanoparticles 47
Figure 3-2 SEM and AFM images of synthesized silica nanoparticles and layer by layer assembled D2 channel a-40nm NPs b-80nm NPs c-layer by layer assembled D2 coating d- AFM height image of D2 coating 52
Figure 3-3 The qualitative comparison of the inception of cavitation phenomenon inside the regular microchannels with state-of-the–art design (D1) and SLIPS enhanced one (D3) 55
Figure 3-4 The inception inside CH7 and the enhancement demonstration with SLIPS and LBL silica nanoparticles and the water contact angle of the channel a- hydrophilic surface of D1 coating b- hydrophobic surface of D2 coating c- hydrophobic surface of the D3 coating and thin layer of lubricant covering the droplet 56
Figure 3-5 Cavitation inception in the extended channel for the smaller microchannels (CH5 and 6) enhanced by D3 and the comparison with the corresponding extended channel for the larger microchannel 57
Figure 3-6 The variations in pressure at the location of vena contracta (P2) and Reynolds number for the cases of D1 and D3 at cavitation inception for different microchannels (X stands for the number of the channels) 58
Figure 3-7 The comparison in the supercavitation flow regime inside different microchannels for the D3 coating with plain D1 microchannels 60
Figure 3-8 The flow rate variations in CH1 and CH5 as a function of pressure drop 61
Figure 3-9 The cavitating flow patterns inside the microchannel and extended channel of the CH7 device for the configuration D1 and D2 and D3 coatings 61
Figure 3-10 The variations in cavitation number as a function of vapor volume fraction in different microchannels for the D1 and D3 devices 64
Figure 3-11 Comparison in the flow regimes inside CH7 at different upstream pressures for the D1, and D2 and D3 coatings 64
Figure 4-1 Assembly of the microfluidics device. Schematic overview of (A) fabrication process flow for the microfluidic device (B) assembled layers of thin film on the microfluidic device and

SEM image of the final thin film (C) 2D and 3D height images of atomic force microscopy representing the nano and microscale roughness of the surface. 76

Figure 4-2 Assembly of the CNF-stabilized PFC5 droplets. Particle stabilized droplets were prepared by (A) mixing a CNF suspension in MilliQ water with PFC5 to obtain the CNF stabilized droplets. (B) Light microscopy image of the resulting CNF-stabilized PFC5 droplets (imaged ca.1 h after preparation). Droplets were deposited and dried at ambient conditions and imaged using (C) AFM and (D) SEM. 77

Figure 4-3 The cavitating flow patterns inside the same microchannel (CH1). (A) supercavitation flow pattern at upstream pressure of 1.7 MPa for the case of PFC5 droplets in water (B) developed cavitating flow at upstream pressure of 7.23 MPa for the case of water. 79

Figure 4-4 The cavitating flow patterns inside the same microfluidic device (CH1). (A) penetration of twin cavities to the extended channel with a view of the microchannel downstream at the upstream pressure of 2.3 MPa for the case of PFC5 droplets (B) penetration of twin cavities to the extended channel at the upstream pressure of 2.3 MPa for the case water. 80

Figure 4-5 Cavitation patterns for PFC5 droplets in two different microfluidics devices (CH1 and CH2). The variation of Reynolds and Weber numbers as a function of the cavitation number for the cavitating flow with CNF-stabilized PFC5 droplets. Snapshots of the corresponding flow patterns at points A, B and C of the different curves are included. 82

Figure 4-6 The fate of the PFC5 droplets during supercavitation. Bubble radius variations at the upstream pressure of 1.67 MPa inside the extension with shock wave manifestation. The microfluidic device, CH1, was used. 83

Figure 4-7 CNFs before and after supercavitation. AFM image of CNF (A) before and (B) after supercavitation. 84

Figure 5-1 The trapping of air toward the walls of the tube and wrapping by the lubricant of the SLIPS 91

Figure 5-2 Schematic illustration of the mechanism of bubble separation and conduction process 92

Introduction and State of Art

Slippery liquid-infused porous surfaces (SLIPS), which are mimicked from pitcher plant, have been recently introduced as a potential solution for different applications. Many scientists have been inspired by the capabilities of these surfaces and have tried to harness their advantages by engineering the surface of substrates. The main objective in the engineering of the substrate's surface is preparing the substrate to entrap a proper lubricant on its surface. In this regard, extensive works have been carried out to modify the chemical and physical properties of the surface to be adapted for entrapping the lubricant. However, it should be noted that most of the techniques that have been exploited for this purpose are limited to the characteristics of the substrate, unscalable, complicated manufacturing process, and etc. In this dissertation, it has been attempted to address these problems and investigated a simple approach for applying a thin film to stabilize the desired lubricant on the surface of the substrate with a low dependency on the substrate's material using layer-by-layer technique.

In the first chapter of the dissertation, silica nanoparticles with a wide range of diameter have been synthesized and characterized. Different diameters of the nanoparticles with a negative surface zeta potential have been synthesized by changing the chemical ratios of the bath's components. These nanoparticles are prepared to be deposited on the substrate and create a rough surface to entrap the desired lubricant within its porosities. Characterization and optimization of the diameter and the surface charge of the silica nanoparticles have improved the mechanical properties of the deposited thin film and its efficiency in stabilization of the lubricant.

In the second chapter, which have been published in Langmuir journal, the prepared silica nanoparticles have been assembled on the glass and silicon wafer substrates using the dip-coating method of layer-by-layer assembly technique. The surface of glass and silicon wafer can be hydrolyzed in an aqueous media and generate partially charged regions for attracting the oppositely charged polyelectrolytes and nanoparticles. However, the negatively charge silica nanoparticles cannot be absorbed on the negatively charges glass and silicon wafer. In the meantime, the density of the charge on the surface of the substrate is not strong enough to absorb and stabilize the silica nanoparticles on the surface. For reducing the dependency of the thin film deposition's efficiency on the substrate's material, an adhesion layer has been anticipated to increase the surface charge density of the substrate and provide an attractive layer for deposition of the synthesized silica nanoparticles. The surface assessments of the thin film, which have been carried out using scanning electron microscopy (SEM), atomic force microscopy (AFM), ellipsometry and many other devices, confirmed the needed porosity for entrapping the lubricant within the surface of the thin film. By modifying the surface affinity of the thin film, a fluorinated lubricant has been entrapped within the porosities of the assembled thin film and SLIPS have been achieved and the icephobicity of theses thin films and their durability have been investigated thoroughly in this chapter.

In the third and fourth chapter, which are published in scientific reports and chemical engineering journals respectively, the simplicity of deposition technique and the independency of the method to the geometry of the substrate were challenged. In these chapters the thin film has been layer-by-layer assembled using fluidic coating method on the surface of the silicon wafer microchips, which is impossible or too complicated to modify its surface using other well-known techniques and methods. The carved channels of the microfluidic device on silicon wafers were covered using glass anodic bounding and the surface of the channels was not exposed to the environment to apply and surface modification processes. It has been shown that layer-by-layer technique can deposit a thin film on the surface of the microfluidic device by a very simple approach without removing the anodic bounded glass cover. The impact of the deposited SLIPS on the hydrodynamic cavitation properties of the microfluidic devices has been investigated in these chapters.

The proposed dip coated layer-by-layer assembled SLIPS in this thesis have presented a durable and transparent icephobic surfaces with a nanometric thickness, which are less dependent on the material of the substrate, and are able to be deposited on any partially charged surfaces. Additionally, the deposition of the layer-by-layer assembled SLIPS using fluidic coating method have revealed the simplicity of the method for applying the thin films on the geometrically complicated surfaces and channels. The reported results, have shown an outstanding performance in generation of the cavitating flow at lower upstream pressure and preservation of the cavitating bubbles.

Chapter One

Synthesis and Characterization of the Silica Nanoparticles

1-1 Introduction

Silica nanoparticles have been attracted the interest of the research groups in recent decades base on their unique and outstanding properties. These nanoparticles are transparent in a wide range of optical wave lengths, chemically stable and unreactive, mechanically durable and stable, and fairly not harmful or toxic to living tissue. In addition to these properties, they are synthesized and functionalized in rather simple procedures which can develop different and amazing chemical and physical properties on the surface of the particles [1]. Functionalizing the particles alters the chemistry and affinity of the surface which allows the scientists to load different chemicals on the particles for studying the surface properties in biomedical applications. Meanwhile the dispersion and size control of the nanoparticles in various solutions can be engineered as a consequence of surface modification of the nano particles. However, the uptake hazards and risks of these particles and functionalizing groups by animals, plants and human beings are not studied thoroughly and need to be investigated further [2].

There are various approaches introduced to synthesis silica nanoparticles for different applications. Size distribution, surface zeta potential, mesoporosity, mechanical properties, dispersant solution and many other factors can affect the selection of appropriate synthesizing approach. The sol-gel process and microemulsion method can basically be considered as the most well-defined and widespread methods to produce wide size range of silica nanoparticles [3, 4].

Microemulsions (MEs) are liquid systems of oil, water, and amphiphile components which are isotropic transparent in most of the cases [5]. Depending on the components of the systems, they can be divided in three main different categories as water-in-oil in which the oil phase in the system is dominant as the internal phase, oil-in-water, which oily phase is the continuous one in the system and bicontinuous water and oil in which there are comparable amounts of water and oil in the system. MEs are developed by blending the aqueous and oily phase in the presence of proper surfactant. The phase behavior of the developed ME system is determined by the relative proportions of the oil, water, and amphiphile components in which the low surface tension achieved by the surfactant, can result in spontaneous transformation into ME[6-8] In the case of silica nanoparticles, ME has been investigated extensively in the recent decade. The surfactant helps the oil and water to be dispersed in the media and the hydrolysis reaction takes place at the interface of the oil and water.[9]

Stöber process has been reporter by Werner Stöber and his colleges in 1968 and is used as one the most practical and simple wet chemistry approaches to synthesis silica nanoparticles. In this process, which is a subset of sol-gel process, a precursor is introduced to an alcoholic solution to react with water. The hydrolyzed precursors lose the EtOH group on their structure and link together to create bigger molecules and finally build the silica particles as shown in Figure 0-1[10]. The synthesized particles using this method are uniform and have a narrow size distribution, which can be controlled by the conditions in the bath. The reactants concentration ratio, temperature of the bath, concentration of the catalysts, and reaction time are the most important parameters, which effect the size and distribution of the particles. Adding ammonia to the bath reduces the random directional growth of the particles and spherical particles can be achieved. Increasing the amount of the ammonia concentration in the bath increase the size of the particles however the size distribution of the particles gets wider. The concentration of tetraethyl orthosilicate as precursor effects the particles size inversely. The higher concentration of tetraethyl orthosilicate provides greater amount of nucleation sites in the bath which reduce the size of the synthesized particles and increase the size spread of them as a consequence. The temperature of the bath can determine the size and the distribution of the particles. The lower temperature reduces the reactions rate which in turn leads to increase in the size of the particles (Figure 0-2) [11]. Using Stöber process to generate silica particles grants the advantageous of precisely controlling the size and monodispersity of the synthesized nanoparticles.

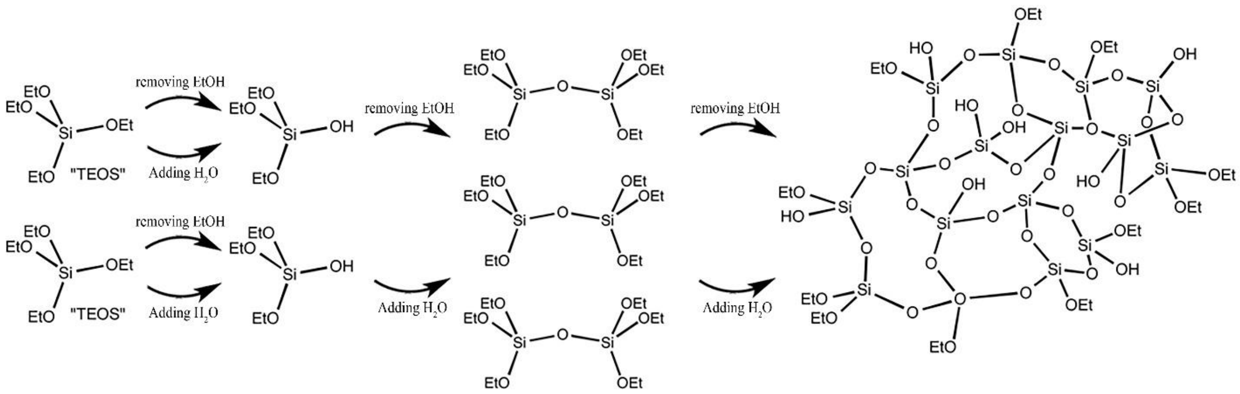

Figure 0-1 The mechanism of silica nanoparticles growth

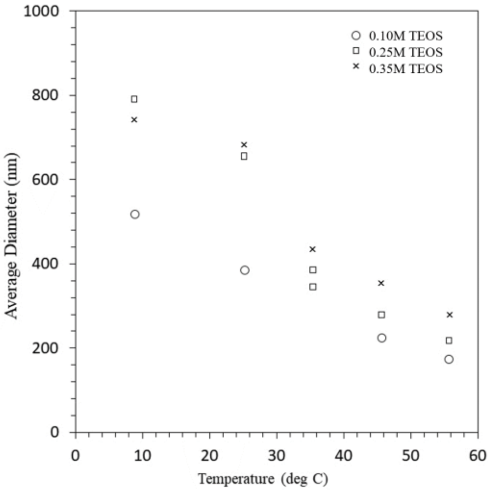

Figure 0-2 Average diameter of particles as a function of bath temperature [11]

Nanoparticles can be protonated or deprotonated in the aqueous solutions and acquire positive or negative charge on the surface respectively [12]. Silanol functional group on the surface of the silica nanoparticles are dissociation with the water molecules and becomes negatively charged [13]. Zeta potential of silica nanoparticles has been studied in the recent literatures. It is reported that these particles possess negative surface charge which is stable in a wide range of pHs (3-13) (Figure 0-3) [14]. High stability and low dependency of surface charges of the silica nanoparticles to the pH of the solution makes them an interesting inorganic particle to be used in layer-by-layer assembly. In this chapter different sizes of silica nanoparticles have been synthesized using Stöber method and the size distribution and zeta potential of them has been studied.

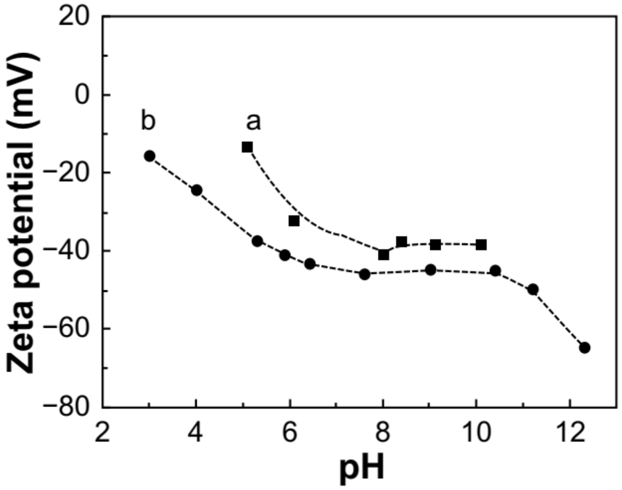

Figure 0-3 Zeta potential of silica nanoparticles in different pHs [14]

1-2 Experiments

1-2-1 Materials

Tetraethyl orthosilicate (TEOS), Ammonia solution 25%, 2-propanol 99.5% (IPA) were purchased from Sigma Aldrich. Deionized water (resistance 18.2 MΩ cm) was obtained using Milli-Q.

1-2-2 Synthesizing nanoparticles

The sol-gel synthesizing the silica nanoparticles carried out at room temperature ($25 \pm 2\ ^{\circ}\mathrm{C}$). Isopropyl alcohol (IPA) was used as the reaction media, Tetraethyl orthosilicate (TEOS) was used as source of silica and 25% Ammonium hydroxide solution in water was used as catalyzer and hydrolyzer. The ammonia hydroxide was mixed with IPA for 15 minutes on a magnetic stirrer and then TEOS was added to the solution. After two hours of stirring, the solution stored without disturbance for 72 hours. The size of nano particles was controlled by changing the ratio of TEOS/NH_4OH.

1-2-3 DLS and Zeta potential measurements

Size distribution of the particles was measured by Dynamic Light Scattering (DLS). DLS measurement reports the size of the nanoparticles in three values of distribution; intensity (I), volume (V) and number (N) distribution. The intensity distribution is related to the amount the light that have been scattered by the particles in each size bin. The volume distribution describes the total volume of the particles which are in the same size bin and the number distribution is related to the number of the available particles in each size bin. In a sample containing two type of particles (a and b) the related distribution of a particle is calculated as follows:

$$\%\mathrm{I_a} = \frac{100.\,\mathrm{N_a a^6}}{\mathrm{N_a a^6 + N_b b^6}}$$

$$\%\mathrm{V_a} = \frac{100.\,\mathrm{N_a a^3}}{\mathrm{N_a a^3 + N_b b^3}} \tag{1-1}$$

$$\%\mathrm{N_a} = \frac{100.\,\mathrm{N_a}}{\mathrm{N_a + N_b}}$$

Where N_a and N_b are the number of the particles with sizes of a and b respectively. The intensity distribution is related to the size of the particles by a factor of six. This means that the intensity distribution emphasizes of the larger particles. In this regard, it is better to work with the number distribution to report the smaller particles in the solution and report the intensity distribution values to emphasis the larger particles in the solution.

1-3 Results and discussion

A wide range of the silica nanoparticles size have been synthesized by changing the ratio of the TEOS/ Ammonia in the IPA medium. By increasing the ratio of the TEOS/Ammonia, the OH^- content of the solution is decreased. Therefore, the TEOS molecules are not hydrolyzed sufficiently to produce silanol monomers by substituting the (-Si-OET) with (-Si-OH). Hydrolyzed TEOS molecules condensates and create a branched siloxane network however the lack of silanol monomers prevent the reaction to go forward and the rate of the growth of the nanoparticles decreases. In the case of lower ratio of the TEOS/Ammonia, silanol monomers are abundant in the solution. These molecules can create a network and grow up by adding new silanol group to the network and the size of the silica nanoparticles increases as result [15]. Figure 0-4 represents the size changes of silica nanoparticles with the ratio of the TEOS/Ammonia. Figure 0-5 represents the SEM images of the nanoparticles with diameter of 100nm,70nm, and 45nm. It should be noted that the reported diameters are the values that have been measured by DLS instrument which is based on the hydrodynamic diameter of the particles. Hydrodynamic diameter of the particles is a little bit larger than the actual sizes of the nanoparticles shown in SEM images.

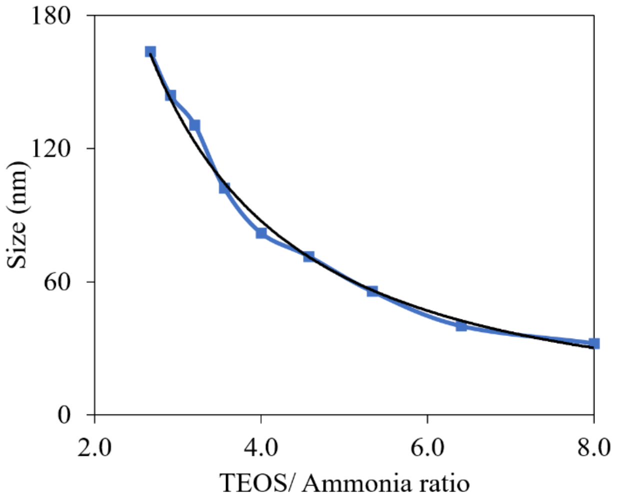

Figure 0-4 Size changes of silica nanoparticles with the ratio of the TEOS/Ammonia

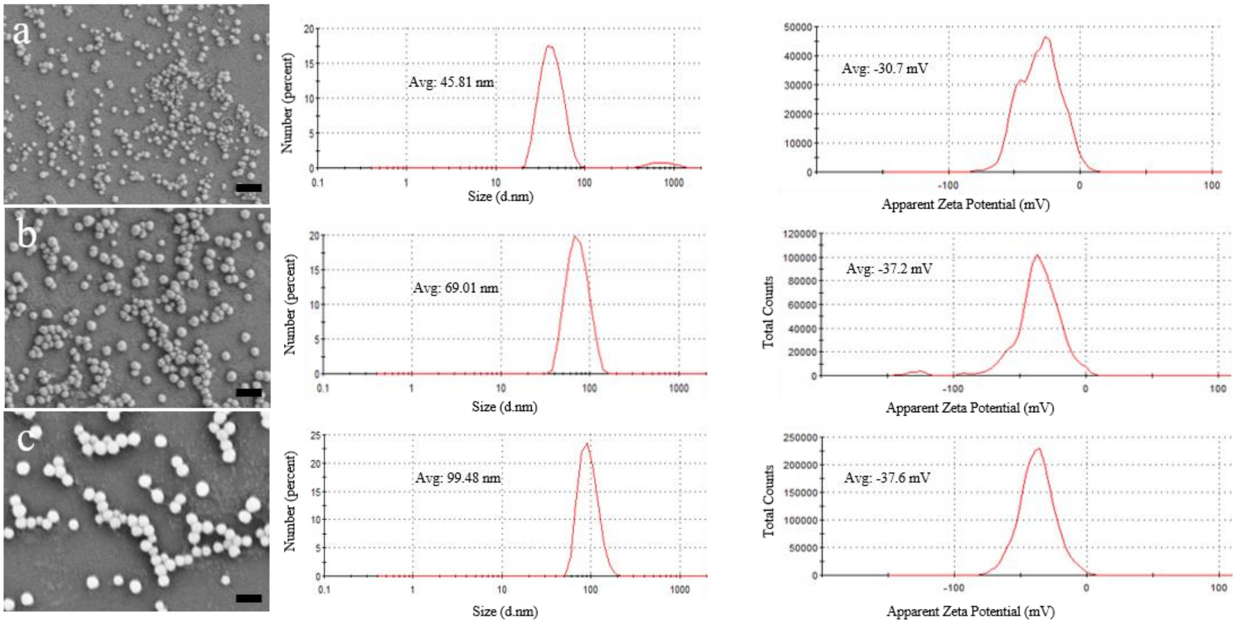

Figure 0-5 SEM images, number distribution of DLS measurments and Zeta petential of the a) Silica nanoparticles with diameter of 45nm b) Silica nanoparticles with diameter of 70nm c) Silica nanoparticles with diameter of 100nm. All the scale bars are 200nm.

For further investigation in the mechanism of synthesizing of the silica nanoparticles, size changes of three test samples were measured, over 2, 6, 24, 48, 72 and 96 hours. As it is reported in Figure 0-6, in less than two hours large particle sizes has been detected in the medium. The size of the particles drops in the first six hours and then it increases to a rather stable diameter in 72 hours.

Han et al. has related the large particle sizes in the first hours of the reaction to the clumps of loosely coalesced small particles. They get denser as the reaction progress and create small nanoparticles, which gradually grow until stabilization of the size [15].

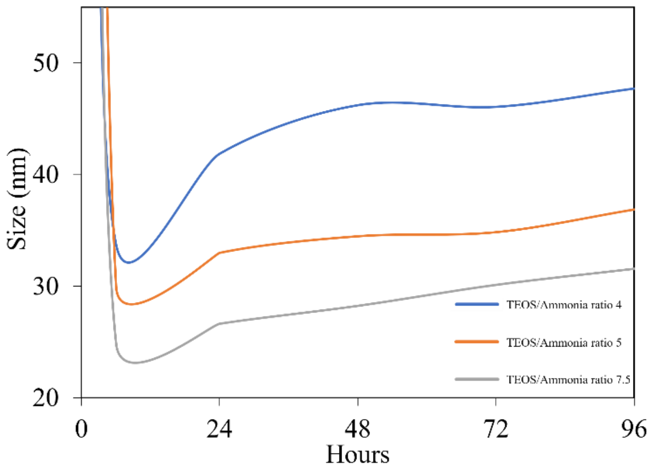

Figure 0-6 Size changes of nanoparticles in the baths with different TEOS/Ammonia ratios by time

1-4 Conclusion

The silica nanoparticles, which are synthesized and characterized in this chapter are assembled on the surface of the substrates via layer-by-layer method to provide the porosities on the surface of the thin film. These porosities are filled using a lubricant to achieve SLIPS surfaces as reported in the upcoming chapters. Among all synthesized silica nanoparticles, the ones with 40 and 80nm diameter was selected to be used in the next chapters. These nanoparticles were prepared in the baths with TEOS/Ammonia ratio of 6.5 and 3.5 and their zeta potential were measured as -24.9 and -35 mV respectively.

1-5 References

1. Graf, C., et al., *Surface Functionalization of Silica Nanoparticles Supports Colloidal Stability in Physiological Media and Facilitates Internalization in Cells*. Langmuir, 2012. **28**(20): p. 7598-7613.
2. Liberman, A., et al., *Synthesis and surface functionalization of silica nanoparticles for nanomedicine*. Surface Science Reports, 2014. **69**(2–3): p. 132-158.

3. van Blaaderen, A. and A. Vrij, *Synthesis and Characterization of Monodisperse Colloidal Organo-silica Spheres.* Journal of Colloid and Interface Science, 1993. **156**(1): p. 1-18.
4. Arriagada, F. and K. Osseo-Asare, *Synthesis of nanosize silica in a nonionic water-in-oil microemulsion: effects of the water/surfactant molar ratio and ammonia concentration.* Journal of colloid and interface science, 1999. **211**(2): p. 210-220.
5. Danielsson, I. and B. Lindman, *The definition of microemulsion.* Colloids and Surfaces, 1981. **3**(4): p. 391-392.
6. Alany, R.G., et al., *Microemulsion systems and their potential as drug carriers*, in *Microemulsions*. 2008, CRC Press. p. 278-323.
7. Lawrence, M.J. and G.D. Rees, *Microemulsion-based media as novel drug delivery systems.* Advanced Drug Delivery Reviews, 2000. **45**(1): p. 89-121.
8. Moulik, S.P. and B.K. Paul, *Structure, dynamics and transport properties of microemulsions.* Advances in Colloid and Interface Science, 1998. **78**(2): p. 99-195.
9. El Maghraby, G.M., M.F. Arafa, and E.A. Essa, *Chapter 33 - Phase transition microemulsions as drug delivery systems*, in *Applications of Nanocomposite Materials in Drug Delivery*, Inamuddin, A.M. Asiri, and A. Mohammad, Editors. 2018, Woodhead Publishing. p. 787-803.
10. Stöber, W., A. Fink, and E. Bohn, *Controlled growth of monodisperse silica spheres in the micron size range.* Journal of Colloid and Interface Science, 1968. **26**(1): p. 62-69.
11. Bogush, G.H., M.A. Tracy, and C.F. Zukoski, *Preparation of monodisperse silica particles: Control of size and mass fraction.* Journal of Non-Crystalline Solids, 1988. **104**(1): p. 95-106.
12. Barisik, M., et al., *Size Dependent Surface Charge Properties of Silica Nanoparticles.* The Journal of Physical Chemistry C, 2014. **118**(4): p. 1836-1842.
13. Behrens, S.H. and D.G. Grier, *The charge of glass and silica surfaces.* The Journal of Chemical Physics, 2001. **115**(14): p. 6716-6721.
14. Kim, K.-M., et al., *Surface treatment of silica nanoparticles for stable and charge-controlled colloidal silica.* International journal of nanomedicine, 2014. **9 Suppl 2**(Suppl 2): p. 29-40.
15. Han, Y., et al., *Unraveling the Growth Mechanism of Silica Particles in the Stöber Method: In Situ Seeded Growth Model.* Langmuir, 2017. **33**(23): p. 5879-5890.

Chapter Two

Tailoring the Icephobic Performance of Slippery Liquid-Infused Porous Surfaces through LbL

Published in Langmuir:

Aghdam, A. S., & Cebeci, F. Ç. (2020). Tailoring the Icephobic Performance of Slippery Liquid-Infused Porous Surfaces through the LbL Method. Langmuir, 36(46), 14145-14154, doi.org/10.1021/acs.langmuir.0c02873.

2-1 Abstract

There has been increasing interest in recent years in identifying an ice-removal procedure that is a low cost, scalable, and consumes a negligible amount of energy, in order to prevent catastrophic failures in outdoor structures. One of the potential solutions to the structural problems caused by frigid and icy conditions is the use of slippery liquid-infused porous surfaces (SLIPS) to effect passive ice removal using easy, economical, and energy-free means. This work takes advantage of highly flexible layer-by-layer (LbL) technology to customize and design surfaces that have a high degree of roughness by using negatively and positively charged polyelectrolytes and negatively charged silica nanoparticles (NPs). SEM (scanning electron microscopy) images represent the silica nanoparticles deposition on the surface of the thin film. The roughness of these thin films has been demonstrated by AFM (atomic force microscopy) investigation. The main characteristics of these surfaces are their high contact angle and low water contact angle hysteresis, which is achieved by the fluorinated lubricant that is infused in the pores of the films. The ice adhesion strength of the thin films was measured using a home-built normal mode tensile test in an environmental chamber, which confirmed the icephobicity of the surface as having an adhesion strength of less than 5kPa, implying that this surface is an excellent candidate for the passive removal of ice. The thin film thin films were aged for up to 100 days, and the results showed that the thin film could reduce the ice adhesion strength by 65%, even after this period. The ice adhesion strength of the thin film after icing/deicing cycles showed that 80% of the icephobicity of the thin film had been preserved even after 50 cycles.

2-2 Introduction

Failures caused by ice are a significant concern [1] in relation to outdoor structures and other advanced complex structures such as aircraft [2], wind turbines [3, 4], ships [5, 6] and power lines [7, 8]. Lowering the performance or causing the breakdown of these systems may result in catastrophic failures. Creating ice-free surfaces with an enhanced lifetime to improve the performance of these structures in relation to specific applications is challenging, and is a topic that has attracted significant interest among scientists.

Standard practices for deicing can be divided into three main approaches: thermal [9], mechanical [10, 11], and chemical [12]. Each of these methods may be time-consuming, expensive and detrimental to the environment, and in some cases cannot be applied to, or may even damage, the surface of the structure and the structure itself [13]. In these practices, researchers have made intensive efforts to develop thin film and surface modifications to increase the freezing time of water droplets on the surface and provide an opportunity for them to be repelled before the formation of ice. In addition, making the surface superhydrophobic and preventing water droplets from penetrating and freezing on the surface is another strategy to create icephobic surfaces [8]. Such activity can thus reduce the ice adhesion strength to a point at which the ice can be removed easily by relying on its weight or the environmental conditions, with no external force required [14].

Liu et al. argued that the formation of frost is delayed on a superhydrophobic surface with a water contact angle of 162 degrees, and the structure of ice is, therefore, weakened enough to be removed from the body easily [15]. Meuler et al. concluded that the icephobicity of fluorodecyl polyhedral oligomeric silsesquioxane (POSS) coatings on smooth surfaces is dependent on the receding contact angle of water on the substrate surface. They proposed that controlling the surface roughness can reduce the ice adhesion strength more effectively [16]. Cao et al. used various sizes of silica nanoparticles in a polymeric texture, and claimed that superhydrophobicity does not guarantee an anti-icing property, and the size of the features on the surface and its morphology should be taken into account [17].

Mimicking the lotus effect by making the surface rough at the nano and micro scale can increase hydrophobicity in the Cassie state and prevent the penetration of water droplets to the surface pores by confining the air between the water and surface [5, 18, 19]. However, investigating such coatings under conditions of high humidity can either downgrade the wetting state to a Wenzel state [20-22] or increase the opportunity for moisture to penetrate the surface, thus enabling the nucleation of ice and making ice removal more difficult [23-25]. On the other hand, the precipitation of fluorinated compounds on smooth surfaces can increase hydrophobicity and icephobicity; however, the durability of the thin films is a prohibitive factor in these instances. One of the most effective strategies for countering freezing conditions is to increase the roughness of the surface and coat it with a thin film of fluorinated compounds to reduce the energy of the surface and enhance the durability of the fluorinated thin film [26].

In recent years, Slippery Liquid Infused Porous Surfaces (SLIPS) has been introduced as an imitation of the way pitcher plants (Nepenthes) construct omniphobic surfaces. These surfaces are scalable and durable at a reasonable cost. However, their applicability on different surfaces, and the transparency of the films, is challenging in most cases [27-29]. Recently, researchers have combined the idea of classical thermal heating with SLIPS surfaces to obtain efficient coatings, and have reported successful icephobic coatings [28, 29]. One of the well-proven approaches to produce SLIPS thin films is the layer-by-layer (LbL) assembly method. LbL has been widely used to customize and design surfaces with nano- and micro-scale roughness on various substrates for different applications, such as hydrophilicity, superhydrophobicity, and omniphobicity [19, 20, 27]. The LbL approach benefits from the electrostatic interactions between oppositely charged molecules to assemble thin films, offering a molecular level control of the structure and thicknesses of the layers [27, 30]. LbL is a simple, low-cost, environmentally benign and scalable technique, and hence applicable to diverse systems, structures and substrates.

The ice adhesion strength of icephobic surfaces has been evaluated using several methods and force-applying modes. These methods can be divided into three main categories: applying shear stress using a force probe, applying shear stress by centrifugal force, and applying normal stress. Some researchers have applied shear stress to measure the strength of ice adhesion to the surface of the sample [31, 32]. On the other hand, both Kulinich & Farzaneh and Janjua et al. took advantage of centrifugal force to detach the ice from the samples. They measured the rotational speed of the specimens and calculated the shear force that had been applied to the ice/substrate interface [33, 34]. Additionally, some researchers have evaluated ice adhesion strength by applying normal stress [35, 36]. Using normal force to detach the ice can simulate the removal of ice by its own weight, and can help to investigate the behavior of ice in real-life conditions. Notably, the movement of ice due to shear stress does not guarantee its removal, and hence the application of normal force can reveal more detail about such an incidence in SLIPS.

A survey of recent studies reveals that superhydrophobic surfaces have been selected as an appropriate strategy to counter icing conditions. However, the degradation of the icephobicity properties of the surface caused by the destruction of the surface roughness during the icing cycles, and the nucleation of the ice crystals from the moisture in the air pockets within the pores, demonstrated the inefficiency of such surfaces in cyclic icing conditions [37, 38]. Employing the LbL technique, rather than other surface modification processes, excludes not only the dependency of the thin film applicability, quality, and performance on the substrate, but also reduces the complexity and cost of the manufacturing process.

All the points mentioned earlier prompted the idea of creating SLIPS icephobic surfaces by taking advantage of the LbL technique to fabricate nano- and micro-controlled rough surfaces by depositing nanoparticles of different sizes and trapping the water-immiscible lubricants within their pores. The nanoscale thickness of the thin film and the simplicity of its application on the surface, regardless of the geometry of the substrate, are the outstanding advantages of using LbL method for creating a stable SLIPS surfaces. By using fluidic LbL deposition technique, we have applied LbL-based SLIPS thin films inside microfluidic channels to obtain cavitating flows for biomedical and energy applications [39-41], which is not easy to achieve by other techniques and methods.

In this study, we selected the LbL method to assemble water-based oppositely charged polyelectrolytes. We embedded different sizes of silica nanoparticles to create a variable surface architecture where the roughness can be customized for the thin-films. The vapor phase deposition of fluorinated silane enhanced the affinity of the surface to the lubricant and provided a better bed for trapping it. Filling the surface porosity with polymeric fluorinated oils increased the contact angle (118 °) and reduced the contact angle hysteresis (8.2 °) to achieve icephobic surfaces. The icephobicity of the prepared SLIPS was evaluated using a home-built mechanical test for icephobicity by applying normal stresses to detach the ice from the surface. Measuring the ice adhesion strength in a normal mode, using the home-built mechanical apparatus, uncovered the detachment behavior of the ice from the surface by its own weight [42]. Our study showed that assembling SLIPS on the surface of glass reduced the ice adhesion strength to 100 times lower (4.9 kPa) than untreated glass, aluminum, and stainless steel by -10 °C. Long term testing of the samples revealed that the thin film could reduce the strength of ice adhesion by 65% after 100 days.

2-3 Experimental section

Materials

Tetraethyl orthosilicate (TEOS), Ammonia solution 25%, 2-propanol 99.5% (IPA), poly(sodium 4-styrene sulfonate), average Mw ~70,000 (SPS), poly(allylamine hydrochloride), average Mw 50,000 (PAH), 1H,1H,2H,2H-Perfluorodecyltriethoxysilane 97% (PFDTS) were purchased from Sigma Aldrich. Fomblin® Y LVAC 25/6, average molecular weight 3.300 (PFPE), was purchased from Solvay. Deionized water (resistance 18.2 MΩ cm) was obtained using Milli-Q.

Preparation of silica nanoparticles (NPs)

Monodispersed Silica NPs were synthesized by a sol-gel reaction, as described elsewhere [43], and the size and zeta potential of the particles were determined using Dynamic Light Scattering (DLS) Malvern Zetasizer Nano ZS.

Preparation of thin films using the Layer by Layer (LbL) method

A pre-cleaning step for glass substrates was applied before the thin film coating procedure. Briefly, substrates were sonicated in a glass cleaning solution for 15 minutes and rinsed in distilled water for another 15 minutes, rinsing step repeated three times. For depositing the tetralayer structure of the thin film, the substrate was submerged in positive (poly(allylamine hydrochloride))(pH:7.50) and negative (poly(sodium 4-styrene sulfonate)(pH:4.00) or silica nanoparticles(pH:7.50)) solution for 10 minutes and then rinsed for two/one/one minutes in distilled water at room temperature. The concentration of the polyelectrolyte solutions was adjusted to 10mM, and the concentration of silica nanoparticles was 0.03 g/L. Multiple layers of polyelectrolytes and nanoparticles were attracted and deposited on the surface through the electrostatic interaction of oppositely charged molecules, and created a rough surface as a tetralayer thin film on the substrate, as illustrated in Figure 2-1 and Figure 2-2.

The fluorinated silane PFDTS was applied on the LbL-assembled thin films by vapor phase deposition in a reduced pressure chamber at 75 torrs and room temperature for 12 hours afterwards.

The samples were spin-coated with a sufficient amount of Fomblin® YL VAC 25/6 oil with an average molecular weight of 3300 amu for 60 seconds and 1500 RPM to achieve a thin, uniform layer of the lubricating oil. The weight of the infused lubricant was measured using a four decimal place analytical balance.

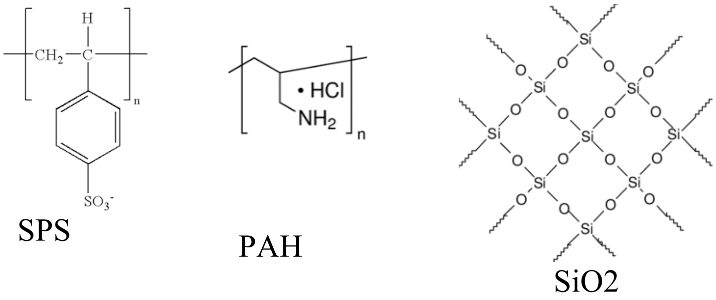

Figure 2-1 Chemical structure of SPS, PAH and SiO_2

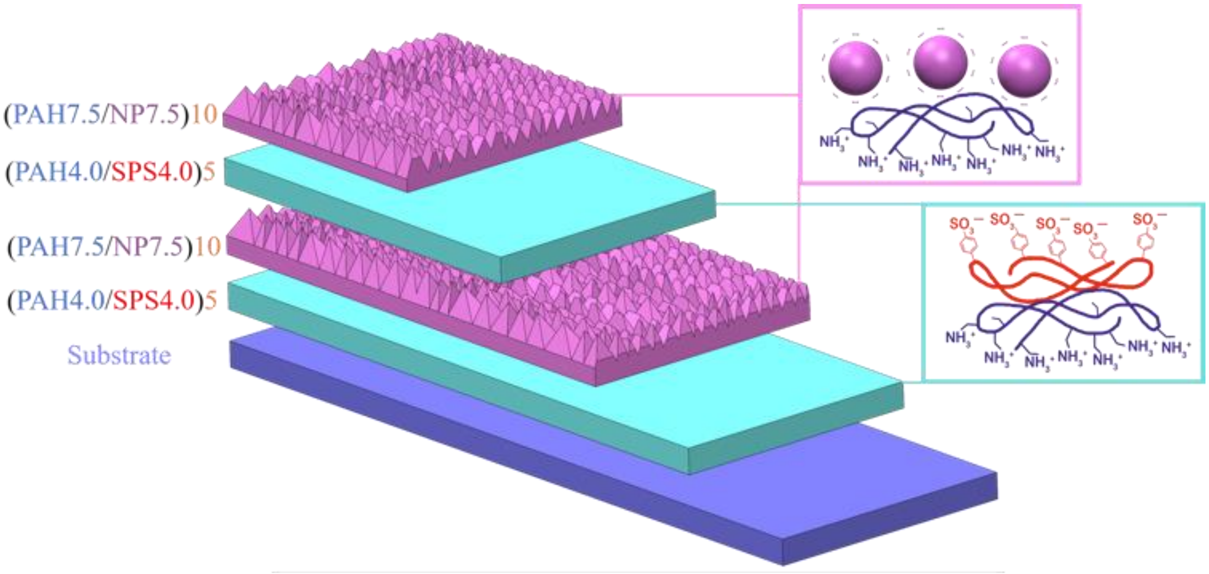

Figure 2-2 Schematic representation of LbL deposition of different polyelectrolytes and nanoparticles on the surface for creating a rough tetralayer thin film structure.

Characterizations

A KLA-TENCOR P6 Surface Profiler was used to determine the thickness of the thin films. They were scratched in a Z-shaped pattern without affecting the substrate. The depth of the nine different locations of the scratched pattern was measured by applying a 2 mN force. The thickness, reflectance, refractive index, and porosity of the thin films was measured and modelled using J.A.

Woollam Co. M2000 ellipsometry. The measurements were conducted in the wavelength range of 380 to 780 nm (~1.6–3.3 eV).

The transmittance of the thin films and SLIPS was measured using UV-Visible-NIR (Shimadzu UV 3150) in the visible light spectrum ranging from 380 to 780 nm wavelength.

Contact angle and contact angle hysteresis (CAH) were measured using Attension Theta Lite. 5µL of distilled water (18.2 MΩ·cm) was accumulated on the tip of the needle and then released on the surface by moving the syringe down to enable the droplet to touch the surface. By increasing and decreasing the volume of the water on the surface and measuring the maximum and minimum contact angles, the contact angle hysteresis was calculated. The reported values are the average of three measurements for each sample.

The nanomechanical properties of the thin films and surface topography were assessed by a Bruker MultiMode 8 Atomic Force Microscope (AFM). The height images were captured using NanoAndMore tips with a bending spring constant of 40 N/m, the resonance frequency of 50-200 kHz, and the tip radius of 10-20 nm and the mechanical properties were assessed by tips with a bending spring constant of 200 N/m, the resonance frequency of 500-600 kHz, and tip radius of 25-35 nm. The minimum deformation of the surface according to the nanomechanical properties evaluation was set as 2-5 nm, and the scan rate was 0.5-1 Hz. All images were processed using procedures for plane-fit and flattening. The surface morphology of the samples was analyzed by Field Emission Scanning Electron Microscopy (FESEM, LEO Supra VP-55).

A home-built mechanical test setup was prepared to evaluate the icephobicity of the surfaces. A cylindrical polypropylene ice mold with a diameter of 5.5mm was filled with water and sealed from the other end to prevent water leakage by taking advantage of capillary force. The ice mold was placed on the sample, which was fixed horizontally in the holder (Figure 2-3) for 3 hours at -10˚C. The temperatures values inside the chamber and the ice mold were measured to ensure the formation of ice and temperature changes during the ice-detaching test. Tensile strength tests with a rate of 5mm/min were carried out at least ten times for each sample to measure the maximum normal stress applied to detach the ice from the surface of substrates.

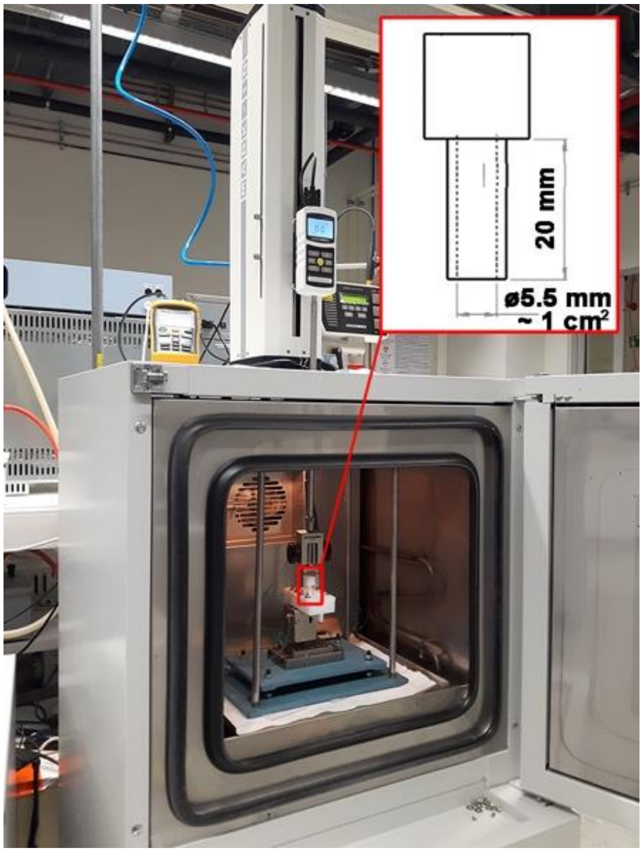

Figure 2-3 Ice mold, substrate and ice holder of the home-built icephobicity test setup

2-4 Results and discussion

Covering surfaces with different sizes of nanoparticles can customize the roughness of specimens at the nano- and micro-scale levels. The roughness of the surface provides holes and cracks for the infusion and trapping of the lubricant in harsh environments [13, 44]. In this study, silica nanoparticles were synthesized by a sol-gel method, and the size of the nanoparticles was adjusted by modifying the ratio of the [TEOS]/[NH3]$_{aq}$, as reported in Table 2-1 and Figure 2-4 for customizing the surface roughness with nanoparticles. Both the DLS and SEM particle size measurements clearly demonstrate the effect of reducing the ratio of [TEOS]/[NH3]$_{aq}$. Increasing the concentration of [NH3] in the solution supplies a higher amount of water, which in turn increases the efficiency of the hydrolysis reaction of TEOS and therefore the abundantly available silanols for condensation extend the size of the silica nanoparticles [45, 46].

Table 2-1. Measured silica nanoparticle sizes by DLS and SEM when [TEOS]/[NH3]aq ratio was varied during nanoparticle synthesis

Sample	DLS size (nm)	Zeta potential (mV)	SEM Particle size (nm)	STD	[TEOS]/ [NH3]aq
N1	36.8	-24.9	38.6	8.05	6.5
N2	63.2	-42.4	67.9	7.16	4.5
N3	83.2	-37.6	83.7	10.5	3.5
N1, N3	68.1	-35.0	-		-

The average number distribution of particle size is increased more than twofold when the ratio of [TEOS]/[NH3] is reduced to 3.5 and achieved 83.2 nm in DLS measurements and 83.7 nm in the SEM analysis, which indicates good correlation. A mixture of 36.8 nm and 83.2 nm (1:1) NPs was prepared to assemble two different sizes of nanoparticles on the surface and create a varied roughness scale. The reported average size of the DLS measurement of these samples is almost the average of the N1 and N2 samples, which demonstrates the homogeneous mixing of nanoparticles. These results evidence good consistency with the SEM images.

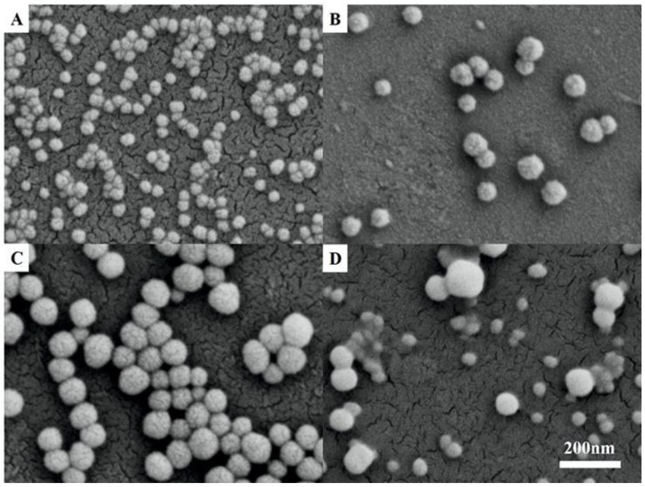

Figure 2-4 SEM image of silica NPs A-N1 (38.6 nm), B-N2 (67.9 nm), C-N3 (83.7 nm), D-N1&N3 (a mixture of 38.6 nm and 83.7 nm) silica nanoparticles. All scale bars are 200 nm.

The schematic representation of the architecture of the films is illustrated in the experimental section. On the glass slides which are used as the substrate, silica nanoparticles attain a negative charge in contact with aqueous solutions, due to the dissociation of the silanol groups [47]. The negatively charged surface of the glass adsorbs PAH chains; however, some of the positive charges of PAH remain exposed to the interfaces, which reverse the charge of the surface. In the next step, depending on the hierarchy, a negatively charged SPS polymer chain or silica NP deposits on the surface and reverses the surface charge again [48]. The mechanism of the LbL deposition makes the process independent of the shape and size of the substrate, with precise control at nanoscale. Hydroxyl groups of silica NPs in the final layer of the structure ensure that the thin film has hydrophilic characteristics. On the other hand, the high level of surface roughness reduces the chance of penetration of water into the surface, which results in hydrophobicity. In this study, thin films were prepared in two different architectures by LbL and water contact angle measurements for advancing the water contact angle (AWCA) and the water contact angle hysteresis (CAH) of the glass; the performance of the thin films are tabulated in Table 2-2. The specimens are numbered from S1 to S5 depending on their targeted architectural design of thin films. An example of such film, S5, indicates the number of layers (5 for PAH/SPS &10 for PAH/NP), tetralayers (2), and diameters of the NPs as 38.6 and 83.2 nm. The reference sample of untreated glass showed that the water contact angle was 15.66°, increasing when coated with polyelectrolytes and silica NPs, in S5, to 33.35° where the film thickness was measured as 190.2 nm. The results confirmed that surface roughness plays a determining role, compared with that of hydroxyl groups, in surface hydrophobicity.

Table 2-2. Structure and nanoparticle size of thin films

#	**Architecture**	**NP Size (nm)**	**AWCA[*] Hysteresis[**]**	**Thickness (nm)**
G	Bare glass	-	15.7	-
S1	(PAH‖SPS)5‖(PAH‖NP)10	38.6	26.6	87.81
S2	(PAH‖SPS)5‖(PAH‖NP)10	83.7	24.3	120.2
S3	((PAH‖SPS)5‖(PAH‖NP)10)2	38.6	28.5	142.3
S4	((PAH‖SPS)5‖(PAH‖NP)10)2	83.7	25.4	202
S5	((PAH‖SPS)5‖(PAH‖NP)10)2	38.6:83.7 (1:1)	33.4	190.2

* Advancing water contact angle,

** Receding water contact angle values for all samples were below five degrees.

SEM and AFM observations confirm that the deposition of the different architectures on the substrate can modify the roughness and the exposed surface of the samples dramatically. The S1 and S2 samples have a relatively lower thickness, and the collapsed, or uncovered, parts of the thin film in the S2 piece admit an insufficient number of bilayers (Figure 2-5).

Table 2-3. AFM surface topography at the nano- and microscale

	Glass		S1		S2		S3		S4		S5	
Scan size(μm)	10	1	10	1	10	1	10	1	10	1	10	1
Z range (nm)[1]	97.9	13.2	193	70.7	205	48.1	259	64.2	298	86.3	241	97.4
Surface %[2]	0.207	0.423	7.69	6.20	5.40	3.93	6.36	12.4	9.13	8.03	16.3	12.8
Rq (nm)[3]	3.90	0.583	22.3	9.27	26	6.85	32.9	7.49	35.4	11.0	30.3	15.3
Ra (nm)[4]	1.33	0.427	17.4	7.33	20.6	5.45	26.3	6.02	28.1	8.56	24.2	12.2

[1] The height difference between maximum and minimum

[2] Surface area difference between the actual and projected surface.

[3] Root mean square roughness of the surface.

[4] The arithmetic average of the absolute values of the roughness

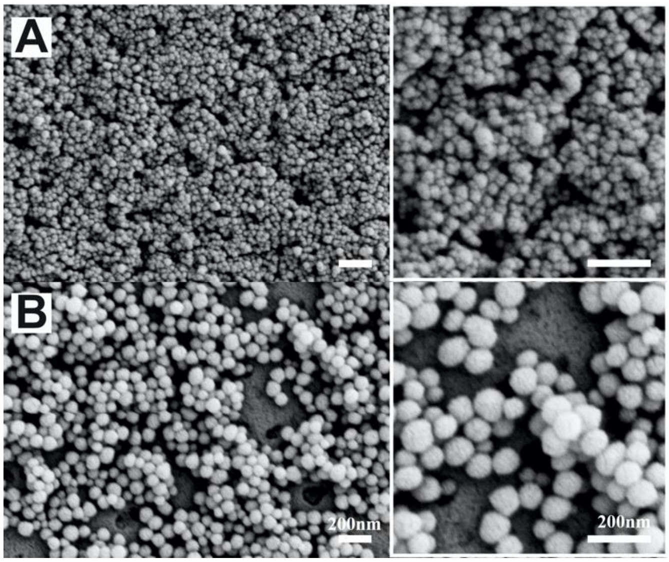

Figure 2-5 SEM images of A-(PAH||SPS)5||(PAH||NP)10 architecture using 38.6 nm silica nanoparticles B-(PAH||SPS)5||(PAH||NP)10 architecture using 83.7 nm silica nanoparticles: all scale bars are 200 nm

Additional layers of the thin film in the S3 and S4 samples not only cover the surface efficiently but also increase the surface roughness because of the superimposition of the different layers of the NPs, as shown in Table 2-3 represents the AFM results with two different scan sizes of 1 and 10 micrometers. The root mean square (RMS) of the roughness of the surface of the untreated glass was calculated as 3.9 nm and 0.6 nm in 10- and 1-micrometre scan sizes respectively, which confirms a relatively smooth surface compared with the coated samples. These results correlate well with the literature [49].

The sharp and nanometric changes in the height of the untreated glass in Figure 2-7 might be related to dust or some form of contamination from the test environment. Covering the glass substrate with NPs increases the roughness and the projected surface area of the thin films up to 35.4 nm RMS in sample S4 and 15.3 nm RMS in sample S5 at 10 and 1 μm scan size respectively.

Table 2-3 shows the changes in the projected surface area at 1- and 10-micrometre scan sizes. The S1 and S3 samples are assembled using smaller NPs: and thus, have a relatively higher difference in the projected area than other samples with larger NPs (S2, S4), as expected. However, the S4 sample, which has a sufficient number of layers to cover the surface and a continuous film on the substrate, has greater roughness.

This suggests that the samples with larger NPs build surfaces at a micro scale, and the samples with smaller NPs create roughness at the nano scale. These results and interpretations lead to a strong likelihood that mixing different sizes of NPs and depositing them with a sufficient number of layers can help to design a customizable rough surface. As reported in Table 2-3 and shown in Figure 2-6, the 16.8% and 12.8% the surface area difference for S5 at micro and nanoscale respectively can provide the necessary roughness to infuse the fluorinated lubricant on the thin film.

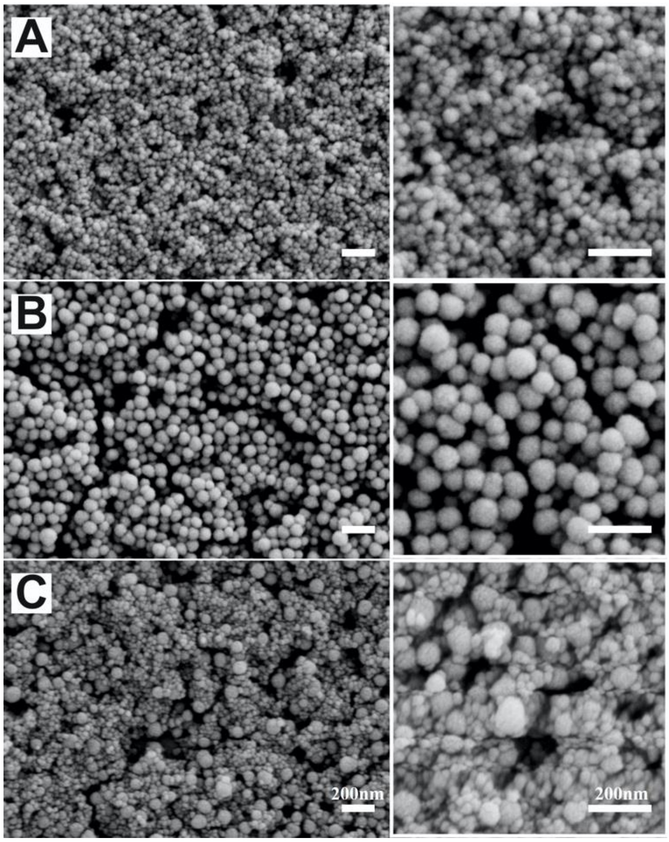

Figure 2-6 SEM images of A- ((PAH||SPS)5||(PAH||NP)10)2 architecture using 38.6 nm silica nanoparticles, B-((PAH||SPS)5||(PAH||NP)10)2 architecture using 83.7 nm silica nanoparticles 4, C-((PAH||SPS)5||(PAH||NP)10)2 architecture using (1:1) mixture of 38.6 nm and 83.7 nm silica nanoparticles. All scale bars are 200 nm.

Although, the observed rough morphology from SEM images and surface roughness from the AFM images prove that the created porous and rough surfaces in the thin films the existence of necessary voids and sites on the film to trap the lubricants. The Bruggeman effective medium approximation (EMA) has been used to model the optical properties of porous surfaces to estimate the fraction of the voids within the film [50]. The assembled S4 thin film with a thickness to be 216 nm exhibits a porosity of 25.3% by the ellipsometry measurements, as shown in Table 2-4. The deterioration of mechanical properties on the film in comparison with S5 samples makes S5 preferable to S4. The low mean square error of the fitted models and the consistency of the thickness measured by the profilometry results confirms the reliability of the void fraction values of thin films. Table 2-4 shows that silica nanoparticles may create the porosity inside the films: the larger the particle size, the higher the void fraction.

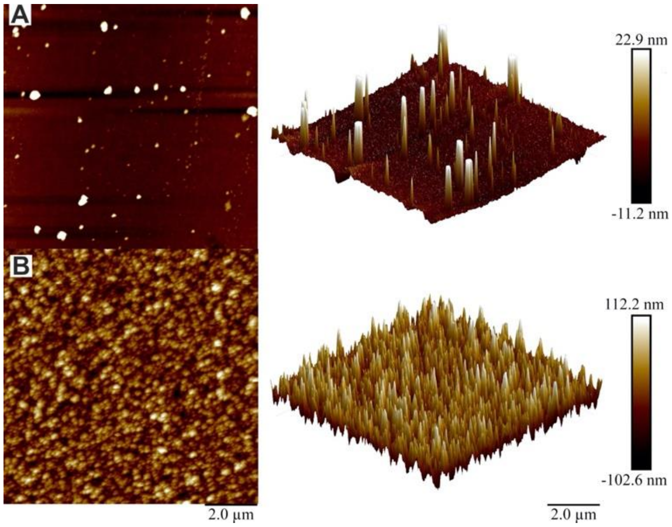

Figure 2-7 AFM images of A-Glass, B-((PAH||SPS)5||(PAH||NP)10)2 architecture using (1:1) mixture of 38.6 nm and 83.7 nm silica nanoparticles

Table 2-4. The thickness and void fraction of thin films measured using ellipsometry

Sample	**Thickness (nm)**	**EMA %**	**Thickness MSE (nm)**
(PAH||SPS)20	10	0	3.84
S3	114	2.8	7.29
S4	216	25.3	32.24
S5	170	16.2	6.9

The S3 sample has the smallest nanoparticle size of all the samples. Small particles can penetrate narrower porosities and holes on the surface. Therefore, they can mechanically support each other more effectively. The ratio of surface to volume in smaller particles is higher than in bigger ones. This ratio indicates that they can be firmly bonded to the substrate and other particles. The combination of different nanoparticle sizes in the S5 samples enhances the mechanical properties of the thin film and increases the durability of the surface roughness in harsh conditions.

The elastic modulus of the samples was extracted using retract curves and fitted according to the Derjaguin–Muller–Toporov (DMT) model [51]:

$$F - F_{adh} = \frac{4}{3} E^{*} \sqrt{R(d - d_0)^3)} \qquad (2\text{-}1)$$

where R is the radius of the tip, d-d_0 is the sample's deformation, F-F_{adh} is the measured force by cantilever relative to adhesion force and E^* is the reduced modulus. By considering the Poisson ratio (v_s), known as 0.5, and assuming infinite modulus for the tip (E_{tip}), the Young modulus of the thin film based on AFM measurements can be calculated using the following equation:

$$E^{*} = \left[\frac{1 - v_s^2}{E_s} + \frac{1 - v_{tip}^2}{E_{tip}} \right]^{-1} \qquad (2\text{-}2)$$

The nanomechanical properties of thin films, which have been assessed using AFMs, demonstrate that coating the surface with polymers and silica NPs reduces the Young modulus of the surface. The average reduced modulus of 500 points on each sample has been reported in Table 2-5.

Table 2-5 Nanomechanical properties of thin films

Sample	**E (GPa)**	**E* (GPa)**	**STD (GPa)**
G	20.1	22.1	1.28
S3	4.4	4.9	0.56
S4	3.5	3.9	0.35
S5	5.3	5.8	0.64

The stress-displacement curves of the ice detachment of different samples of ice on the thin film and substrates show that the failure of the material obeys the brittle model in which a very high standard deviation can be observed. The Weibull distribution model was applied to evaluate the ice adhesion force and compare the effect of the thin films and SLIPS on the substrate using the following equation [52]:

$$P(V) = \exp\left[- \left(\frac{\sigma}{\sigma_0} \right)^m \right] \qquad (2\text{-}3)$$

where P(V) is the survival probability, and *m* is the Weibull modulus, which is obtained experimentally. The lower the *m*, the wider the distribution. σo is the centrality and highlights the probability of failure for any stresses lower than or equal to the σo which is 63%, and is the fracture strength. In our investigation to apply this model, we conducted a mechanical test with at least nine different specimens in separate runs for each sample.

Figure 2-8 illustrates the average of three measurements of temperature change in the interface of the ice/surface of different samples over time. The creation of ice on aluminum substrate started 15 minutes after putting the sample in the environmental chamber; however, on the glass substrate it took longer to create the ice, and this affected the strength of the ice. Ice creation started in 22 mins on an icephobic surface. This means that the thin film not only reduces the ice adhesion strength to the surface but also manipulates the nucleation and growth mechanism of ice by providing nucleation sites and reducing the surface energy. Thus, the mechanical properties of the ice column diminish, and its durability weakens. As reported in Table 2-6 and Figure 2-9, stainless steel 304 has a wide ice adhesion strength distribution and aluminum a relatively narrow one. The of glass, stainless steel 304 and aluminum samples were measured as 538, 340 and 243 kPa, which is relatively close to 465, 340 and 242 kPa, the average value of the fracture stress, respectively. Although it seems that glass has the highest adhesion strength, analyzing the fracture cross-sections revealed that in most cases in the stainless steel 304 and aluminum samples, the ice column failed before detaching from the surface. This behavior might be related to the ice nucleation and growth mechanism and the effect of the cooling rate on the structure and strength of the ice[53].

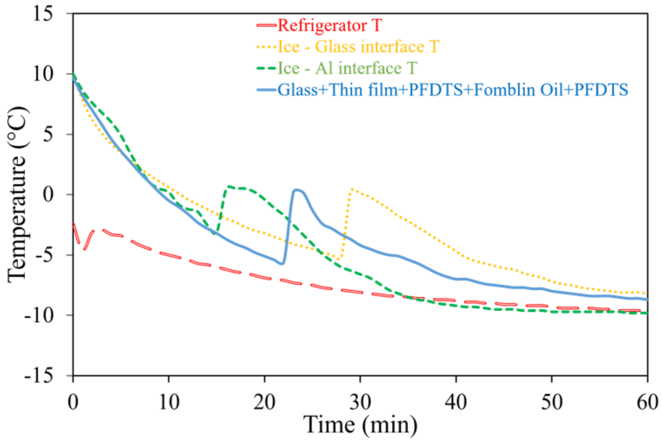

Figure 2-8 Temperature changes of the refrigerator and different surfaces by time

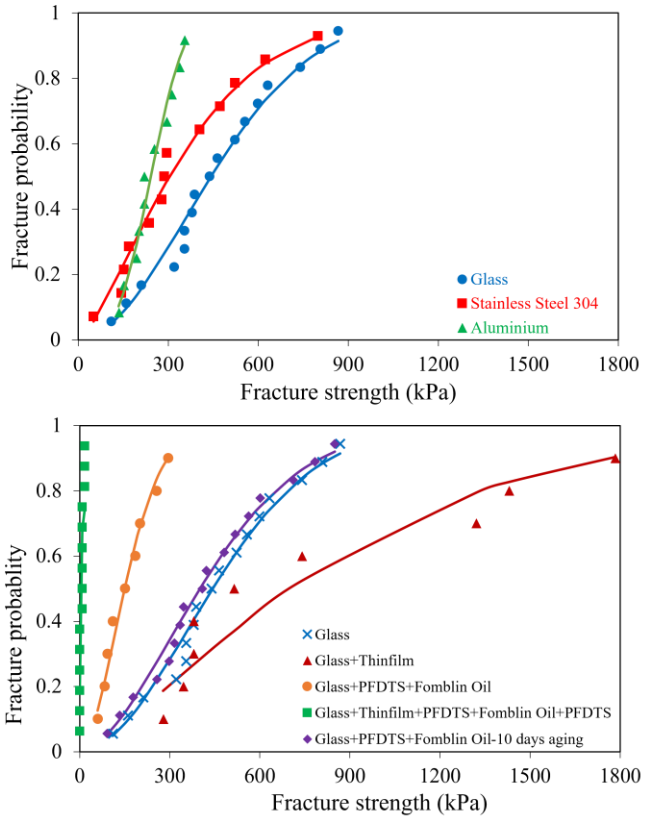

Figure 2-9 Weibull distribution of the ice adhesion strength of substrates and modified surfaces.

Table 2-6. Weibull parameters of thin films

Substrate / Thin Film (TF) Structure	**m**	**σ_o (kPa)**	**σ_{avg} (kPa)**	**STD[*] (kPa)**
Stainless steel 304	1.38	396.3	340.6	206.3
Aluminum	3.16	271.9	242.9	70
Glass	1.88	538	464.9	211
Glass+TF	1.30	929.1	796.91	533.3
Glass+PFDTS+Fomblin	1.79	184.4	158.9	76.5
Glass+TF+PFDTS+Fomblin+PFDTS	0.25	4.9	6.7	6.3
Glass+PFDTS+Fomblin-10 days aging	1.73	495.3	464.5	217

[*] Standard Deviation

The S5 sample, which possesses micro and nanoscale roughness and has more space on its surface to trap the lubricant, underwent mechanical ice detaching tests. Introducing the glass and thin-film sample to harsh conditions increased the ice adhesion strength to 796 kPa, with a standard deviation of 533 kPa. The porosity and roughness of the surface provide critical points for water to infuse into and stick to the surface more efficiently. Coating the glass with the lubricant alone can efficiently decrease the ice adhesion strength to about 160 kPa; however, the lubricant is not stable on the surface and can be removed easily, even by tilting. The vapor phase deposition of PFDTS on the surface increases the affinity between the substrate and lubricant, which guarantees the stability and penetration of the lubricant into the pores and cracks of the surface. This means that the leakage of the lubricant will be prevented and the porosities of the surface will create a reservoir to compensate for the loss of the lubricant due to the evaporation and drainage. Therefore, the environmental pollution of the lubricant will decrease. The roughness of the surface increases the density of the deposited PFDTS on the surface, which decreases the surface energy of the thin film [54, 55]. Although it has been reported in the literature that fluorinated silane groups may have low durability in contact with ice and water, covering the PFDTS layer with the lubricant may prevent the direct contact of this layer with water and ice and the durability of the layer will increase [56].

It should be noted that vapor phase deposition was applied under low vacuum conditions, and the amount of the deposited PFDTS on the surface was meager, which was barely detectable using a precise balance with the readability of up to 0.1mg (4 decimal places) on the 18.75 cm^2 glass slide. Therefore, the cost and complexity of the application process of PFDTS, and its environmental effect is negligible. On the other hand, infusing the fluorinated lubricant to the surface of the S5 sample ensures the stability of the lubricant, and, as is reported in Table 2-6, the ice adhesion strength approaches zero. The lubricant fills all the pores and blocks the water and moisture from penetrating the surface of the thin film. The S5 sample with fluorinated lubricant is thus indicated as an excellent candidate for supericephobicity, even in wet and moist conditions. The average weight change of the nine different samples due to lubrication was measured as $0.03g/18.75cm^2$, which ensures that the thickness of the oil layer is less than 8.5 μm (the density of the lubricant is 1.9g/ml). The vapor pressure of the Fomblin® Y LVAC 25/6 is about 610-8 torrs at room temperature, which demonstrates the low probability of the evaporation of the lubricant from the surface.

The AWCA and WCAH of the substrates and S5 samples with different preparatory steps are reported in Table 2-7. Applying S5 thin film to the substrate and filling its pores with lubricant increases the AWCA up to 120 degrees and decreases the WCAH to 8 degrees. It is shown that high AWCA and low CAH can be considered to be characteristic properties of icephobic surfaces, which correlates well with the literature [23, 25, 57].

The UV-Vis transmittance of the S5 sample coated with an infused lubricant, which is at least 85% transparent in the visible light range, is reported in Figure 2-10. Other samples have almost the same pattern, and they are transparent in the visible light spectrum. By using ellipsometry, the refractive index of the thin films and the reflectance of the lubricant-infused films are measured as 1.39 and less than 10% respectively. These results indicated that the assembled thin films could be categorized as anti-reflection thin films [58].

Table 2-7. AWCA and WCAH of substrates and thin films

Sample	**AWCA***	**WCAH****
Aluminum	95.3	86.5
Stainless Steel 304	93.9	80.4
Glass	15.7	15.7
Glass+PFDTS	72.5	48.0
Glass+PFDTS+Fomblin Oil	81.7	50.8
Glass+PFDTS+Fomblin Oil+PFDTS	97.7	52.2
Glass+TF (S5)	33.4	33.4
Glass+TF(S5)+PFDTS+Fomblin Oil+PFDTS	118	8.2

*Advancing Water Contact Angle

** Water Contact Angle Hysteresis

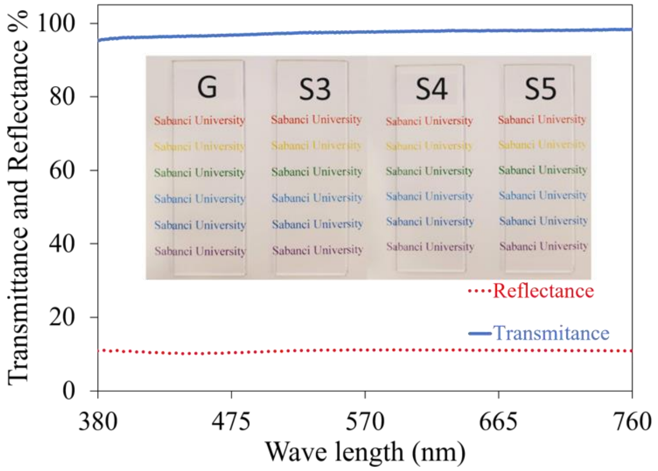

Figure 2-10 UV-Vis transmittance of Glass+S5+PFDTS+Fomblin Oil+PFDTS

The durability of the prepared samples was measured over for 100 days, as represented in Figure 2-11 and Table 2-8, to simulate the behavior of the thin films in winter. The samples were stored at room temperature in a vertical position for 5, 10, 20, 50 and 100 days and then an ice adhesion strength test was applied to at least nine samples for each aging time. The samples were stored in a vertical position, the maximum gravity forces have been applied to the lubricant, and the worst-case scenario has been simulated for draining the lubricant. In this case, the removal of the lubricant will be much faster than the samples that are stored in horizontal or acute angles.

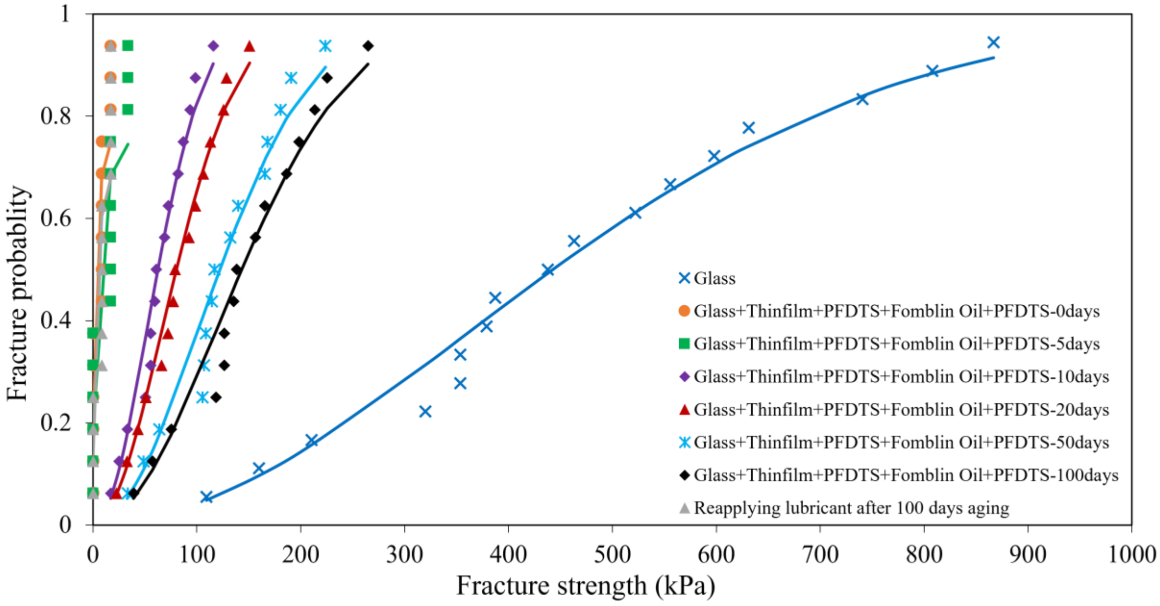

Figure 2-11 Weibull distribution of the ice adhesion strength of the aged samples for 5, 10, 20, 50 and 100 days.

Table 2-8 Weibull parameters of thin films for different aging periods

Substrate / Thin Film (TF) Structure	**m**	**σ_o (kPa)**	**σ_{avg} (kPa)**	**STD[*] (kPa)**
Glass+TF+PFDTS+Fomblin+PFDTS-5 days aging	0.25	9.8	13.5	12.6
Glass+TF+PFDTS+Fomblin+PFDTS-10 days aging	1.97	75.4	64.9	26.8
Glass+TF+PFDTS+Fomblin+PFDTS-20 days aging	1.93	97.1	83.8	36.2
Glass+TF+PFDTS+Fomblin+PFDTS-50 days aging	1.95	147.4	126.5	51.7
Glass+TF+PFDTS+Fomblin+PFDTS-100 days aging	1.97	172.7	148.5	61

[*] Standard Deviation

It was shown that the Weibull distribution of the ice adhesion strength of the icephobic samples shifted to the right. As the Weibull distribution shifts to the right, and closer to that of the untreated glass sample, the icephobicity of the sample decreases and the ice detachment gets harder. The comparison of σo of the aged samples in Figure 2-12 shows that although the ice adhesion strength increases over time, the rate of change decreases and reaches a threshold. The ice adhesion strength of the 100-day aged sample is 35% of that of untreated glass. During the winter season, which lasts 90 days in most regions on earth, these samples can reduce the ice adhesion strength by 65% without the need to renew the lubricant on the surface. Aging of the samples in the vertical position for 100 days drains the lubricant; however, the micro and nanostructure of the thin film is preserved during the aging. Reapplying the lubricant on the aged samples after 100 days, reload the pores of the surface with the lubricant and recovers the low ice adhesion strength of the surface as the fresh icephobic samples. Figure 2-9 and Table 2-6 shows that glass samples which are spin-coated by the lubricant without deposition of thin film, have very low durability for aging. These samples have lost their limited icephobic properties in about ten days and behave as non-treated samples.

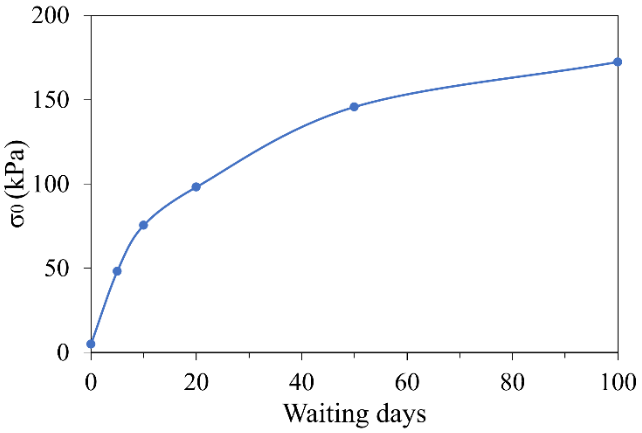

Figure 2-12 Change in ice adhesion strength of σ_o by ageing

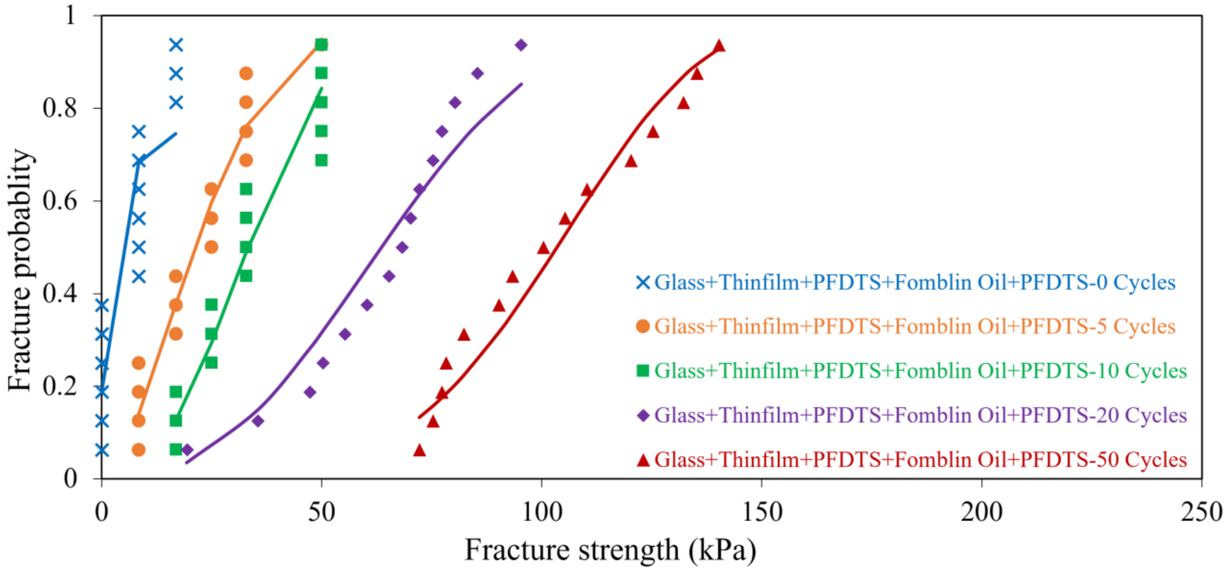

Figure 2-13 Weibull distribution of the ice adhesion strength of the cyclic iced/deiced samples for 5, 10, 20, 50 cycles.

Table 2-9 Weibull parameters of thin films for different iced/deiced cycles

Substrate / Thin Film (TF) Structure	**m**	σ_o **(kPa)**	σ_{avg} **(kPa)**	**STD*** **(kPa)**
Glass+TF+PFDTS+Fomblin+PFDTS-5 Cycles	1.66	26.5	22.8	11.8
Glass+TF+PFDTS+Fomblin+PFDTS-10 Cycles	2.44	38.7	33.8	12.7
Glass+TF+PFDTS+Fomblin+PFDTS-20 Cycles	2.50	73.6	63.9	19.1
Glass+TF+PFDTS+Fomblin+PFDTS-50 Cycles	4.39	112.5	102.6	22.8

*Standard Deviation

The durability of the icephobic thin films was evaluated for 5, 10, 20 and 50 icing/deicing cycles. The samples were placed in a vertical position inside the environmental chamber to simulate the worst possible condition, and the samples were submerged in water. In each cycle, the temperature of the chamber was reduced to -10°C from 25°C and then increased to 25°C with a rate of 0.3°C per minute. The Weibull distributions of the ice adhesion strength of the ice/deiced samples are reported in Figure 2-13 and Table 2-9. Even after 50 cycles of the icing/deicing, the samples preserved 80% of their icephobicity in comparison with non-treated glass. If we consider one icing/deicing cycle for each day during the winter season in real condition, it will take 50 days to reach 50 cycles. By comparing the results of the aging tests with cycling tests, it is observed that 20 days of aging or 50 cycles of ice/deicing has almost the same effect on the icephobicity of the samples; however, in 20 days only 20 cycles will be completed in real condition. Therefore, the durability of the samples is mostly are affected by the aging of the samples and draining of the lubricant and the icing/deicing cycles have a much lower influence on degrading of the icephobicity of the samples.

2-5 Conclusions

In summary, it can be observed that although hydrophobic surfaces have been investigated extensively in recent years, these still require further improvement in frigid and icy conditions. We have developed an icephobic SLIPS on a glass substrate using a simple layer-by-layer (LbL) self-assembly method, which is also scalable and low cost. The tetralayer thin film of PAH, SPS and silica NPs was deposited on the substrate, and a fluorinated lubricant was infused into these pores generated by bimodal distributed NPs on the surface to create SLIPS for tailoring the roughness of these films. The generated roughness in the form of holes and cracks is contributed to the infusion of more lubricant and helped to trap them inside longer even under challenging conditions. Besides, it provided to the deposition of denser PFDTS on the surface. The NPs size was varied by adjusting the ratio of the [TEOS]/[NH3]aq where the average NP sizes were measured to be within a range of 36.8 to 83.2 nm. The thickness of the thin films was about 200 nm, and AFM and SEM images confirmed that the surfaces of the thin films are rough at both micro and nanoscale (Rq: 30 and 15 nm respectively), enabling them to act as a reservoir for the lubricant. The Young module of the thin film was calculated through AFM measurements, and it was concluded that by customizing the surface roughness by intentionally creating bimodal NP sizes enhanced the mechanical properties of thin films and increased the modulus to 5.3 GPa. A home-built mechanical test setup was prepared in order to evaluate the icephobicity of the surfaces. The Weibull distribution model was applied to assess the ice adhesion force and compare the effect of the thin films and SLIPS, and the ice adhesion strengths were calculated. The results showed that the adhesion strength of the ice to SLIPS was almost zero. Also, this thin film not only reduces the ice adhesion strength to the surface but also manipulates the nucleation and growth mechanism of ice by providing nucleation sites and reducing the surface energy. Thus, the mechanical properties of the ice column diminish, and its durability weakens. Besides, these newly developed thin-films exhibit transparencies of up to 98% in the visible region due to porosities imparted through silica NPs, which is unlikely to have been the case in earlier reported results. The ageing of the thin film reveals that it can reduce the ice adhesion strength to 35% of the untreated surface, even after 100 days. Cyclic icing/deicing of the samples showed that the ice adhesion strength of the thin film after 50 cycles of icing/deicing is about five times lower than non-treated glass sample.

2-6 References

1. Andersson, A.K. and L. Chapman, *The impact of climate change on winter road maintenance and traffic accidents in West Midlands, UK.* Accident Analysis & Prevention, 2011. **43**(1): p. 284-289.
2. Tarquini, S., et al., *Investigation of ice shedding properties of superhydrophobic coatings on helicopter blades.* Cold Regions Science and Technology, 2014. **100**: p. 50-58.
3. Parent, O. and A. Ilinca, *Anti-icing and de-icing techniques for wind turbines: Critical review.* Cold Regions Science and Technology, 2011. **65**(1): p. 88-96.
4. Dalili, N., A. Edrisy, and R. Carriveau, *A review of surface engineering issues critical to wind turbine performance.* Renewable and Sustainable Energy Reviews, 2009. **13**(2): p. 428-438.
5. Meuler, A.J., G.H. McKinley, and R.E. Cohen, *Exploiting topographical texture to impart icephobicity.* ACS nano, 2010. **4**(12): p. 7048-7052.
6. Guo, P., et al., *Icephobic/anti-icing properties of micro/nanostructured surfaces.* Adv Mater, 2012. **24**(19): p. 2642-8.
7. Menini, R. and M. Farzaneh, *Advanced Icephobic Coatings.* Journal of Adhesion Science and Technology, 2012. **25**(9): p. 971-992.
8. Golovin, K., et al., *Designing durable icephobic surfaces.* Science Advances, 2016. **2**(3).
9. Chen, B., et al., *Numerical simulation and experimental validation of aircraft ground deicing model.* Advances in Mechanical Engineering, 2016. **8**(5): p. 1687814016646976.
10. Martin, C.A. and J.C. Putt, *Advanced pneumatic impulse ice protection system (PIIP) for aircraft.* Journal of Aircraft, 1992. **29**(4): p. 714-716.
11. Weisend, N.A., B.F. Trares, and K.L. Leffel, *Pneumatic deicer for shedding thin ice*. 1992, Google Patents.
12. Thomas, S.K., R.P. Cassoni, and C.D. MacArthur, *Aircraft anti-icing and de-icing techniques and modeling.* Journal of Aircraft, 1996. **33**(5): p. 841-854.

13. Wang, Y., et al., *The icephobicity comparison of polysiloxane modified hydrophobic and superhydrophobic surfaces under condensing environments.* Applied Surface Science, 2016. **385**: p. 472-480.
14. Schutzius, T.M., et al., *Physics of icing and rational design of surfaces with extraordinary icephobicity.* Langmuir, 2015. **31**(17): p. 4807-21.
15. Liu, Z., et al., *Frost formation on a super-hydrophobic surface under natural convection conditions.* International Journal of Heat and Mass Transfer, 2008. **51**(25): p. 5975-5982.
16. Meuler, A.J., et al., *Relationships between Water Wettability and Ice Adhesion.* ACS Applied Materials & Interfaces, 2010. **2**(11): p. 3100-3110.
17. Cao, L., et al., *Anti-icing superhydrophobic coatings.* Langmuir, 2009. **25**(21): p. 12444-8.
18. Cassie, A.B.D. and S. Baxter, *Wettability of porous surfaces.* Transactions of the Faraday Society, 1944. **40**(0): p. 546-551.
19. Zhai, L., et al., *Stable superhydrophobic coatings from polyelectrolyte multilayers.* Nano Letters, 2004. **4**(7): p. 1349-1353.
20. Cebeci, F.C., et al., *Nanoporosity-driven superhydrophilicity: A means to create multifunctional antifogging coatings.* Langmuir, 2006. **22**: p. 2856-2862.
21. Wenzel, R.N., *RESISTANCE OF SOLID SURFACES TO WETTING BY WATER.* Industrial & Engineering Chemistry, 1936. **28**(8): p. 988-994.
22. E, J., et al., *Wetting Models and Working Mechanisms of Typical Surfaces Existing in Nature and Their Application on Superhydrophobic Surfaces: A Review.* Advanced Materials Interfaces, 2018. **5**(1): p. 1701052.
23. Kim, P., et al., *Liquid-infused nanostructured surfaces with extreme anti-ice and anti-frost performance.* Acs Nano, 2012. **6**(8): p. 6569-6577.
24. Nosonovsky, M. and V. Hejazi, *Why superhydrophobic surfaces are not always icephobic.* ACS nano, 2012. **6**(10): p. 8488-8491.
25. He, Z., et al., *Room Temperature Characteristics of Polymer-Based Low Ice Adhesion Surfaces.* 2017. **7**: p. 42181.
26. Yokoi, N., et al., *Optically Transparent Superhydrophobic Surfaces with Enhanced Mechanical Abrasion Resistance Enabled by Mesh Structure.* ACS Applied Materials & Interfaces, 2015. **7**(8): p. 4809-4816.
27. Sunny, S., et al., *Lubricant-Infused Nanoparticulate Coatings Assembled by Layer-by-Layer Deposition.* Advanced Functional Materials, 2014. **24**(42): p. 6658-6667.
28. Liu, X., et al., *Slippery liquid-infused porous electric heating coating for anti-icing and de-icing applications.* Surface and Coatings Technology, 2019. **374**: p. 889-896.

29. Zhao, Z., et al., *Development of high-efficient synthetic electric heating coating for anti-icing/de-icing*. Surface and Coatings Technology, 2018. **349**: p. 340-346.
30. Decher, G., *Fuzzy Nanoassemblies: Toward Layered Polymeric Multicomposites.* Science, 1997. **277**(5330): p. 1232-1237.
31. Ozbay, S. and H.Y. Erbil, *Ice accretion by spraying supercooled droplets is not dependent on wettability and surface free energy of substrates.* Colloids and Surfaces A: Physicochemical and Engineering Aspects, 2016. **504**: p. 210-218.
32. Subramanyam, S.B., K. Rykaczewski, and K.K. Varanasi, *Ice Adhesion on Lubricant-Impregnated Textured Surfaces.* Langmuir, 2013. **29**(44): p. 13414-13418.
33. Janjua, Z.A., et al., *Performance and durability tests of smart icephobic coatings to reduce ice adhesion.* Applied Surface Science, 2017. **407**: p. 555-564.
34. Kulinich, S.A. and M. Farzaneh, *Ice adhesion on super-hydrophobic surfaces.* Applied Surface Science, 2009. **255**(18): p. 8153-8157.
35. Ruan, M., et al., *Preparation and anti-icing behavior of superhydrophobic surfaces on aluminum alloy substrates.* Langmuir, 2013. **29**(27): p. 8482-91.
36. Sarkar, D.K. and M. Farzaneh, *Superhydrophobic Coatings with Reduced Ice Adhesion.* Journal of Adhesion Science and Technology, 2009. **23**(9): p. 1215-1237.
37. Huang, X., et al., *A survey of icephobic coatings and their potential use in a hybrid coating/active ice protection system for aerospace applications.* Progress in Aerospace Sciences, 2019. **105**: p. 74-97.
38. Kulinich, S.A., et al., *Superhydrophobic Surfaces: Are They Really Ice-Repellent?* Langmuir, 2011. **27**(1): p. 25-29.
39. Aghdam, A.S., et al., *A New Method for Intense Cavitation Bubble Generation on Layer-by-Layer Assembled SLIPS.* Scientific Reports, 2019. **9**(1): p. 11600.
40. Ghorbani, M., et al., *Facile hydrodynamic cavitation ON CHIP via cellulose nanofibers stabilized perfluorodroplets inside layer-by-layer assembled SLIPS surfaces.* Chemical Engineering Journal, 2020. **382**: p. 122809.
41. Abbasiasl, T., et al., *Effect of intensified cavitation using poly(vinyl alcohol) microbubbles on spray atomization characteristics in microscale.* AIP Advances, 2020. **10**(2): p. 025318.
42. Wang, C., et al., *Laboratory test for ice adhesion strength using commercial instrumentation.* Langmuir, 2014. **30**(2): p. 540-547.

43. Malay, O., et al., *Polyurethaneurea–silica nanocomposites: Preparation and investigation of the structure–property behavior.* Polymer, 2013. **54**(20): p. 5310-5320.
44. Miwa, M., et al., *Effects of the Surface Roughness on Sliding Angles of Water Droplets on Superhydrophobic Surfaces.* Langmuir, 2000. **16**(13): p. 5754-5760.
45. Buckley, A. and M. Greenblatt, *The sol-gel preparation of silica gels.* J. Chem. Educ, 1994. **71**(7): p. 599.
46. Malay, O., I. Yilgor, and Y.Z. Menceloglu, *Effects of solvent on TEOS hydrolysis kinetics and silica particle size under basic conditions.* Journal of Sol-Gel Science and Technology, 2013. **67**(2): p. 351-361.
47. Behrens, S.H. and D.G. Grier, *The charge of glass and silica surfaces.* The Journal of Chemical Physics, 2001. **115**(14): p. 6716-6721.
48. Lvov, Y., G. Decher, and H. Moehwald, *Assembly, structural characterization, and thermal behavior of layer-by-layer deposited ultrathin films of poly (vinyl sulfate) and poly (allylamine).* Langmuir, 1993. **9**(2): p. 481-486.
49. Shah, H.C. and R.W. Davis Jr. *57.4: The Effect of the Roughness of the Glass Substrate on the Roughness of the Barrier Layer Used During Fabrication of Poly-Si TFTs*. in *SID Symposium Digest of Technical Papers*. 2003. Wiley Online Library.
50. Todorov, R., et al., *Microstructure and ellipsometric modelling of the optical properties of very thin silver films for application in plasmonics.* Thin Solid Films, 2017. **628**: p. 22-30.
51. Derjaguin, B.V., V.M. Muller, and Y.P. Toporov, *Effect of contact deformations on the adhesion of particles.* Journal of Colloid and Interface Science, 1975. **53**(2): p. 314-326.
52. Wachtman, J.B., W.R. Cannon, and M.J. Matthewson, *Mechanical properties of ceramics*. 2009: John Wiley & Sons.
53. Petrovic, J.J., *Review Mechanical properties of ice and snow.* Journal of Materials Science, 2003. **38**(1): p. 1-6.
54. Feng, B., et al., *Characterization of surface oxide films on titanium and adhesion of osteoblast.* Biomaterials, 2003. **24**(25): p. 4663-4670.
55. Bodner, T., et al., *Correlation of surface roughness and surface energy of silicon-based materials with their priming reactivity.* Monatshefte für Chemie - Chemical Monthly, 2012. **143**(5): p. 717-722.
56. Kulinich, S.A., et al., *The icephobic performance of alkyl-grafted aluminum surfaces.* Soft Matter, 2015. **11**(5): p. 856-861.

57. Eral, H.B., D.J.C.M. ’t Mannetje, and J.M. Oh, *Contact angle hysteresis: a review of fundamentals and applications*. Colloid and Polymer Science, 2013. **291**(2): p. 247-260.

Chapter Three

A New Method for Intense Cavitation Bubble Generation on Layer-By-Layer Assembled Slips

Published in Scientific Reports:

Aghdam, A. S., Ghorbani, M., Deprem, G., Cebeci, F. Ç., & Koşar, A. (2019). A new method for intense cavitation bubble generation on layer-by-layer assembled slips. Scientific Reports, 9(1), 1-13

doi.org/10.1038/s41598-019-48175-4 .

3-1 Abstract

The importance of surface topology for the generation of cavitation bubbles in micro scale has been emphasized during the last decade. In this regard, the utilization of surface roughness elements is not only beneficial in promoting mass transportation mechanisms, but also in improving the surface characteristics by offering new interacting surface areas. Therefore, it is possible to increase the performance of microfluidic systems involving multiphase flows via modifying the surface. In this study, we aim to enhance generation and intensification of cavitating flows inside microfluidic devices by developing artificial roughness elements and trapping hydrophobic fluorinated lubricants. For this, we employed different microfluidic devices with various hydraulic diameters, while roughness structures with different lengths were formed on the side walls of microchannel configurations. The surface roughness of these devices was developed by assembling various sizes of silica nanoparticles using the layer-by-layer technique (D2). In addition, to compare the cavitating flow intensity with regular devices having plain surfaces (D1), highly fluorinated oil was trapped within the pores of the existing thin films in the configuration D2 via providing the Slippery Liquid-Infused Porous Surface (D3). The microfluidic devices housing the short microchannel and the extended channel were exposed to upstream pressures varying from 1 to 7.23 MPa. Cavitation was incepted at much lower upstream pressures for the configurations of D2 and D3, while the survival of the generated bubbles was much longer for the configuration D3. Interestingly, hydraulic flip, which rarely appears in the conventional conical nozzles at high pressures, was observed at moderate upstream pressures for the configuration D2 proving the air passage existence along one side of the channel wall.

3-2 Introduction

The nature has inspired the humanity in the development of most of the cutting edge technologies to cope with different problems to improve the life quality. During recent years, lotus leaf and nepenthes pitcher-plant, which offer outstanding natural designs involving liquids and gases, have played a crucial role in inspiring the scientists to develop Slippery Liquid-Infused Porous Surfaces (SLIPS). These types of enhanced surfaces are able to control and improve different surface properties such as hydrophobicity and icephobicity for the use in separation, protection and transportation of underwater macro gas bubbles [1, 2].

Hydrodynamic cavitation in microscale as an emerging topic in the field of small bubble generation has attracted considerable attention in the engineering, energy and biomedical communities. This phenomenon can be manipulated by surface modifications in such a way that more intense cavity clouds could be generated. Recently, it was shown that surface roughness apart from the working fluid inside microfluidic devices has a significant effect on the generation of cavitation bubbles [3]. Therefore, it is of great importance to investigate the surface characteristics by focusing on substrate nanoengineering techniques to achieve intense bubble generation and earlier cavitation inception, which could be utilized in energy and biomedical applications.

SLIPS cover rough surfaces prepared on a substrate, which are formed using various techniques such as carving using chemical or physical reactions, attachment of nanoparticles (NPs), rods or wires using deposition, casting or assembly techniques. The resultant pores within the surface of the substrate are used as reservoirs to trap a slippery lubricant. Thus, changing the characteristics of rough surfaces can provide proper locations to trap different types of hydro or oleo phobic lubricants within pores and valleys of the surface. During the last decade, layer-by-layer (LbL) assembly as an emerging technique has attracted the interest of many scientists for achieving different substrates regarding the surface roughness [4-6]. This method has been introduced as a sub-nano scale approach in the assembly of any kind of electrostatically charged particles of electrolytes on oppositely charged substrates or sublayers [7]. The self-assembly of alternately charged polyelectrolytes as adhesion layer can provide a reliable and adhesive sublayer, which is sufficiently charged to embrace oppositely charged NPs and to attain a robust and mechanically strong and rough surface. As a result, the lubricant trapped within these porosities serves as stable and endurable SLIPS [8].

The studies related to the surface roughness effect on bubble dynamics mostly focused on bubble separation and mass transportation. In this regard, SLIPS, hydrophobic and superhydrophobic surfaces have been considered by scientists in trapping, separating and transporting air bubbles under water. There is a major difference in the behavior of these surfaces encountering bubbles. For hydrophobic and surperhydrophobic surfaces, the micro and nanoscale roughness on the substrate traps pockets of air within its pores and does not allow water to penetrate. On the other hand, SLIPS provide hydrophobicity and aerophilicity without trapping dry air pocket, where water droplet in air environment or air bubble under water becomes confined under a thin layer of the trapped lubricant and not only withstands the upward buoyancy force of the air bubble but also increases the life time and durability of air bubbles to pressure changes [2, 9]. Some researchers have taken the advantages of SLIPS to transport bubbles using the buoyancy force, to change the path of bubble and deviate their route, to absorb bubbles generated within a liquid and direct them along a trajectory[10-12]. The functionalities of SLIPS in protecting gas bubbles and increasing their life time under water have attracted the attention of related research communities dealing with macro bubbles. However, the behavior of these surfaces interacting with micro size bubbles clusters and clouds has not been sufficiently covered. Few attempts regarding hydrodynamic cavitation have been made to study cavitating flows in micro scale in the literature [13, 14], where advanced surface engineering techniques were not considered. It could be possible to reach fully developed supercavitation conditions inside microfluidic devices [15, 16] and to employ the energy released from the collapse of cavitation bubbles in different applications varying from thermoelectric energy generation [17] to sonoluminescence applications [18]. Therefore, in the light of the studies on cavitation in microscale, the recent investigations deal with the surface configurations such as roughness implementations and embedded pillars inside a microchannel [19] to generate intensified cavitating flows.

Motivated by the promising results of recent studies, SLIPS were formed on the microchannels in this study by assembling several layers of thin film using the LbL technique, and fluorinated oil was trapped within the pores of the film. The microfluidic devices were initially fabricated using a state-of-the-art process flow for formation of side wall roughened channels. Several layers of polyelectrolytes and NPs were assembled on the surface of microchannels by using the LbL technique and then by making the thin film surface favorable for the lubricant. The porosity of the thin film was filled by the oil, and the performances of the enhanced microchannels were evaluated. The surface enhanced devices with different hydraulic diameters were exposed to upstream pressures ranging from 1 to 7.23 MPa, while the downstream pressure was kept at the atmospheric pressure level. Accordingly, to generate intense cavitating flows and to lead to earlier cavitation inception, the surface modification effects were examined. This study reveals the potential of roughened surfaces and SLIPS in generating the bubble clouds (even at the center of the microchannel in some cases), which bolsters the idea of facile cavitating flow patterns in micro scale even at low pressure drops. The results of this study could be well exploited in energy harvesting applications in microscale as well as in biomedical applications.

3-3 Methods and Materials

3-3-1 Methods and materials for creating SLIPS

3-3-1-1 Materials

Tetraethyl orthosilicate (TEOS), ammonia solution 25%, 2-propanol 99.5% (IPA), poly(sodium 4-styrenesulfonate), average molecular weight of 70,000 (SPS), poly(allylamine hydrochloride), average molecular weight of 50,000 (PAH), 1H,1H,2H,2H-perfluorodecyltriethoxysilane 97% (PFDTS) were purchased from Sigma-Aldrich (St. Louis, USA). Fomblin Y LVAC 25/6, average molecular weight of 3,300 (PFPE) was purchased from Solvay (Brussels, Belgium). Deionized water (resistance 18.2 MΩ cm) was obtained using Milli-Q.

3-3-1-2 Assembly of thin film coatings for SLIPS

3-3-1-2-1 NPs

Monodispersed silica nanoparticles were synthesized in parallel lines with the literature [20] by tuning the ratio of [TEOS]/$[NH_3]_{aq}$ to control the size of the particles.

3-3-1-2-2 Preparing LbL solution

LbL assembly was performed in two different ways in order to assess the properties of thin films on silicon wafer and evaluate the generation of cavitating flows within the microfluidic devises. For applying the thin film both on bare silicon wafer and microfluidic devices, two solutions of positively charged PAH and a solution of negatively charged SPS with concentrations of 10 mM and pH of 4.00, 7.50 and 4.00, respectively, were prepared. Silica NPs dispersed in water were prepared as a mixture (1:1) of 40 and 80 nm number average size with concentration of 0.03g/L each. The pH of the negatively charged suspension was adjusted to 7.50.

3-3-1-2-3 LbL assembly of thin films on microfluidic devices and bare silicon wafer

The assembly of the thin film on bare silicon wafer was performed using the dip coating technique, and the substrates, which were sonicated in glass cleaning solution for 15 mins and rinsed in water for another 15 minutes, were submerged in the oppositely charged polyelectrolytes and NPs for 10 minutes and were rinsed for 2/1/1 minute in three separated distilled water tubes.

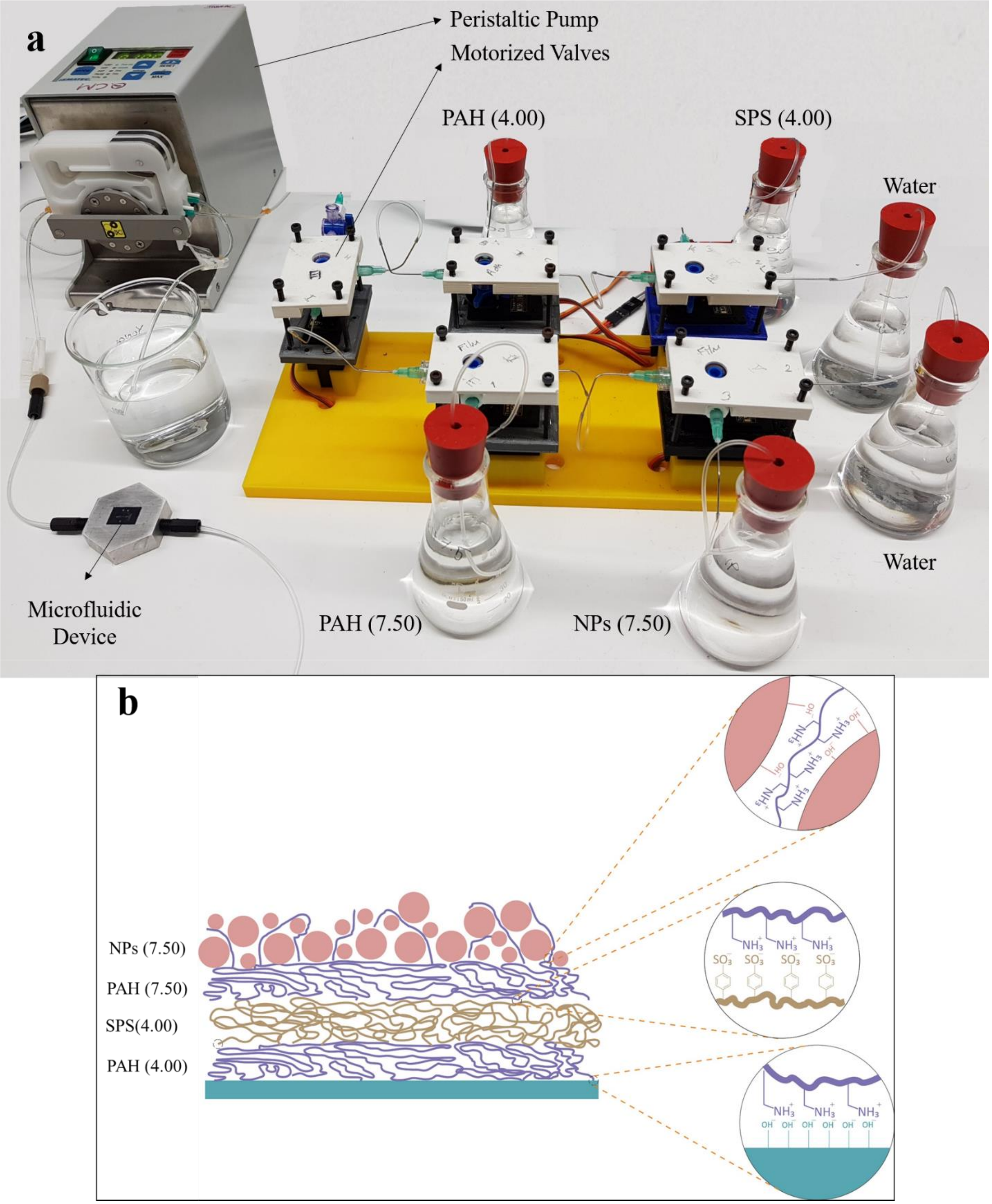

Figure 3-1 a-Peristatic pump and a home-made Polyelectrolyte Distributer System (PDS) b-schematic of Layer by Layer assembled polyelectrolytes and nanoparticles

Microfluidic devices have an inaccessible geometry due to their design and high pressures, which they should withstand during cavitation tests. As it was impossible to apply the SLIPS before the fabrication of microfluidic devices, the assembly of thin film on devices was executed using a peristatic pump and a home-made polyelectrolyte distributer system (PDS) to pass the various polyelectrolytes consecutively with a feeding rate of 0.2 mL/s through the devices and then to rinse it with a sufficiently large quantity of water to remove excessive and loosely bounded electrolytes or NPs (Figure 3-1a).

The final schematic of the thin film both on bare silicon wafers and microfluidic devices is as follows: (PAH(4.00)||SPS(4.00))5||(PAH(7.50)||NP(7.50))10 (Figure 3-1b)

3-3-1-2-4 Heat treatment and applying lubricant

The prepared thin films for both cases were dried in room temperature and under a vacuum chamber (75 torr) for at least 12 hours. A solution of PFDTS and ethanol 1%(V/V) was applied on the surface of the thin films followed by another 12 hour period of 75 torr vacuum exposure in room temperature to evaporate and clear away the excessive ethanol from the surface. The samples were undergone a 2 hour heat treatment of 100℃ to increase both the durability and stiffness of the thin film and creation of covalent bonds between fluorine compound and thin film. Eventually, a very thick layer of Fomblin YL VAC 25/6 lubricant with an average molecular weight of 3300 a.m.u was spread over the thin film on the silicon wafer and was spun for 60 seconds at 1500 RPM to remove excess oil. For microfluidic devices, the lubricant was injected to the channel.

3-3-2 Experimental Procedure and Configurations

All the microfluidic devices were fabricated out of double side polished silicon wafers with a thickness of 380 µm. All the steps of the fabrication of microfluidic devices were executed according to the techniques adopted from semiconductor based microfabrication techniques, which were explained in our previous study [3]. Seven microfluidic devices with different hydraulic diameters and side wall roughness length were employed in this study. The height of the side wall roughness elements was selected as $0.1D_h$. These elements were formed as a structural roughness according to the geometry design. The detailed properties of these devices were listed in Table 3-1. Meanwhile, the equivalent sand-grain roughness (k_s) was calculated as 5.863 µm using the algorithm presented by Adams et al. [21], which is suitable for low measured roughness values.

Table 3-1 The detailed properties of the microfluidic devices

Microfluidic device	**Microchannel hydraulic diameter, D_h [µm]**	**Side wall roughness Length**
CH1	200	0.5 L
CH2	200	L
CH3	133	0.33 L
CH4	133	0.5 L
CH5	100	0.33 L
CH6	100	0.5 L
CH7	240	0.33 L

The flow restrictive element in the experimental setup presented in our previous study [3] induces a sudden drop in pressure due to reduction in the cross-sectional area so that small bubbles from the flow restrictive element emerge due to hydrodynamic cavitation. It is predicted to obtain intense generation of cavitation bubbles with the surface modification. For all the microchannel configurations, the walls of microchannels are equipped with three pressure sensors to measure local pressures at the prescribed locations, namely before the entrance of the restrictive element, vena contracta ($1D_h$) and entrance of the extended channel ($5D_h$-$8D_h$) [22]. The same sensors were used to assess the pressure recovery inside the microchannel.

The glass wafer assists in visualizing fluid flows inside the channels. The experiments were conducted by applying different inlet pressures. The inlet pressure was varied from 1 to 7.23 MPa, while the outlet pressure at the microchannel was fixed to 0.1 MPa. The whole steps of the visualization experiments were comprehensively explained in our previews study [23]. The visualization was carried out in two main regions. The first region was the entrance of the microchannel with the length of 1.6 mm, where the pressure was expected to decrease to the vapor saturation pressure, and the second region was the extension region with the width of 900 µm and length of 1.6 mm, where the bubble generation was likely to appear in this area.

3-3-3 Characterization

3-3-3-1 DLS

The size and zeta potential of synthesized NPs were measured in a disposable capillary cell (DTS1070) using the Dynamic Light Scattering (DLS) technique via Malvern Zetasizer Nano ZS.

3-3-3-2 AFM and SEM

The surface topography was obtained using the Bruker Multimode 8 atomic force microscope (AFM). The height images were captured using NanoAndMore tips with a bending spring constant of 40 N m, resonance frequency of 50-200 kHz, and tip radius of 10-20 nm. All the images were processed (using procedures for plane-fit and flatten). The surface morphology of the samples was analyzed by field emission scanning electron microscopy (FESEM, LEO Supra VP-55).

3-3-3-3 CA

Contact angle (CA) and contact angle hysteresis (CAH) were measured using the equipment Attension Theta Lite. A 5 μL droplet of distilled water (18.2 MΩ·cm) was accumulated on the surface of the samples for measuring the CA, and by adding and removing the water from the stabilized droplet, the contact angle hysteresis was obtained. The reported values are the average of three subsequent measurements for each sample.

3-3-3-4 Ellipsometry

Thickness, reflectance, refractive index and porosity of thin films were measured and modeled using J.A. Woollam Co. M2000 ellipsometry. The measurements were conducted in the range of 380 to 780 nm (~1.6–3.3 eV) wavelengths.

3-4 Results and discussion

3-4-1 Surface properties

Figure 3-2 displays the SEM images of silica nanoparticles and the D2 thin film on silicon wafer. The SEM images of NPs are consistent with the DLS results. The sizes of the nanoparticles were measured as 40 and 80 nm (Table 3-2). The mesoporous surface of the bigger nanoparticles is shown in Figure 3-2b, which proves the nanoscale roughness and higher efficiency of the surface in making the infused lubricant become stable on the surface of samples. It is clear from Figure

3-2c that a uniform layer of the combination of the two different sizes of the nanoparticles is assembled on the surface of the silicon wafer and creates artificial roughness on the smooth surface of the wafer.

The Bruggeman effective medium approximation (EMA) was used for modelling ellipsometry results of porous surfaces to estimate the thickness and fraction of the voids within the film [24]. The thickness of the layer by layer assembled thin film was measured as 120 nm, and the 10 % EMA of the voids within the film can be considered as another evidence for the existence of the pores to save the lubricant and for the formation of the SLIPS.

Introducing PFDTS reduces the surface energy, which leads to hydrophilicity. The Fluorinated compound alters the affinity of the surface, and the surface roughness provided by the thin film makes the pores hold the lubricant on the surface under harsh conditions. Therefore, the lubricant withstands intensified cavitating flows even at very high velocities and turbulent flow conditions, and the flow patterns do not change during the multiple and prolonged experiments suggesting the repeatability of the results. The Root Mean Square (RMS) of the roughness of the surface is reported as 14.2 nm according to the AFM results. The projected surface of the thin film shows a 0.6% increase in the surface area, which ensures that the lubricant has some space within the pores of the surface to build a reservoir and be caught there during the fluid flow.

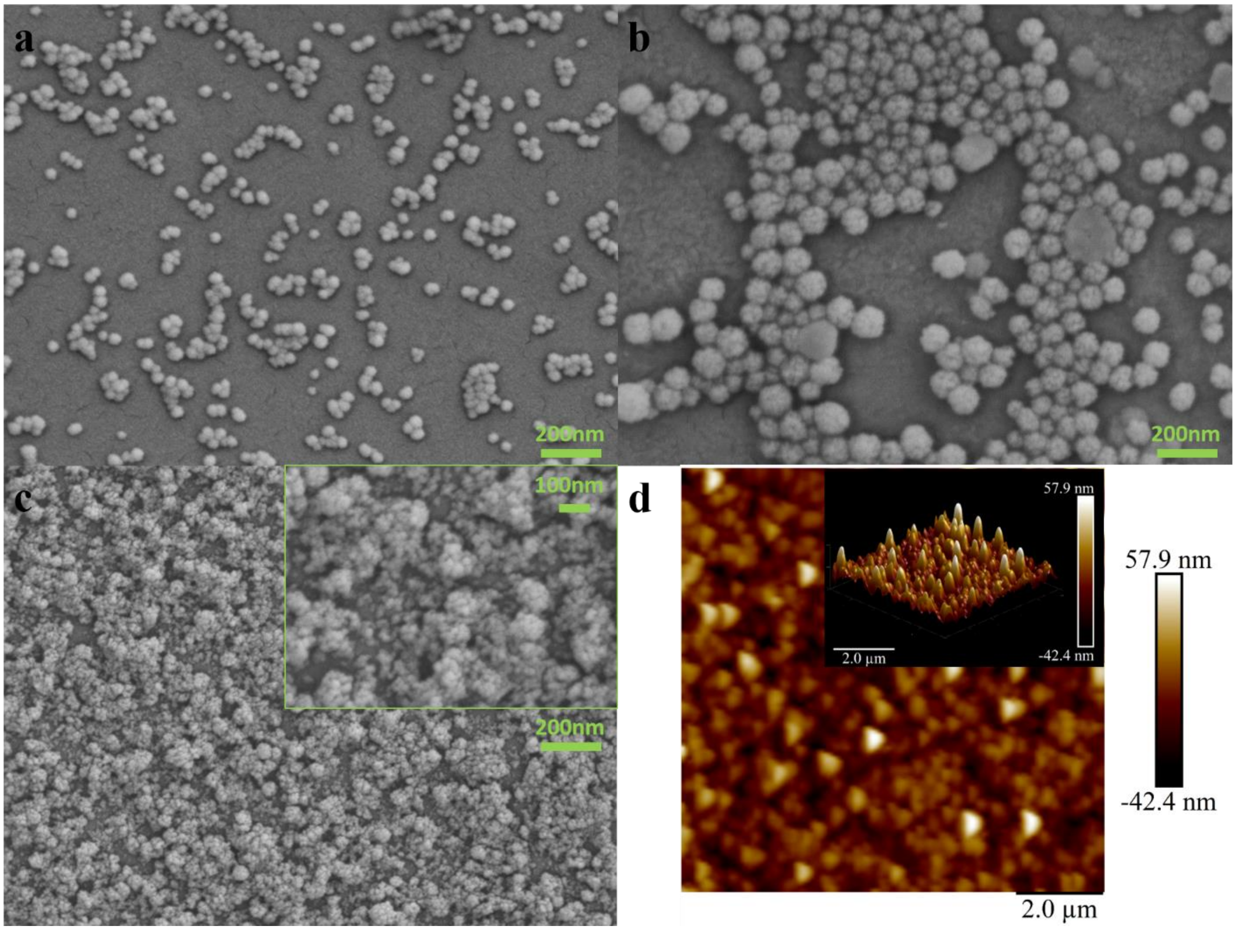

Figure 3-2 SEM and AFM images of synthesized silica nanoparticles and layer by layer assembled D2 channel a-40nm NPs b-80nm NPs c-layer by layer assembled D2 coating d- AFM height image of D2 coating

Table 3-2 DLS size and Zeta potential of synthesized and mixed silica nanoparticles

Sample number	DLS Size [nm]	Zeta potential [mV]	SEM Particle size [nm]	STD	[TEOS]/ [NH3]aq
N1	38.2	-22.6	33.4	7.55	6.5
N2	86.5	-38.5	81.4	8.25	3.5
N1, N2 (1:1)	68.1	-35.0	-		-

3-4-2 The effect of the SLIPS and LBL assembled silica nanoparticles on the inception of the cavitation phenomenon

Figure 3-3 displays a general overview of cavitation inception. Just beyond the vena contracta, the pressure suddenly decreases, and cavitation bubbles appear at each column. The inception of cavitating flows was investigated thoroughly inside the microfluidic devices using the fluorinated enhanced surface by LBL assembled silica nanoparticles and SLIPS, which were named in this study as D2 and D3, respectively. The inception was visualized in two regions, namely microchannel and the extended channel, which is the channel downstream of the microchannel. The results obtained from these devices were compared with the regular device with plain surface, which is called D1 in this study.

Figure 3-3 illustrates the effect of the SLIPS (D3) in the generation of cavitation bubbles at lower pressures. The results obtained from the devices with D3 coating are compared with the results of the devices having plain surfaces in this figure. The inception pressure is reduced more in the smaller channels (e.g. CH4), while there is still a considerable decrease in the inception pressure for the bigger channels (e.g. CH1) with intensified cavitating flows. Surface roughness is one of the major parameters influencing cavitating flows. It affects the boundary layer, which in turn affects the occurrence of cavitating flows. The surface roughness facilitates the cavitation inception and augments the nucleation of cavitation bubbles, since heterogeneous nucleation occurs in practical engineering situations rather than homogenous nucleation. Thus, crevices, roughness elements and porosity facilitate nucleation and facilitates cavitation inception. On the other hand, it can increase the flow instability, depending on the size and spatial distribution of the roughness elements [25].

. The overall trend in the cavitation inception in the regular side wall roughened channels is reflected as lower upstream pressure values for the bigger channels, which shows an earlier arrival of the vapor saturation pressure condition in these channels (e.g. CH1). Therefore, besides the new structural design, SLIPS is considered as an effective way to lead to an earlier generation of cavitation, which is essential to decrease the input energy and to increase the efficiency of microfluidic devices in providing cavitating flows.

Cavitation inception occurs with the formation of attached twin cavities inside the microchannel, which are limited to the inlet of the nozzle. The most important parameter in the formation of the flow regimes in micro scale is the surface tension. The surface tension of water is s = 0.0728 N/m at 293.15 K, and the previous results corresponding to water indicated that bubbly flow is a less dominant flow regime for micro scale cavitating flows[13]. Weak forces due to surface tension make the bubbles in liquids grow more, and the surface nuclei are the source for them. In addition, the surface tension mostly determines the bubble departure and prevents the detachment of the voids/non condensable gases from the surface. Since the diameter of the bubble is more comparable to the diameter of the channel in micro scale, this effect is more pronounced in the microfluidic devices facilitating the condition for the generation of cavitating flows. Therefore, cavitation phenomenon appears in bubbly flow pattern inside the microchannel within a small range of working conditions, and twin cavity clouds appear instead.

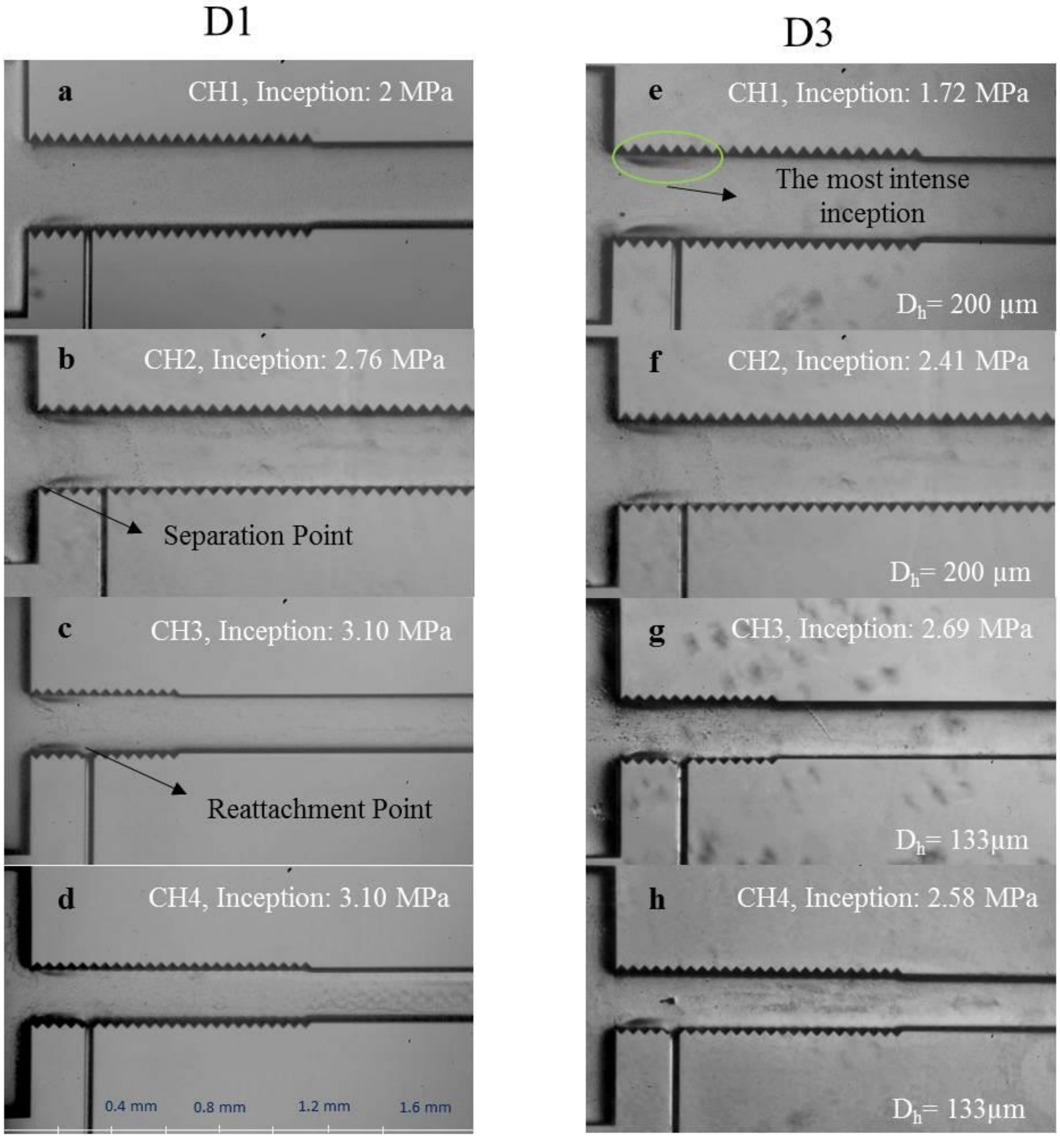

Figure 3-3 The qualitative comparison of the inception of cavitation phenomenon inside the regular microchannels with state-of-the–art design (D1) and SLIPS enhanced one (D3)

To reveal the effect of surface modification on twin cavity formations, more tests were done on the biggest available microchannel (CH7), where the side wall roughness elements cover one third of the microchannel. Figure 3-4 shows the inception in CH7 with the coatings of D2 and D3 and their comparison with the plain microchannel. As seen, the lubricant is deflected due to the high pressure fluid flow, and the roughness of the surface has a direct contact with the flow. As a result, the inception pressure decreases to 1.48 MPa for the coating D3 corresponding to the lowest value for inception pressure. For the D3 coating, after nucleation of cavitation bubbles, a very thin layer of lubricant covers the surface of the bubble and protects it from collapse[26]. However, D2 samples do not have any lubricant within its pores. Thus, it is shown that larger microchannels with shorter side wall roughness elements cause cavitation inception at much lower upstream pressure, which is a result of surface dominating and dictating cavitation events.

Contact angle measurements show that water has the highest contact angle in the case of D3 coating. The contact angle hysteresis of the D2 and D3 coatings are measured to be 100° and 5°, respectively, which means that the droplet on the lubricant of the D3 coating can easily slide. However, the droplet on the D2 coating is pinned on the surface [27]. On the other hand, the D1 surface is hydrophilic, and the water droplet is completely spread on the surface. It should be noted that the behavior of contact angle of air bubble in water medium can be predicted using the water droplet in air medium. They can be considered as supplementary angles as documented in the literature [11]. The curved shape of the intersection of the droplet and the lubricant for the D3 coating shows that a very thin layer of the lubricant covers the surface of the droplet, which can protect the bubble from collapse in water medium [9, 26].

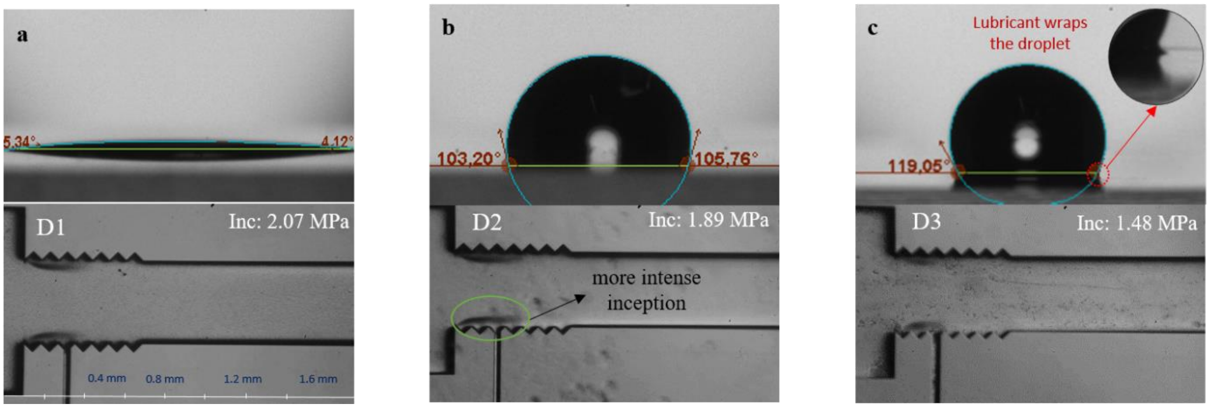

Figure 3-4 The inception inside CH7 and the enhancement demonstration with SLIPS and LBL silica nanoparticles and the water contact angle of the channel a- hydrophilic surface of D1 coating b- hydrophobic surface of D2 coating c- hydrophobic surface of the D3 coating and thin layer of lubricant covering the droplet

The reduction in the hydraulic diameter of the microchannel leads to an interesting behavior in the inception and flow patterns inside the microchannel and the extended channel. While weaker inception is observed inside the smaller microchannel (CH5 and 6), much more intense inception is captured in the extended channel. Interestingly, there are almost no twin cavity clouds in the extended channel for the bigger microchannels at corresponding inception pressures as shown in Figure 3-5.

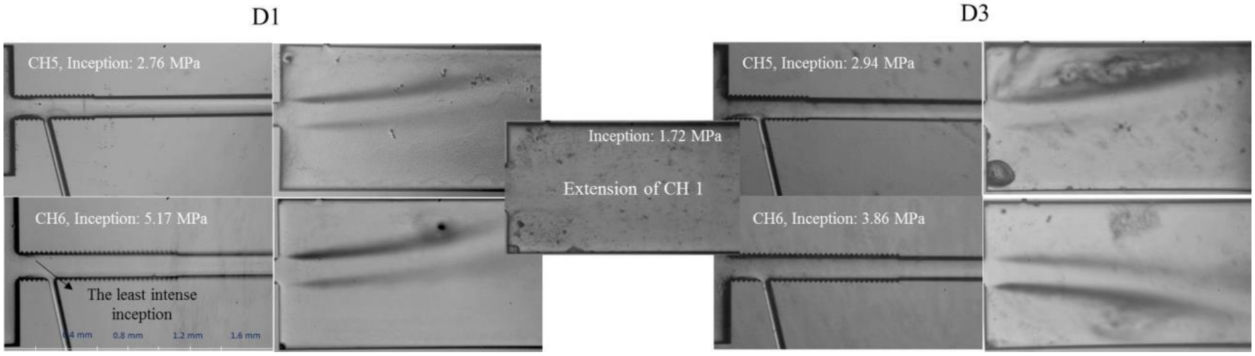

Figure 3-5 Cavitation inception in the extended channel for the smaller microchannels (CH5 and 6) enhanced by D3 and the comparison with the corresponding extended channel for the larger microchannel

Cavitation occurs due to rapid changes at pressure in the smaller microchannels, when flow is injected inside extended channel. This rapid change of channel size has a direct effect on both pressure and velocity, which causes cavitation, and bubbles are mostly visible in the area such as vena contracta. The high values of the pressure at the vena contracta location (P2) for smaller microchannels support the hypothesis of later occurrence of inception (Figure 3-6). In addition, the pressure in the extended channel exhibits a stable trend (P_{abs}=0), which is less compared to the larger microchannels. This proves that the design parameters are significant in achieving the desirable cavitation feature at different locations. Apart from the size variation effects, the surface enhancement with the coating D3 also exhibits its significant effect in the generation of more intense clouds in the extended channel. Large vortices and several separations are observed as shown in Figure 3-5 for the D3 coating, which presents larger pressure variations for this case. The movement and direction of flow depends on several parameters. When there are bends in either upstream or downstream within the microchannel or extended channel, they make the flow move upward or downward depending on the position and angle of the bend before the channel. There are also some other phenomena such as step flow, and the wake region at the corner of the channel can lead to periodic movements of the jet with low frequency due to separation effects (similar to

Karman vortex phenomenon). The detailed comparison of the cavitation inception between plain microchannel and D3 coating for smaller channels is shown in the Figure 3-5.

Figure 3-6 shows the pressures at the location of the vena contracta (P2) and Reynolds number ($\mathrm{Re} = \rho v_{\mathrm{ref}} D_{\mathrm{h}} / \mu$, where v_{ref} is the flow velocity and D_{h} is the hydraulic diameter), at cavitation inception for the surface configurations D1 and D3. The results illustrate that the P2 has a lower value for all the microchannels (CH X-here X stands for the number of the channels) for the coating D3 in comparison to the D1 device. The reduction in P2 becomes more for smaller microchannels for the coating D3 indicating the effect of the SLIPS on the inception and generation of the bubbles in larger channels. As seen, the results with SLIPS are more favorable in terms of earlier inception in comparison to the smaller channels.

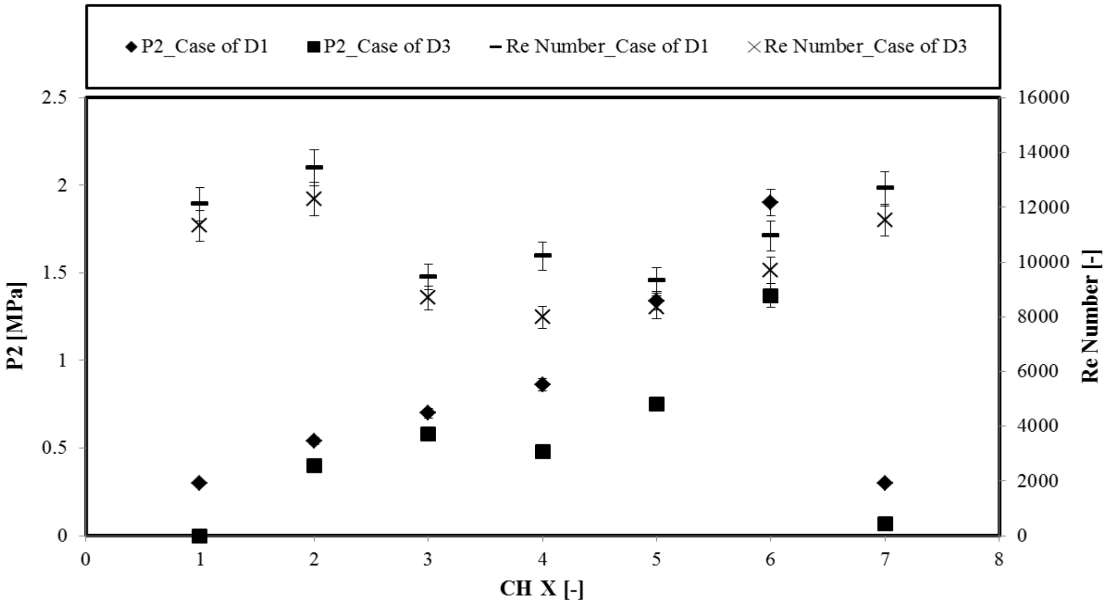

Figure 3-6 The variations in pressure at the location of vena contracta (P2) and Reynolds number for the cases of D1 and D3 at cavitation inception for different microchannels (X stands for the number of the channels)

The results of the Reynolds number also present a decreasing trend with the introduction of SLIPS coating to the microchannels, which implies earlier cavitation inception for the D3 coating. Furthermore, the Reynolds number values suggest turbulent flow conditions for all the cases, while its values for the smaller channels have smaller magnitudes. This suggests that the velocity of cavitating flows at the inception has higher values for the larger microchannels despite the lower pressure magnitudes compared to the smaller microchannels. As a result, the larger microchannel with D3 coating results in the most intense cavitation inception.

3-4-3 The effect of the LbL assembled SLIPS on the development of the cavitating flow

Figure 3-7 presents a qualitative comparison of flow pattern variations inside different microchannels for the D1 and D3 cases. The results show that the supercavitation condition exists for all the microchannels for the D3 coating, while this flow pattern is not visible in the case of D1 for some of the microchannels including the larger ones (e.g. CH2 and CH4). In addition, the supercavitation flow pattern appears at much lower upstream pressure values for the case of D3.

According to Figure 3-7, the large reduction in pressures to achieve supercavitation flows can be observed in the larger microchannels (CH1). Moreover, the results illustrate that for the longer side wall roughness elements with a reduction in the hydraulic diameter (CH4) for the D1 device, supercavitation cannot be seen even at high upstream pressure (7.23 MPa). However, supercavitation flow regime with intensified cavitating flows (even from the center of the channel) is observed in the smaller microchannels for the D3 device. This flow regime is also visualized for other channels, while the cavitation cloud generation from the center of the channel is observed in CH5 with a more intense behavior for the D3 device. This outcome demonstrates the effectiveness of the roughness elements in generating intense cavitation features in the micro scale. On the contrary, the roughness elements in the conventional channels are not as effective as in the microchannels [28]. As a result, along with the pressure rise, the roughness distribution induces intense turbulent flow conditions, which are accompanied with high surface tension in micro scale, providing an interesting flow regime filling almost the entire microchannel.

Figure 3-8 presents the flow rate variations for CH1 and CH5 with respect to the pressure drop. Flow rate has a constant value beyond the pressure drop of 3.9 MPa for the D3 coating, which marks the arrival of the supercavitation condition, while the flow rate is constant beyond the pressure drop of 5.9 MPa implying later arrival of the supercavitation condition in CH5.

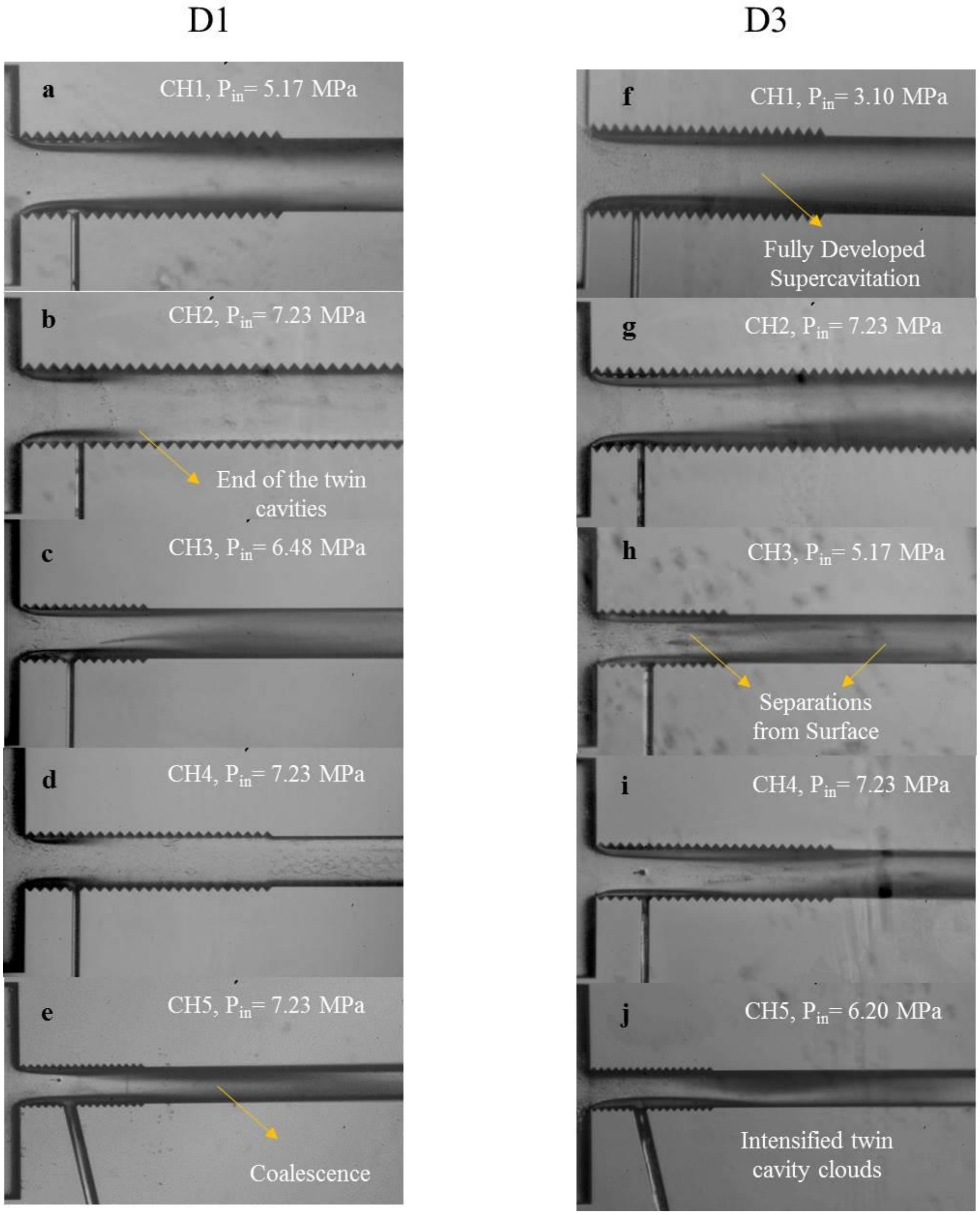

Figure 3-7 The comparison in the supercavitation flow regime inside different microchannels for the D3 coating with plain D1 microchannels

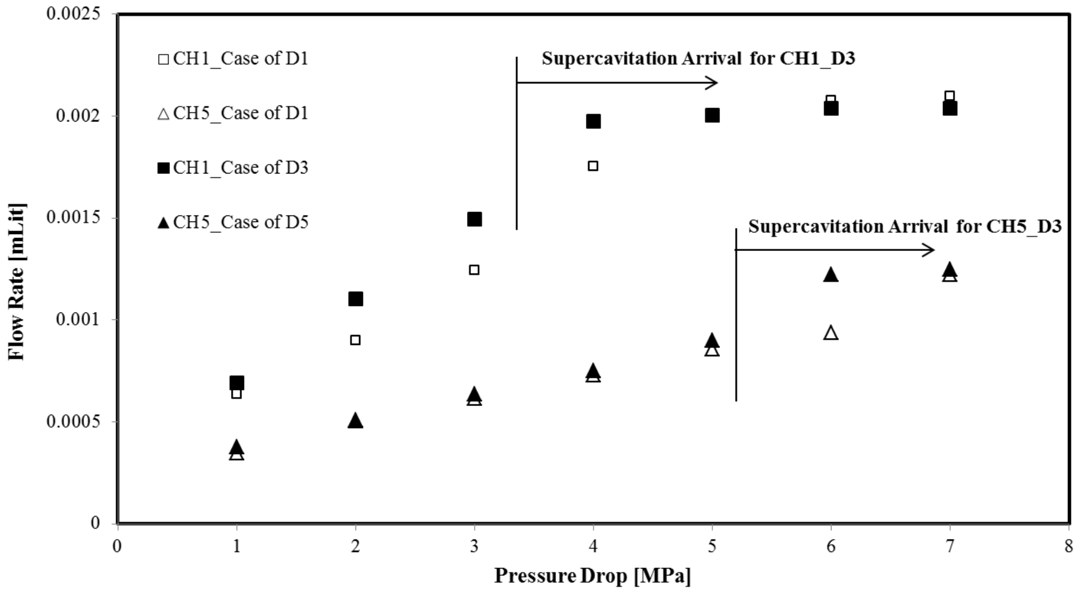

Figure 3-8 The flow rate variations in CH1 and CH5 as a function of pressure drop

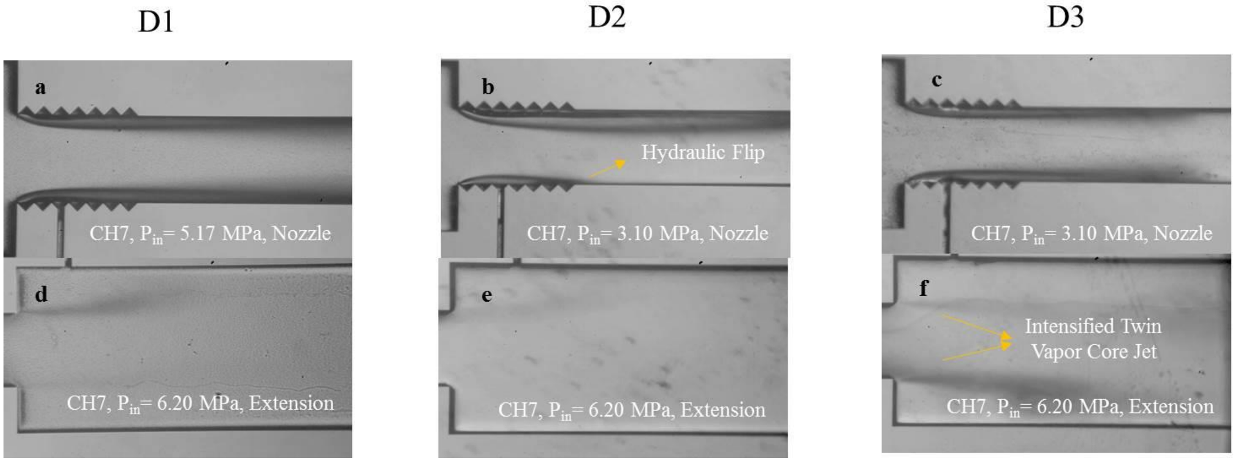

Figure 3-9 The cavitating flow patterns inside the microchannel and extended channel of the CH7 device for the configuration D1 and D2 and D3 coatings

The cavitating flow patterns in CH7 for the D1 device, and D2 and D3 coatings are shown in Figure 3-9, which displays the effect of the modified surface and the trapped lubricant on the bubble nucleation and following growth. Generated bubbles follow different paths to reach the extended channel and the targeted wall. Most of the cavitation bubbles survive and reach the extension part by passing through the liquid without touching the walls or the nozzle surface. The roughness elements provide favorable locations at the throat and even within the nozzle for nucleation of bubbles and also increase the probability of collapse in the cases of contact of the bubble with the surface or the walls of the nozzle. Lower inception and lower supercavitation pressures in D2 devices in comparison with the D1 devices prove that generation of bubbles in D2 devices is significantly enhanced and despite the collapse of the bubbles in the nozzle, supercavitation can be observed at the pressure 3.10 MPa (Figure 3-9). Comparing the results in the extended regions of D1 and D2 devices at 6.20 MPa reveals that the number of the survived bubbles is almost the same. This means that most of the bubbles generated inside D2 channels collapse. As the only difference between D1 and D2 devices is the roughness of the surface, the roughness of the surface in the channel not only increases the amount of generated bubbles but also plays a dominant role in the collapse of the bubbles. Although D1 devices generate lower amount of bubbles, most of them survive either by passing directly through the fluid or by bouncing the surface without rupture. The chance of the survival of the cavitation bubbles can be clearly visualized from the extension region. For instance, the extension region of CH7 channels at upstream pressure 5.17 MPa is presented in Figure 3-9. It is obvious that the bubbles in D2 devices collapse before reaching the extension region and D3 devices protect the bubbles from collapse and enhance the delivery and the density of the bubble cloud to the extension region.

Introducing the lubricant to the devices and trapping it within the pores of D2 devices and developing SLIPS D3 devices make the surface smoother and more favorable for the cavitation bubble protection. Tang et al. [9] claims that the lubricant wraps the surface of the bubble with a very thin layer of oil and protects it from pressure fluctuations or rough conditions. The colliding bubbles with the surface of SLIPS are pinned onto the surface, and the cloak-wise layer of the lubricant lowers the chance of collapse [9, 12]. Therefore, the cavitation bubbles survive along the channel toward the extension region, and bubble delivery can be achieved.

Figure 3-9 shows a thorough comparison of the flow transition inside CH7 for the cases of D1, D2 and D3. This figure presents the effect of the SLIPS coating in reaching the fully developed supercavitation condition at a low upstream pressure. While the supercavitation is observed at the upstream pressure of 3.10 MPa for the D3 coating, separated cavity clouds are also observed at the higher upstream pressure (6.20 MPa) from the center of the microchannel although CH7 is relatively large in terms of hydraulic diameter. Another interesting pattern is observed for the upstream pressure higher than 4.13 MPa for the D2 coating, which is called hydraulic flip. It is a rare pattern, which happens when the cavity cloud reaches the outlet of the microchannel, and the air flow existing at the extended channel tries to find a way in order to fill the entire boundary of the channel. This backflow occurs for the D2 coating implying the existence of the air passage replacing the main jet flow from the wall of the microchannel. During this phenomenon, the water jet is separated from the cavitating flow area and is of great importance in different industrial applications such as hydro-entangling, where uniform fibers form via water jets. To our best knowledge, hydraulic flip is seen for the first time in micro scale in this study.

Figure 3-10 illustrates the variations in cavitation number (σ) with respect to the vapor volume fraction (α_v) for two big and small channels for the cases of D1 and D3. The dimensionless cavitation number is expressed as, $\sigma = \mathrm{P_{ref}} - \mathrm{P_v}/0.5\rho \mathrm{V_{ref}^2}$, $\mathrm{P_{ref}}$ is reference pressure, which is the upstream pressure in this study, $\mathrm{P_v}$ is vapor saturation pressure and $\mathrm{V_{ref}}$ is the reference velocity at the outlet of the microchannel, which was calculated using the mass flow rate. Here, vapor volume fraction is found with the aid of the liquid, vapor and mixture densities. The latter was obtained by dividing mass flow rate by volumetric flow rate. The mass flow rate was obtained by measuring the mass of the fluid within the specified time period. The microchannels with SLIPS have lower cavitation numbers and higher values of vapor volume fractions (Figure 3-10). The results show that the smaller microchannels (CH3 and CH5) for both cases of D1 and D3 have higher values for the vapor volume fraction, while the larger microchannels (CH1 and CH7) have instead higher cavitation numbers. This suggests that although the larger microchannels offer earlier inception and supercavitation, the smaller microchannels generate more intense cavitation and denser vapor phase specifically at higher upstream pressures (Figure 3-11). As a result, in spite of more intense cavitating flows for the smaller microchannels, the larger microchannels require less input energy regarding cavitating flows.

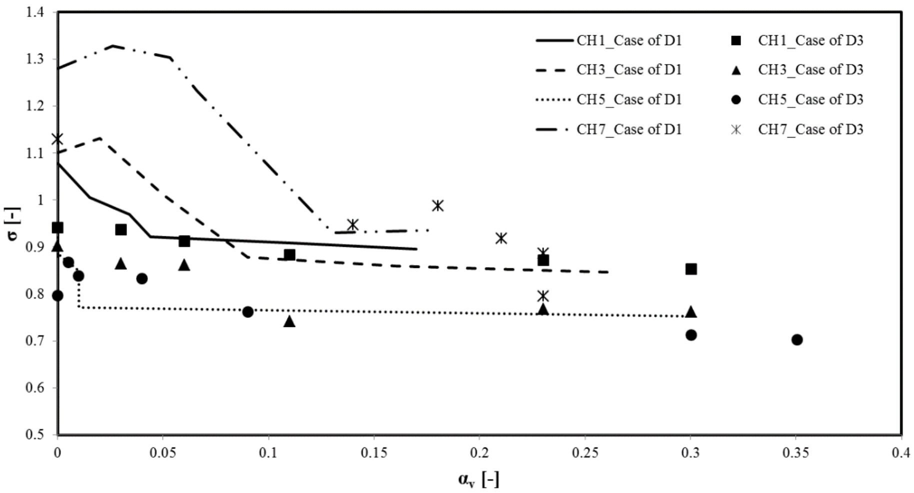

Figure 3-10 The variations in cavitation number as a function of vapor volume fraction in different microchannels for the D1 and D3 devices

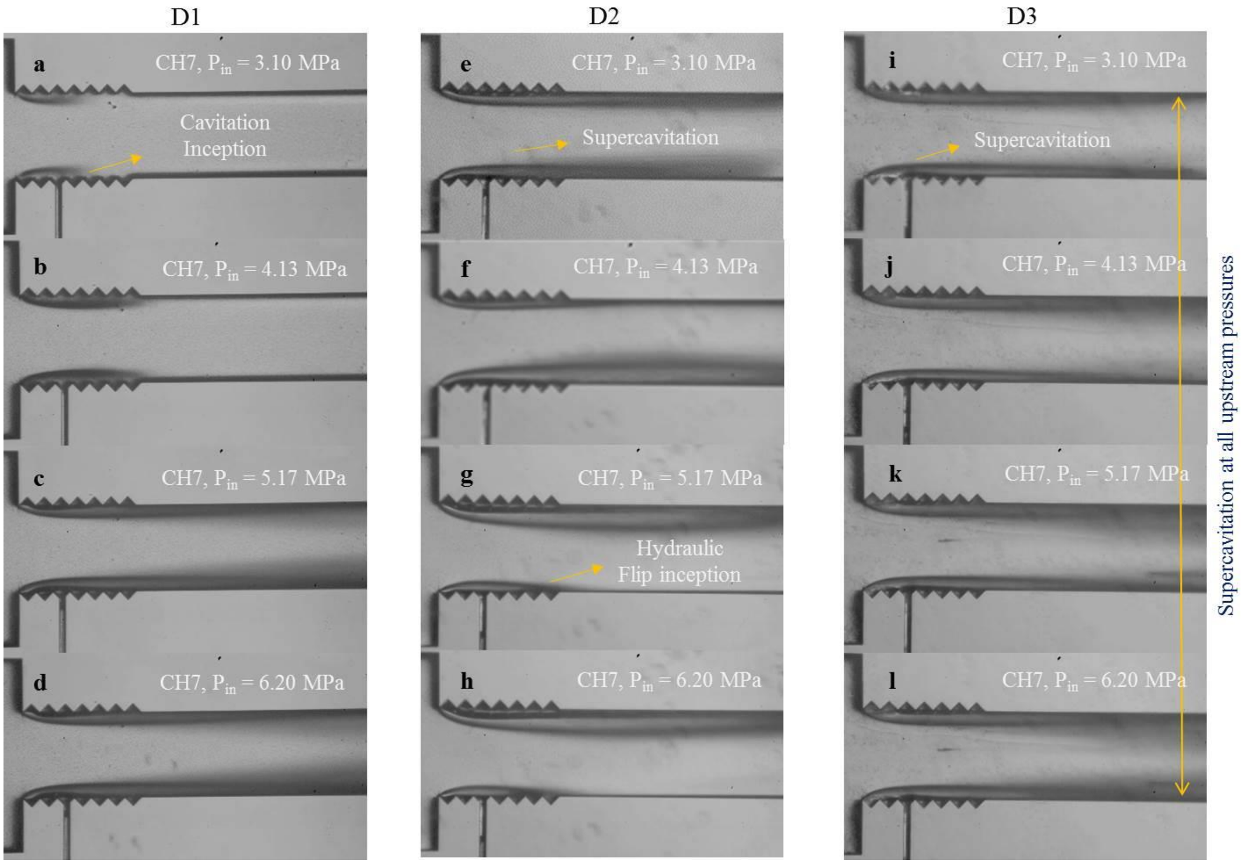

Figure 3-11 Comparison in the flow regimes inside CH7 at different upstream pressures for the D1, and D2 and D3 coatings

3-5 Concluding

In this study, SLIPS is presented as an effective method for earlier generation of cavitating flows, which is essential to decrease the input energy and increase the efficiency in microfluidic devices utilizing bubble clouds. While a less intense and earlier cavitation inception is observed inside the smaller microchannels (CH5 and CH6), more intense inception is captured in the extended channel region. The results show that the supercavitation condition is visible for all the microchannels for the D3 coating (with SLIPS), while this flow regime cannot be even recorded in some of the plain surface microchannels including the larger ones (e.g. CH2 and CH4). In addition, the supercavitation condition can be seen at a much lower upstream pressure for the D3 coating. Another interesting pattern, hydraulic-flip, which has not seen in micro scale before, is observed at upstream pressures higher than 4.13 MPa for the D2 coating (layer-by-layer assembly of silica nanoparticles).

The findings of this study will assist in facile cavitating flow generation with the aid of the cheap and facile surface modification techniques and utilization of cavitating flows in biomedical and energy applications.

3-6 References

1. Kim, P., et al., *Liquid-infused nanostructured surfaces with extreme anti-ice and anti-frost performance.* Acs Nano, 2012. **6**(8): p. 6569-6577.
2. Yong, J., et al., *Femtosecond laser induced underwater superaerophilic and superaerophobic PDMS sheets with through microholes for selective passage of air bubbles and further collection of underwater gas.* Nanoscale, 2018. **10**(8): p. 3688-3696.
3. Morteza, G., et al., *Hydrodynamic cavitation in microfluidic devices with roughened surfaces.* Journal of Micromechanics and Microengineering, 2018. **28**(7): p. 075016.
4. Cebeci, F.C., et al., *Nanoporosity-driven superhydrophilicity: A means to create multifunctional antifogging coatings.* Langmuir, 2006. **22**: p. 2856-2862.

5. Davis, A., et al., *Superhydrophobic Nanocomposite Surface Topography and Ice Adhesion.* ACS Applied Materials & Interfaces, 2014. **6**(12): p. 9272-9279.
6. Tenjimbayashi, M., et al., *Liquid-Infused Smooth Coating with Transparency, Super-Durability, and Extraordinary Hydrophobicity.* Advanced Functional Materials, 2016. **26**(37): p. 6693-6702.
7. Decher, G., *Fuzzy Nanoassemblies: Toward Layered Polymeric Multicomposites.* Science, 1997. **277**(5330): p. 1232-1237.
8. Sunny, S., et al., *Lubricant-Infused Nanoparticulate Coatings Assembled by Layer-by-Layer Deposition.* Advanced Functional Materials, 2014. **24**(42): p. 6658-6667.
9. Tang, X., et al., *Bioinspired Nanostructured Surfaces for On-Demand Bubble Transportation.* ACS Applied Materials & Interfaces, 2018. **10**(3): p. 3029-3038.
10. Ma, H., et al., *Directional and Continuous Transport of Gas Bubbles on Superaerophilic Geometry-Gradient Surfaces in Aqueous Environments.* Advanced Functional Materials, 2018. **28**(7): p. 1705091.
11. Yu, C., et al., *Superwettability of Gas Bubbles and Its Application: From Bioinspiration to Advanced Materials.* Advanced Materials, 2017. **29**(45): p. 1703053.
12. Yu, C., et al., *Manipulating Bubbles in Aqueous Environment via a Lubricant-Infused Slippery Surface.* Advanced Functional Materials, 2017. **27**(29): p. 1701605.
13. Mishra, C. and Y. Peles, *Cavitation in flow through a micro-orifice inside a silicon microchannel.* Physics of fluids, 2005. **17**(1): p. 013601.
14. Rooze, J., et al., *Hydrodynamic cavitation in micro channels with channel sizes of 100 and 750 micrometers.* Microfluidics and nanofluidics, 2012. **12**(1-4): p. 499-508.
15. Ghorbani, M., et al., *Experimental and numerical investigations on spray structure under the effect of cavitation phenomenon in a microchannel.* Journal of Mechanical Science and Technology, 2017. **31**(1): p. 235-247.
16. Ghorbani, M., et al., *Cavitating nozzle flows in micro-and minichannels under the effect of turbulence.* Journal of Mechanical Science and Technology, 2016. **30**(6): p. 2565-2581.
17. Ghorbani, M., et al., *Energy Harvesting in Microscale with Cavitating Flows.* Acs Omega, 2017. **2**(10): p. 6870-6877.
18. Suslick, K.S. and D.J. Flannigan, *Inside a collapsing bubble: sonoluminescence and the conditions during cavitation.* Annu. Rev. Phys. Chem., 2008. **59**: p. 659-683.

19. Nayebzadeh, A., et al., *Cavitation behind a circular micro pillar.* International Journal of Multiphase Flow, 2018. **98**: p. 67-78.
20. Malay, O., et al., *Polyurethaneurea–silica nanocomposites: Preparation and investigation of the structure–property behavior.* Polymer, 2013. **54**(20): p. 5310-5320.
21. Adams, T., C. Grant, and H.J.J.I. Watson, *A simple algorithm to relate measured surface roughness to equivalent sand-grain roughness.* 2012. **2929**: p. 2724.
22. Emerson Automation Solutions, *Fundamentals of Orifice Meter Measurement*. 2017.
23. Ghorbani, M., et al., *Visualization of microscale cavitating flow regimes via particle shadow sizing imaging and vision based estimation of the cone angle.* Experimental Thermal and Fluid Science, 2016. **78**: p. 322-333.
24. Todorov, R., et al., *Microstructure and ellipsometric modelling of the optical properties of very thin silver films for application in plasmonics.* Thin Solid Films, 2017. **628**: p. 22-30.
25. Hao, J., M. Zhang, and X. Huang, *The influence of surface roughness on cloud cavitation flow around hydrofoils.* Acta Mechanica Sinica, 2018. **34**(1): p. 10-21.
26. Li, J., et al., *Slippery Lubricant-Infused Surfaces: Properties and Emerging Applications.* Advanced Functional Materials, 2018. **0**(0): p. 1802317.
27. Wang, L., J. Wei, and Z. Su, *Fabrication of Surfaces with Extremely High Contact Angle Hysteresis from Polyelectrolyte Multilayer.* Langmuir, 2011. **27**(24): p. 15299-15304.
28. Arndt, R.E. and A.T. Ippen, *Rough surface effects on cavitation inception.* Journal of Basic Engineering, 1968. **90**(2): p. 249-261.

Chapter Four

Facile Hydrodynamic Cavitation ON CHIP via Cellulose Nanofibers Stabilized Perfluorodroplets inside Layer-by-Layer Assembled SLIPS Surfaces

Published in Chemical Engineering Journal:

Ghorbani, M., Aghdam, A. S., Gevari, M. T., Koşar, A., Cebeci, F. Ç., Grishenkov, D., & Svagan, A. J. (2020). Facile hydrodynamic cavitation ON CHIP via cellulose nanofibers stabilized perfluorodroplets inside layer-by-layer assembled SLIPS surfaces. Chemical Engineering Journal, 382, 122809

doi.org/10.1016/j.cej.2019.122809.

Abstract

The tremendous potential of “hydrodynamic cavitation on microchips” has been highlighted during recent years in various applications. Cavitating flow patterns, substantially depending upon thermophysical and geometrical characteristics, promote diverse industrial and engineering applications, including food and biomedical treatment. Highly vaporous and fully developed patterns in microfluidic devices are of particular interest. In this study, the potential of a new approach, which includes cellulose nanofiber (CNF)- stabilized perfluorodroplets (PFC5s), was assessed inside microfluidic devices. The surfaces of these devices were modified by assembling various sizes of silica nanoparticles, which facilitated in the generation of cavitation bubbles. To examine the pressure effects on the stabilized droplets in the microfluidic devices, the upstream pressure was varied, and the cavitation phenomenon was characterized under different experimental conditions. The results illustrate generation of interesting, fully developed, cavitating flows at low pressures for the stabilized droplets, which has not been previously observed in the literature. Supercavitation flow pattern, filling the entire microchannel, were recorded at the upstream pressure of 1.7 MPa for the case of CNF-stabilized PFC5s, which hardly corresponds to cavitation inception for pure water in the same microfluidic device.

Keywords: Hydrodynamic Cavitation; Perfluorodroplets (PFC5); Cellulose Nanofibers (CNFs); Pickering; Microfluidic Device; Layer-by-Layer Assembled

4-1 Introduction

Cavitation phenomenon has gained much attention in industrial and biomedical applications, due to its potential in the use for environmentally benign cleaning, energy harvesting and cancer treatment [1–3]. Cavitation phenomenon occurs due to a rapid change in static pressure within a liquid, whereupon gas-filled cavities are generated in the low-pressure region. Cavitation bubbles collapse when encountering the high-pressure region, and intense shock waves form, followed by a micro-jet generation from the center of the bubble. Size effects are important in the generation of cavitation phenomenon, and microfluidic systems are suitable platforms for fundamental studies to shed light on microscale cavitation phenomena [4,5]. The major differences between micro- and macro-scale hydrodynamic cavitation lie in cavitation inception, cavitation hysteresis and rapid transition to supercavitation flow pattern and choked flow [4,5]. There are several studies on parameters affecting the generation of cavitation phenomenon. Flow rate, cavitation number [6], Reynold (Re) number and inception of cavitation are the crucial parameters, which assist in understanding cavitation phenomenon [6–9]. Additionally, the working fluid plays an important role. For example, in the case of a mixture of ethanol and water, choking flow conditions could be obtained at very low cavitation numbers [10].

The formation of cavitating flows in microfluidic systems leads to high temperature gradients and enhanced thermal effects [11], and thermal energy generation is possible due to bubble collapse on the wall of microfluidic devices [12]. Recently, it was shown that the generation of cavitation bubbles and collapse of the bubbles are affected by thermophysical properties of the working fluids as well as the surface topology of the channels inside the microfluidic device [13]. Controlling these parameters helped researchers to develop microfluidic devices capable of generating intensified cavitating flows while decreasing the required energy for achieving the supercavitation flow pattern [14]. As a result, large amount of thermal energy could be generated from a small scale cavitation phenomenon, which could potentially fulfill personal energy needs in environmental friendly fashion.

Inspired by the need for clean energy, the focus in this study is on further intensifying the cavitation phenomenon, in order to generate larger temperature gradients, which is achieved herein by including a new cavitation intensifying strategy. Indeed, cavitation could also potentially be intensified in the presence of rapidly expanding capsules. In this regard, we investigate the potential of particle-stabilized perfluoropentane (PFC5) droplets as cavitation intensifiers. Particle-stabilized droplets are much more stable compared to a surfactant stabilized droplet, because the particles do not easily detach from the O/W interface [15]. This makes particle-stabilized PFC5 droplets promising with the respect to storage stability, because droplets will not merge together into bigger droplets with time. In other words, it is possible to produce a device, where energy can be stored and then released "on demand" in the form of heat.

Here, we present a novel device, which combines a tailored microfluidic channel, ensuring fully developed cavitating flows at very low upstream pressures, together with a new class of cellulose nanofiber-stabilized PFC5 droplets, where the O/W interface is stabilized by the cellulose nanofibers (CNF). By evaluating the energy released from the collapse of the cavitation bubbles, we demonstrate that the CNF-stabilized PFC5 droplets, in combination with the tailored surface roughness of the microfluidics device, represent a unique device in terms of lateral heat release. In addition, as the cellulose nanofibers remain intact after energy release, the particle-stabilized droplets could potentially be regenerated and also stored before being used again.

4-2 Methods and Materials

4-2-1 Fabrication of the microfluidics device

All the microfluidic devices were fabricated out of double side polished silicon wafers with a thickness of 380 µm. A schematic of the fabrication protocol [16] is shown in Figure 4-1A. All the devices employed in this study have small and short side wall roughness elements, as reported in detail in the previous studies of the authors [14]. The microfluidic devices contain two major regions, namely a microchannel followed by an extension (extended channel) downstream of the microchannel. The flow restrictive element induces a sudden drop in pressure due to reduction in cross-sectional area so that small bubbles from the flow restrictive element can be generated due to hydrodynamic cavitation. In addition, the walls of the microchannels are equipped with three pressure sensors to measure the local pressures at the locations (shown as P_1, P_2 and P_3 in Figure 4-1 B), namely before the entrance of the restrictive element, vena contracta (D_h) and entrance of the extended channel ($5D_h$-$8D_h$) [17]. Two microfluidic devices with different hydraulic diameters and side wall roughness length were employed in this study. These elements were formed as a structural roughness according to the geometry design. The detailed properties of these devices are listed in Table 4-1. Meanwhile, the equivalent sand-grain roughness (k_s) was calculated as 5.863

µm using the algorithm presented by Adams et al. [18], which is suitable for low measured roughness values.

Table 4-1 Dimensions for the different parts of the microfluidic devices

Microfluidic device	**Microchannel hydraulic diameter, D_h [µm]**	**Side wall roughness Length**	**Side wall roughness Height**
CH1	66	0.3L	$0.01D_h$
CH2	75	0.5L	$0.01D_h$

4-2-2 Surface Modifications of the device

4-2-2-1 Materials used for surface modifications

Tetraethyl Orthosilicate (TEOS), Ammonia hydroxide solution 25%, 2-Propanol 99.5% (IPA), Poly(sodium 4-styrenesulfonate), average Mw ~70,000 (SPS), Poly(allylamine hydrochloride), average Mw 50,000 (PAH), 1H,1H,2H,2H-Perfluorodecyltriethoxysilane 97% (PFDTS) were purchased from the Sigma Aldrich company. Fomblin Y LVAC 25/6, average molecular weight of 3.300 (PFPE) was purchased from the Solvay company.

4-2-2-2 Synthesis of silica particles

The modified Stöber method was employed to synthesize monodispersed Silica NPs as de- scribed in literature [19]. The zeta potential and diameter of the nanoparticles, which were tuned by the ratio of $[TEOS]/[NH_3]_{aq}$, were measured using the Dynamic Light Scattering (DLS) technique (Malvern Zetasizer Nano ZS). The silica nanoparticles were synthesized in a bath with $[TEOS]/[NH_3]_{aq}$ ratio of 4. The diameter, PDI and zeta potential of the particles were measured as 100 nm, 0.050 and -37.5 mV, respectively.

4-2-2-3 Surface modification with the use of silica particles

The silica particle coating in the interior of the microfluidics device was achieved by depositing several layers of PAH and SPS polyelectrolytes as adhesion layers, and then PAH and NPs layers, to achieve the desired rough surface, were formed on the substrates using the layer-by-layer method. In total, 30 bilayers were needed to achieve the desired surface roughness. The surface tension was adjusted using PFDTS to trap Fomblin YL VAC 25/6 lubricant within the pores of the surface.

4-2-3 Preparation of Cellulose nanofibers (CNFs)

Never-dried bleached sulfite pulp (Nordic Paper Seffle AB, Sweden) was used to obtain the cationic quaternary ammonium salt modified cellulose nanofibers (CNFs). A 1.32 wt% CNF suspension in water was prepared as previously described [20,21]. The amount of cationic groups residing on the CNF surface was 0.13 mmol per g fiber, obtained by conductometric titration [20,22]. The CNFs have already been characterized in a previous study and had a width of ca. 4 nm and their length was in the micrometer range, which was assessed by TEM [20]. However, bigger fiber aggregates could also be observed with TEM [20].

4-2-4 Preparation of CNF-stabilized PFC5 droplets

The stock CNF was diluted with MilliQ-water to obtain a 0.28 wt% suspension of CNF. The pH was adjusted to 9.5. To disperse the CNFs, the suspension was treated an ultrasonic liquid processor (Sonics Vibracell W750, U.S.) at an amplitude of 90% for 180 s (using a ½” tip), as previously described [20]. The suspension was brought to room temperature and afterwards 36 g of the attained CNF suspension was mixed with 1 g of PFC5. Afterwards, the mixture was processed for another 60 s at an amplitude of 80% under ice-cooling to obtain the stock suspension of CNF-stabilized PFC5 droplets. The droplets were imaged after ca. 1 h with a Light microscopy (VisiScope, VisiCam 16 Plus camera, VWR, Sweden).

4-3 Characterization

4-3-1 Atomic force microscopy (AFM)

Nanomechanical properties of the thin films and surface topography were assessed by Bruker multimode 8 Atomic Force Microscope (AFM). The height images were captured using NanoAndMore tips with a bending spring constant of 40 N m^{-1}, resonance frequency of 50-200 kHz, and tip radius of 10-20 nm, and the mechanical properties were assessed using tips with bending spring constant of 200 N m^{-1} resonance frequency of 500-600 kHz, and tip radius of 25-35 nm. The minimum deformation of the surface in nanomechanical properties evaluation was set as 2-5 nm, and the scan rate was 0.5-1 Hz. The height images of the CNFs were captured (ScanAsyst mode in air) with a Bruker NanoScope V (U.S.A.). A diluted drop of the CNF suspension (ca. 0.003 wt%) was dropped on cleaned silicon-wafer, allowed to settle for 3 min and then removed and dried with nitrogen gas. All images were processed using procedures for plane-fit and flattened.

4-3-2 Scanning electron Microscopy (SEM)

The surface morphology of samples was imaged with the Field Emission Scanning Electron Microscopy (FE-SEM, LEO Supra VP-55). The samples were sputter-coated with a (~10 nm) thick coating of Au/Pd prior to imaging.

4-3-3 Ellipsometry measurements

Woollam Co. M2000 ellipsometry was used to measure and model the thickness and the porosity of the films. The wavelength of the light, which has been used to conduct the ellipsometry measurements, was in the range of 380 to 780 nm (∼1.6–3.3 eV). The porosity of the thin film was modeled using the Bruggeman effective medium approximation (EMA) with ellipsometry [23].

4-3-4 Contact angle measurements and contact angle hysteresis

The hydrophobicity of the films was assessed by contact angle and contact angle hysteresis (CAH) measurement using Attension Theta Lite (Biolin Scientific, Finland). 5µL of distilled water (18.2 MΩ·cm) was accumulated on the tip of the needle and then released on the surface. By increasing and decreasing the volume of water residing on the surface and measuring the maximum and minimum contact angles, the contact angle hysteresis was calculated. The reported values are the average of three measurements for each sample type.

4-3-5 Cavitation experiments

The glass wafer on the modified microfluidic devices assists in visualizing flows inside the microfluidic devices. The experiments were conducted by applying different inlet pressures. The inlet pressure was varied from 1 to 7.23 MPa, while the outlet pressure at the microchannel was fixed to 0.1 MPa. The volumetric flow rate was increased with the change in the inlet pressure. Concentration and volume fraction of the CNF-stabilized PFC5 droplets employed in this study have values of approximately 0.027 vol% and 10^8 droplets mL^{-1} at room temperature. Cavitating flows generated in the microchannel were visualized at different regions in the microfluidic devices. The whole steps of the visualization experiments were explained in detail in the previous study of the authors [16].

4-4 Results and Discussion

4-4-1 Surface modification by layer-by-layer (LBL) assembled silica nanoparticles

The channels in the microfluidics devices, fabricated using the process flow shown in Figure 4-1A, went through a surface modification to achieve a rough surface consisting of silica nanoparticles. The coating was prepared by the layer-by-layer method, where polyelectrolytes, as intermittent layers in the build-up of the multilayer coating, were deposited on the surface of the device as shown in Figure 4-1B. The roughness and surface topography of the coating were assessed using Scanning Electron Microscopy (SEM) and Atomic Force Microscopy (AFM) (Figures 1B and C). The average thickness attained from nine points on the thin coating was 110 nm, measured using a profilometer. This value is consistent with the results from ellipsometry (114 nm). The void percentage of the film was estimated as 10% with a mean square error (MSE) of 7% using the Bruggeman effective medium approximation (EMA). These results were further confirmed with SEM images of the surface at two different magnifications, Figure 4-1B. The porosities were estimated numerically from the ellipsometry and SEM measurements. Nano and micro-scale roughness of the surface is not only an important parameter that influences the surface energy of the coating, which in turn affects the hydrophobicity, but it also provides pores for the lubricant to penetrate into the coating. AFM height images and results (Figure 4-1C) proved that these surfaces were rough both on the nano- and micro-scale. The increase in the projected surface is reported as 9% in both scales, and the root mean square is measured as 35.4 nm and 11 nm on the micro- and nano-scale, respectively. The Young modulus of elasticity of the thin film on silicon wafers was 5 GPa, which ensures high durability of the coating under the present working condition.

Static contact angle and contact angle hysteresis measurements reveal the hydrophobic nature of the surface (after the application of the lubricant). The lubricant covers the surface with a very thin layer. As the contact angle of the water droplet and air bubble on a surface are supplementary angles, it can be predicted that the behavior of both of them on this surface is almost the same, and air bubbles have a contact angle of 80° with a low contact angle hysteresis of about 5°, which implies that gas bubbles can easily slide on the surface [24].

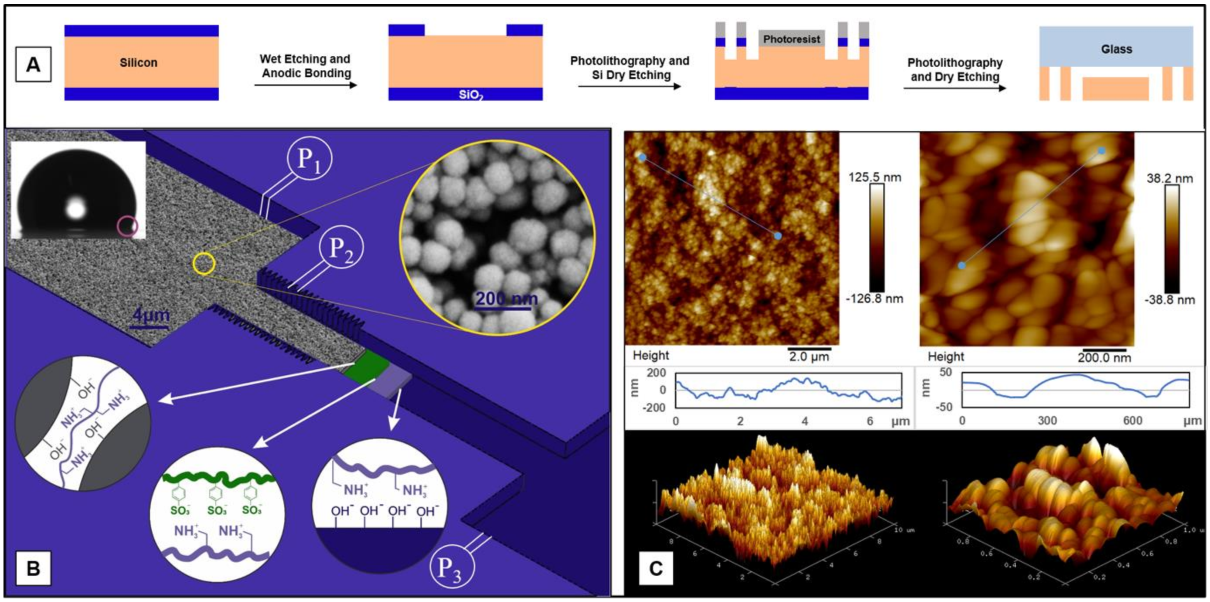

Figure 4-1 Assembly of the microfluidics device. Schematic overview of (A) fabrication process flow for the microfluidic device (B) assembled layers of thin film on the microfluidic device and SEM image of the final thin film (C) 2D and 3D height images of atomic force microscopy representing the nano and microscale roughness of the surface.

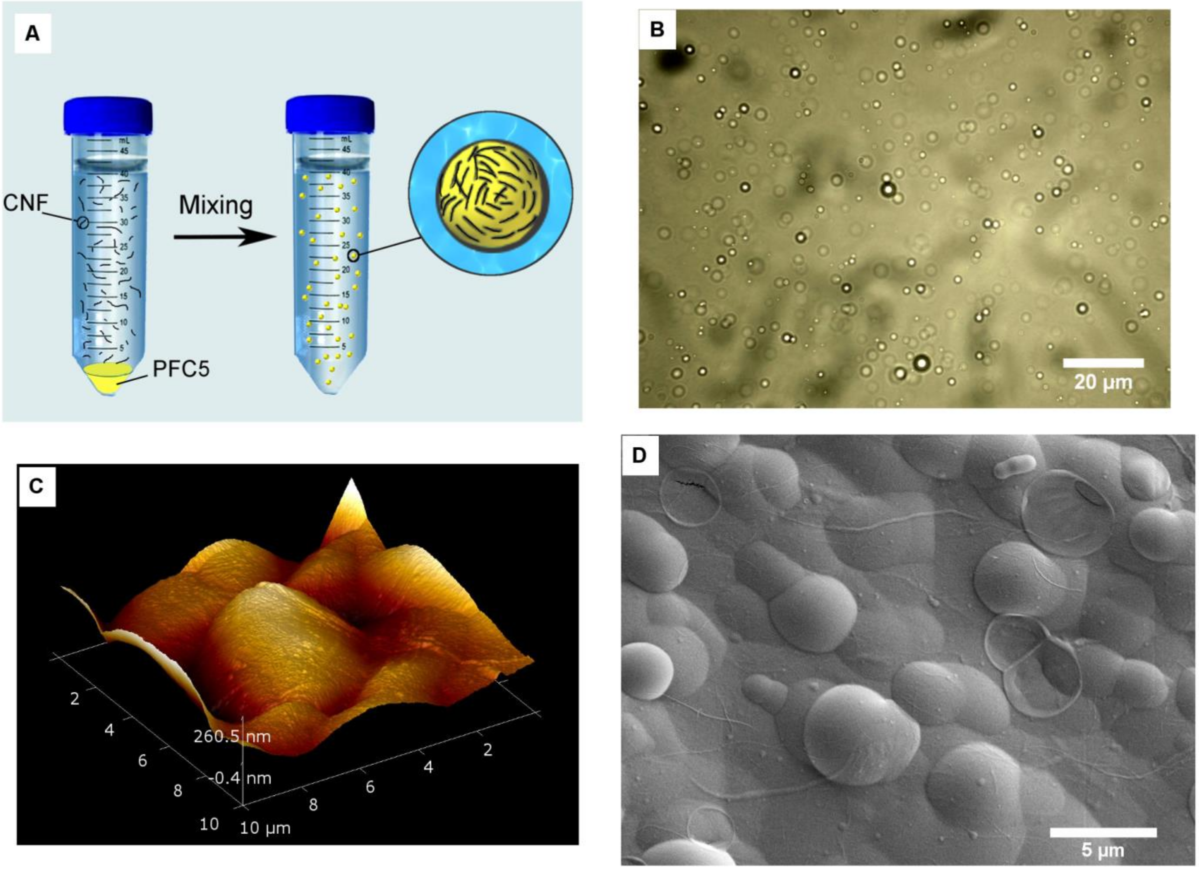

Figure 4-2 Assembly of the CNF-stabilized PFC5 droplets. Particle stabilized droplets were prepared by (A) mixing a CNF suspension in MilliQ water with PFC5 to obtain the CNF stabilized droplets. (B) Light microscopy image of the resulting CNF-stabilized PFC5 droplets (imaged ca.1 h after preparation). Droplets were deposited and dried at ambient conditions and imaged using (C) AFM and (D) SEM.

4-4-2 Assembly of CNF-stabilized PFC5 droplets

The CNF stabilized PFC5 droplet were prepared via a straightforward and simple mixing protocol, where a cationic CNF suspension is mixed with PFC5, whereupon stable micro-sized droplets in a comparatively narrow size distribution are achieved, ca. 1-5 µm in size (Figure 4-2A and B). The size distribution can be compared with the droplet distribution in surfactant stabilized systems, where the size distribution is typically more polydisperse, ranging over a few orders of magnitude (when the droplets are generated with some types of high energy mixing protocol). The CNF stabilized the O/W interface via a Pickering mechanism as demonstrated in a previous study [25].

In Figure 4-2C and D, the particle-stabilized droplets were imaged after drying with AFM and SEM, respectively. Interestingly, the capsule structures did not completely collapse under ambient or high-vacuum conditions in the SEM despite that PFC5 will unavoidably evaporate under such conditions. A nanocellulose composite microcapsules at low polymer content in the shell (and initially filled with hexadecane) will completely collapse under SEM conditions [26,27]. Herein, a bulged (half-collapsed) capsule structure was observed, Figure 4-2C-D, which consisted of a dense CNF layer, see SEM image in Figure 4-2D.

4-4-3 Hydrodynamic cavitation measurements

The pioneering studies on hydrodynamic cavitation on microchips have mostly been devoted to the physics of cavitation on the micro-scale [4]. The surface roughness is effective for the generation of cavitation in the micro-scale [13]. The device reduces the required pressure drop for achieving fully developed supercavitation flow patterns. The side wall roughness elements in the channels affect cavitating flows by inducing secondary flows such as turbulent Taylor vortices, while generating large stable vertical structures, as shown in Figure 4-3. Therefore, the bubbles keep out of the boundaries, and the vapor phase extends along the length of the channel, which is in line with the previous results [13].

The introduced CNF-stabilized PFC5s generate a highly vaporous cavitating flow, which fills the entire microchannel at a much lower upstream pressure (Figure 4-3A). To the best of the authors' knowledge, this has not been previously reported [13,14]. According to Figure 4-3A and B, the droplets give rise to the supercavitation flow pattern at the upstream pressure of 1.7 MPa, while developed cavitating flow with the penetration length of approximately 0.8 mm is observed for the case of water at the pressure of 7.23 MPa. It should be noted that inception of cavitating flow is observed at the upstream pressure of 1.7 MPa for the case of water. The generation of larger cavity clouds (supercavitation), as shown in Figure 4-3A, leads to intense turbulence due to the collapse of some of the bubbles inside the microchannel, which assists in promoting collapse. Moreover, this pattern results in smaller bubble generation in size [28], while the cavity cloud covers the whole volume of the microchannel, thereby generating large temperature gradient.

Due to the low saturation temperature of these droplets (approximately 29 °C), we hypothesize that vaporization will have an additional effect on the flow. Furthermore, the surface tension gradient, induced by the concentration gradient of the dissolved content in the solution, and the generated temperature gradient, substantially reduce the inception pressure for the cavitation phenomenon. As a result, the surface tension effect leads to density gradients, which trigger convective flows in the droplet suspension. These phenomena cause the main flow to be controlled by gravitational forces at low upstream pressure and radial velocity resulting in the slight flow diversion from its regular direction in the extended channel. This flow pattern is observed inside the extended channel for the case of PFC5 droplets and water (Figure 4-4A and B) at the upstream pressure of 2.3 MPa. Strong vortices are observed first at the upstream pressure of 2.3 MPa for the case of PFC5 droplet suspension, which are not observed in the case of water at the same upstream pressure. The generated cavitating flow inside the microchannel with PFC5 droplets has a relatively higher mean velocity (45 m/s), which was measured according to the volume flow rate obtained from the experiments, thereby minimizing the buoyancy effects, which is dominated by the surface tension and generated vortices.

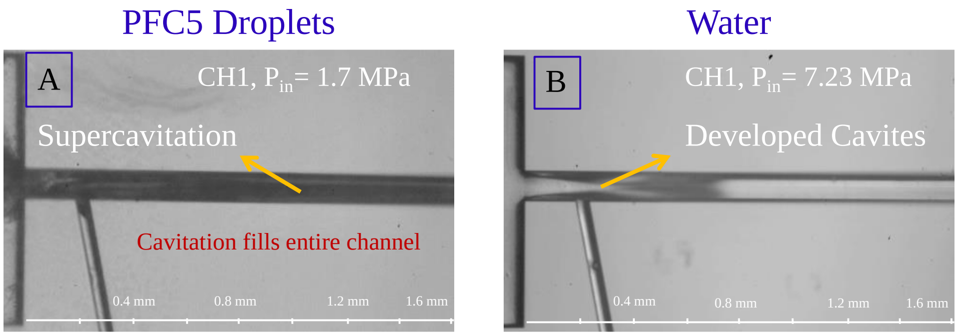

Figure 4-3 The cavitating flow patterns inside the same microchannel (CH1). (A) supercavitation flow pattern at upstream pressure of 1.7 MPa for the case of PFC5 droplets in water (B) developed cavitating flow at upstream pressure of 7.23 MPa for the case of water.

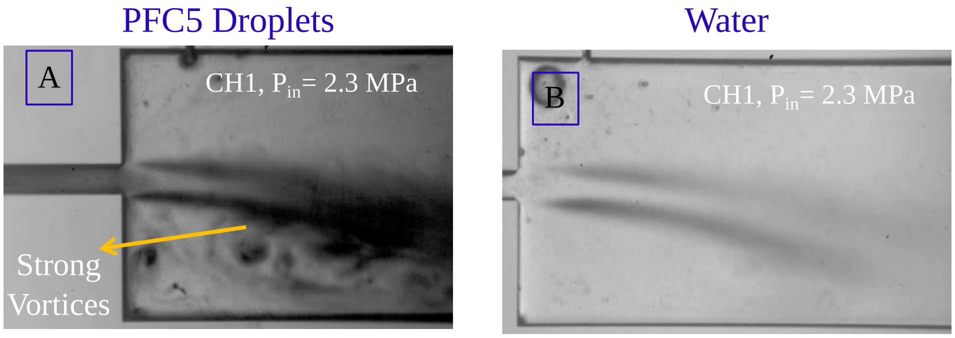

Figure 4-4 The cavitating flow patterns inside the same microfluidic device (CH1). (A) penetration of twin cavities to the extended channel with a view of the microchannel downstream at the upstream pressure of 2.3 MPa for the case of PFC5 droplets (B) penetration of twin cavities to the extended channel at the upstream pressure of 2.3 MPa for the case water.

PFC5 droplets are also introduced into another microfluidic device (CH2) with a hydraulic diameter of 75 µm ($D_h = 4A/P$, where A is the cross-sectional area and P is the perimeter of the microchannel) to compare the flow patterns in geometrically different devices (CH1 and CH2) and to characterize cavitating flows with non-dimensional parameters. The two microfluidic devices were optimized with respect to the intense cavitation generation, see details in the previous studies with water and PVA microbubbles [13,14]. Figure 4-5 shows the comparison between these devices, presented with Re, We and cavitation numbers. Accordingly, the cavitation inception occurs at relatively lower upstream pressure (1.12 MPa) and cavitation number, ($\sigma = \mathrm{P_{ref}} - \mathrm{P_v}/0.5\rho_\mathrm{l}\mathrm{V}_\mathrm{ref}^2$, where ρ_l is liquid density, $\mathrm{P_{ref}}$ is reference pressure, which is the upstream pressure in this study, $\mathrm{P_v}$ is vapor saturation pressure and $\mathrm{V_{ref}}$ is the reference velocity at the outlet of the microchannel, which was calculated with the use of mass flow rate), (4.28) for CH1 compared to CH2, where the upstream pressure is 1.67 MPa, and σ is 7.28. It should be noted that high values of σ in this study are due to the fact that all of the flow patterns appear at rather low upstream pressures and consequently lower mean velocities inside the microfluidic devices. While Re and We numbers ($Re = \rho \mathrm{v}_{ref} D_h/\mu$, and $We = \rho v_{ref}^2 D_h/\sigma$, where σ is the liquid surface tension) are almost in the same range for both devices, Re numbers suggest transient flow at the time of the inception.

The cavitation number differences between inception and developed cavitating flows for CH1 and CH2 are 1.34 and 4.17, respectively. This difference in cavitation numbers suggests that more cavitation bubbles are generated inside the smaller channel and intensified cavitating flow leads to the earlier appearance of the supercavitation flow pattern. Moreover, the Re numbers at points A and B (Figure 4-5) are 7258 and 9745, respectively, which implies that supercavitation arrives at lower Re numbers inside the smaller microchannel with hydraulic diameter of 66 µm (CH1). Although Re and We numbers are lower at point A compared to point B, they are higher for the smaller microchannel at the highest upstream pressure applied to the microfluidic devices. Thus, the mean velocity at the last stage has higher values for the smaller microchannel despite it having the same pressure magnitude as in the larger microchannel. In addition, very strong vortices are observed in the extended channels for both devices, which implies large pressure variations for PFC5 droplets even at lower upstream pressures. It should be noted that the cavitating flow pattern inside the device having the same hydraulic diameter as CH2 and the same side wall roughness length as CH1 is the same as in CH2, as the corresponding Re number is 9886 at the point B. Therefore, the variations in hydraulic diameter strongly affect the cavitating flow pattern. While supercavitation is observed for the smaller microchannel, hydraulic flip is seen at point B for the larger microchannel once the cavitating flow is developed. This flow pattern happens when the cavity cloud reaches the outlet of the microchannel, and the air flow existing at the extended channel tries to find a way in order to fill the entire boundary of the channel. The backflow observed at point B implies the existence of the air passage replacing the main jet flow from the wall of the microchannel. During this phenomenon, the water jet is separated from the cavitating flow area and this is of great importance in different industrial applications such as hydro-entangling, where uniform fibers form via water jets. To the best knowledge of the authors, hydraulic flip is seen for the first time on the micro-scale.

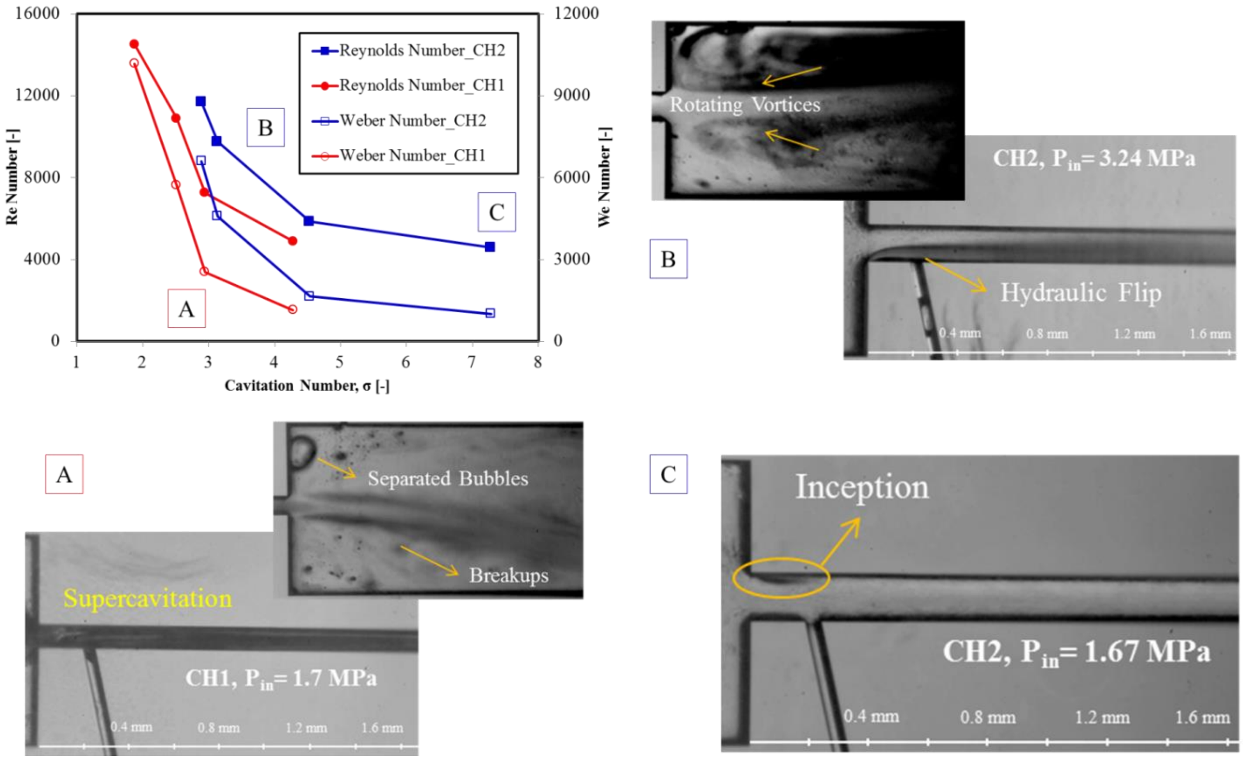

Figure 4-5 Cavitation patterns for PFC5 droplets in two different microfluidics devices (CH1 and CH2). The variation of Reynolds and Weber numbers as a function of the cavitation number for the cavitating flow with CNF-stabilized PFC5 droplets. Snapshots of the corresponding flow patterns at points A, B and C of the different curves are included.

In spite of the lower viscosity, sound speed and surface tension of PFC5 droplets compared to water, the supercavitation and hydraulic flip observed in these experiments occur at low upstream pressure for the case of PFC5 droplets.

The potential energy of the bubbles, which is a function of the size of the bubbles and the vapor pressure of the working fluid, transforms into other forms of energy upon collapse. Shock waves, as a result of the bubble burst, can be used in different fields such as pretreatment of biomass [29]. In an attempt to provide insight into cavitation bubble size, bubble diameter variation within a 7 µs time step is shown in Figure 4-6. At the points A, B, and C, the size of the bubbles gradually increases and reaches a maximum size of 10.5 µm in diameter. The size growth can be due to either the expansion of the gases inside the bubbles or flocculation and coalescences of the small bubbles at points B and C. This growth continues for 3 µs in the extension. The images from the

CCD camera show the disappearance of the bubbles, Figure 4-6 at point D. As can be seen, the rebound bubble size is infinitesimal. As a result, the rebound energy can be neglected, and the shock wave energy is proportional to the initial potential energy of the bubbles before the collapse [30].

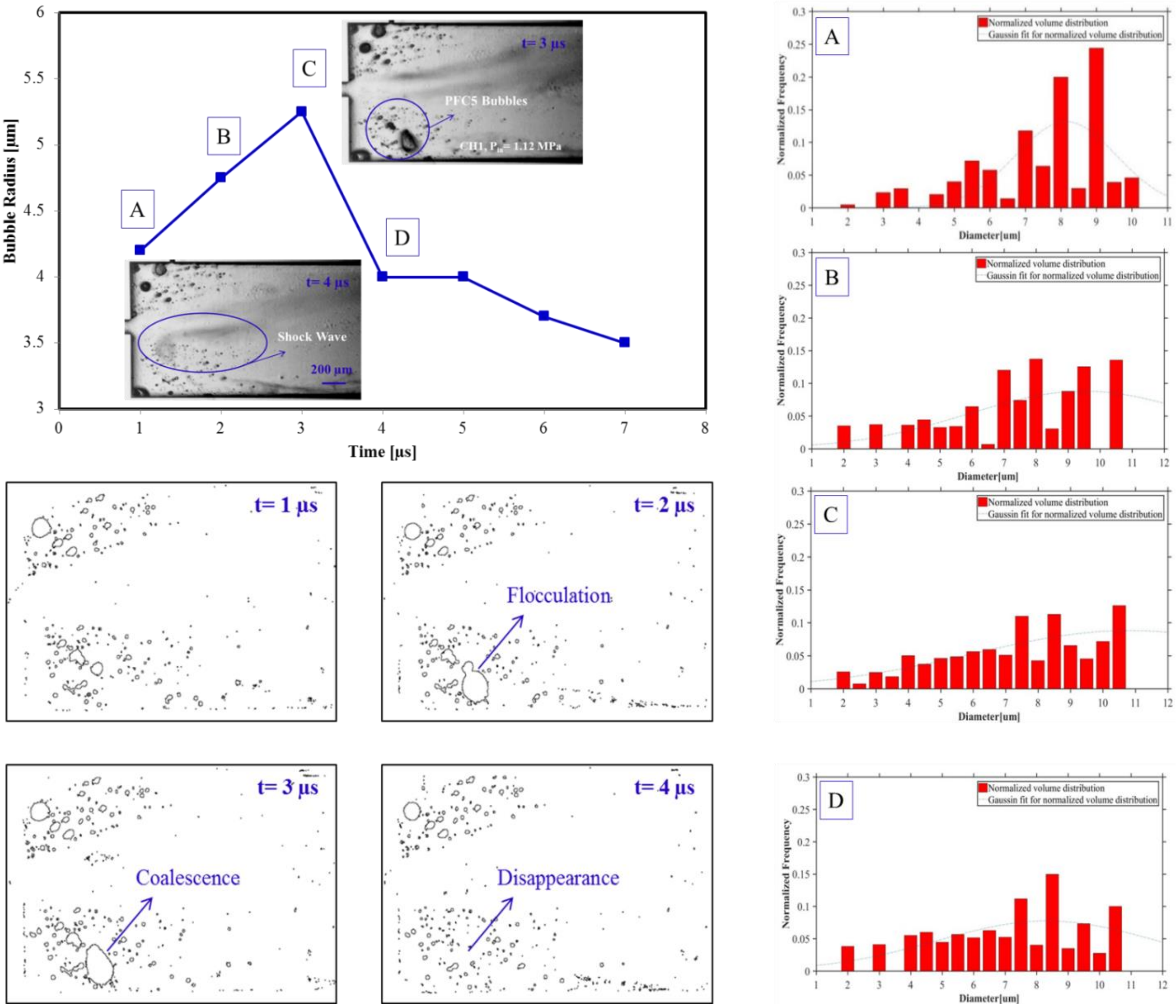

Figure 4-6 The fate of the PFC5 droplets during supercavitation. Bubble radius variations at the upstream pressure of 1.67 MPa inside the extension with shock wave manifestation. The microfluidic device, CH1, was used.

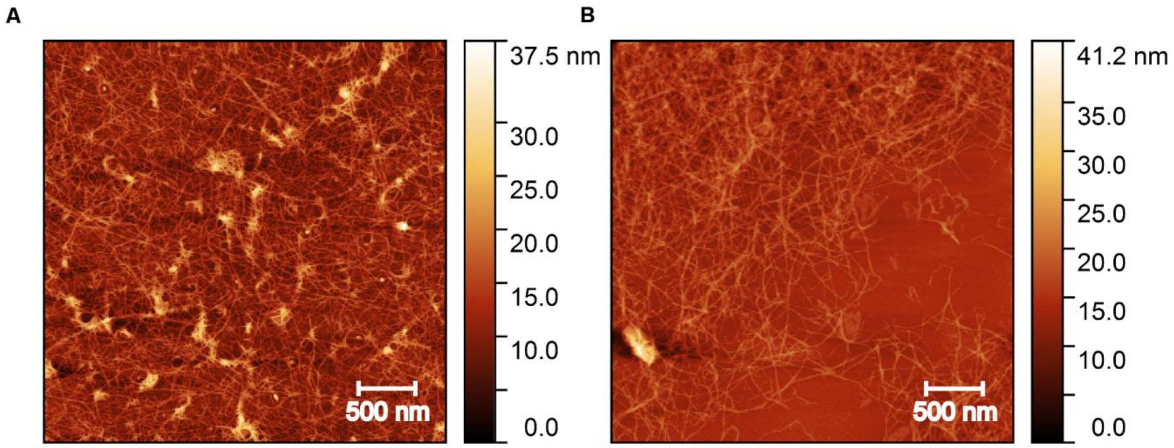

Figure 4-7 CNFs before and after supercavitation. AFM image of CNF (A) before and (B) after supercavitation.

After the supercavitation and destruction of the Pickering-stabilized droplets, it would be attractive to collect the PFC5 and CNFs and regenerate the CNF-stabilized PFC5 droplets. This is only possible if the cellulosic nanofibers are not significantly modified during supercavitation. We hypothesize that the modification should occur on the surface and in the more assessable amorphous regions of the CNFs, which might decrease the length of the CNFs. In Figure 4-7A and B the CNF nanofibers obtained after the supercavitation and the starting nanofibers are compared. Evidently, the CNFs have not been shortened and could be reused to create new PFC5 droplets. This constitute a prerequisite to create an efficient, closed-loop device, which can effectively store energy, release it on demand and finally be "recharged" by regenerating the droplets using a simple mixing step.

4-5 Conclusions

In this study, a new type of droplets, cellulose nanofiber-stabilized perfluoropentane droplets, were tested within a surface tailored microfluidic devices to generate cavitation bubbles in a facile way. The flow pattern with the highest intensity, i.e. supercavitation, was observed at a low upstream pressure of 1.7 MPa with these droplets, which barely corresponded to the cavitation inception for pure water. Moreover, hydraulic flip, which has not been previously recorded on the microscale, was generated for the larger microchannel in the presence of CNF-stabilized PFC5 droplets. The results also showed that more cavitation bubbles were generated inside the smaller channel configuration, and supercavitation flow pattern arrived earlier due to the smaller difference in cavitation number between the inception and developed cavitating flow in the smaller channel configuration. This outcome implies that the microfluidic device with a smaller hydraulic diameter, possesses the most intense cavitation generation at rather low upstream pressures for the case of PFC5 droplets. As the CNFs are not damaged, droplets can be regenerated; this study proposes an important approach towards a closed-loop device that can store energy, then release and be “recharged” on demand.

4-6 References

[1] B. Balasundaram, S.T.L. Harrison, Study of physical and biological factors involved in the disruption of E. coli by hydrodynamic cavitation, Biotechnol. Prog. 22 (2006) 907–913.

[2] D. Uzusen, E. Demir, O.Y. Perk, O. Oral, S. Ekici, M. Unel, D. Gozuacik, A. Kosar, Assessment of probe-to-specimen distance effect in kidney stone treatment with hydrodynamic cavitation, J. Med. Device. 9 (2015) 31001.

[3] M. Ghorbani, C. Sozer, G. Alcan, M. Unel, S. Ekici, H. Uvet, A. Koşar, Biomedical device prototype based on small scale hydrodynamic cavitation, AIP Adv. 8 (2018) 35108.

[4] C. Mishra, Y. Peles, Cavitation in flow through a micro-orifice inside a silicon microchannel, Phys. Fluids. 17 (2005) 13601.

[5] M. Dular, I. Khlifa, S. Fuzier, M.A. Maiga, O. Coutier-Delgosha, Scale effect on unsteady cloud cavitation, Exp. Fluids. 53 (2012) 1233–1250.

[6] C. Mishra, Y. Peles, An experimental investigation of hydrodynamic cavitation in micro-Venturis, Phys. Fluids. 18 (2006) 103603.

[7] J. Li, P. Cheng, Bubble cavitation in a microchannel, Int. J. Heat Mass Transf. 47 (2004) 2689–2698.

[8] M. Medrano, P.J. Zermatten, C. Pellone, J.-P. Franc, F. Ayela, Hydrodynamic cavitation in microsystems. I. Experiments with deionized water and nanofluids, Phys. Fluids. 23 (2011) 127103.

[9] C. Mishra, Y. Peles, Size scale effects on cavitating flows through microorifices entrenched in rectangular microchannels, J. Microelectromechanical Syst. 14 (2005) 987–999.

[10] R. Singh, Y. Peles, The effects of fluid properties on cavitation in a micro domain, J. Micromechanics Microengineering. 19 (2009) 25009.

[11] K.S. Suslick, N.C. Eddingsaas, D.J. Flannigan, S.D. Hopkins, H. Xu, Extreme conditions during multibubble cavitation: Sonoluminescence as a spectroscopic probe, Ultrason. Sonochem. 18 (2011) 842–846.

[12] M. Ghorbani, A. Mohammadi, A.R. Motezakker, L.G. Villanueva, Y. Leblebici, A. Kosar, Energy Harvesting in Microscale with Cavitating Flows, ACS Omega. 2 (2017) 6870–6877.

[13] M. Ghorbani, A.K. Sadaghiani, L.G. Villanueva, A. Koşar, Hydrodynamic cavitation in microfluidic devices with roughened surfaces, J. Micromechanics Microengineering. 28 (2018) 75016.

[14] M. Ghorbani, H. Chen, L.G. Villanueva, D. Grishenkov, A. Koşar, Intensifying cavitating flows in microfluidic devices with poly (vinyl alcohol)(PVA) microbubbles, Phys. Fluids. 30 (2018) 102001.

[15] A. Stocco, W. Drenckhan, E. Rio, D. Langevin, B.P. Binks, Particle-stabilised foams: an interfacial study, Soft Matter. 5 (2009) 2215–2222.

[16] M. Ghorbani, G. Alcan, M. Unel, D. Gozuacik, S. Ekici, H. Uvet, A. Sabanovic, A. Kosar, Visualization of microscale cavitating flow regimes via particle shadow sizing imaging and vision based estimation of the cone angle, Exp. Therm. Fluid Sci. 78 (2016) 322–333.

[17] E.A. Solutions, Fundamentals of orifice meter measurement, White Paper, 2017.

[18] T. Adams, C. Grant, H. Watson, A simple algorithm to relate measured surface roughness to equivalent sand-grain roughness, Int. J. Mech. Eng. Mechatronics. 1 (2012) 66–71.

[19] O. Malay, O. Oguz, C. Kosak, E. Yilgor, I. Yilgor, Y.Z. Menceloglu, Polyurethaneurea–silica nanocomposites: Preparation and investigation of the structure–property behavior, Polymer (Guildf). 54 (2013) 5310–5320.

[20] A.J. Svagan, J.-W. Benjamins, Z. Al-Ansari, D.B. Shalom, A. Müllertz, L. Wågberg, K. Löbmann, Solid cellulose nanofiber based foams–towards facile design of sustained drug delivery systems, J. Control. Release. 244 (2016) 74–82.

[21] S.L. Mølgaard, M. Henriksson, M. Cárdenas, A.J. Svagan, Cellulose-nanofiber/polygalacturonic acid coatings with high oxygen barrier and targeted release properties, Carbohydr. Polym. 114 (2014) 179–182.

[22] M. Hasani, E.D. Cranston, G. Westman, D.G. Gray, Cationic surface functionalization of cellulose nanocrystals, Soft Matter. 4 (2008) 2238–2244.

[23] R. Todorov, V. Lozanova, P. Knotek, E. Černošková, M. Vlček, Microstructure and ellipsometric modelling of the optical properties of very thin silver films for application in plasmonics, Thin Solid Films. 628 (2017) 22–30.

[24] C. Yu, P. Zhang, J. Wang, L. Jiang, Superwettability of gas bubbles and its application: from bioinspiration to advanced materials, Adv. Mater. 29 (2017) 1703053.

[25] M. Ghorbani, K. Olofsson, J-W. Benjamins, M. Wiklund, D. Grishenkov, A.J. Svagan,

Unraveling the Acoustic and Thermal Responses of Perfluorocarbon Liquid Droplets Stabilized with Cellulose Nanofibers, Langmuir. Accepted (2019).

[26] T. Paulraj, A. V Riazanova, K. Yao, R.L. Andersson, A. Müllertz, A.J. Svagan, Bioinspired layer-by-layer microcapsules based on cellulose nanofibers with switchable permeability, Biomacromolecules. 18 (2017) 1401–1410.

[27] A.J. Svagan, A. Musyanovych, M. Kappl, M. Bernhardt, G. Glasser, C. Wohnhaas, L.A. Berglund, J. Risbo, K. Landfester, Cellulose nanofiber/nanocrystal reinforced capsules: A fast and facile approach toward assembly of liquid-core capsules with high mechanical stability, Biomacromolecules. 15 (2014) 1852–1859.

[28] M.T. Shervani-Tabar, S. Parsa, M. Ghorbani, Numerical study on the effect of the cavitation phenomenon on the characteristics of fuel spray, Math. Comput. Model. 56 (2012) 105–117.

[29] R. Terán Hilares, L. Ramos, S.S. da Silva, G. Dragone, S.I. Mussatto, J.C. dos Santos, Hydrodynamic cavitation as a strategy to enhance the efficiency of lignocellulosic biomass pretreatment, Crit. Rev. Biotechnol. 38 (2018) 483–493.

[30] M. Tinguely, D. Obreschkow, P. Kobel, N. Dorsaz, A. De Bosset, M. Farhat, Energy partition at the collapse of spherical cavitation bubbles, Phys. Rev. E. 86 (2012) 46315.

Chapter Five

Conclusion and Outlook

5-1 Conclusion

In this dissertation, we have developed thin films of SLIPS on glass and silicon wafer substrates using dip coating and fluidic coating methods of layer-by-layer (LbL) self-assembly technique, which is also scalable and low cost. The deposited tetralayer thin film of PAH and SPS polyelectrolytes and silica nanoparticles on the substrate, and the infused fluorinated lubricant into the pores of the deposited thin film generated the transparent, icephobic and hydrophobic SLIPS. The roughness in the form of holes and cracks was contributed to the infusion of lubricant and helped to trap them inside longer even under challenging conditions. The homemade silica nanoparticles' diameter was varied by adjusting the ratio of the [TEOS]/[NH3]aq where the average NP sizes were measured to be within a range of 30 to 140 nm. The thickness of the thin films was about 200 nm, and AFM and SEM images confirmed that the surfaces of the thin films are rough at both micro and nanoscale (Rq: 30 and 15 nm respectively), enabling them to act as a reservoir for the lubricant. The young modulus of the coatings was optimized by using a mixture of 40 and 80nm silica nanoparticles in diameter as 5.3 Gpa. The Weibull distribution model was applied to assess and compare the effect of the thin films and SLIPS on the ice adhesion force. The results showed that the adhesion strength of the ice to SLIPS was almost zero. The assembled thin films exhibit transparency of up to 98% in the visible region due to porosities imparted through silica NPs, which is unlikely to have been the case in earlier reported results. The ageing of the thin film revealed that it can reduce the ice adhesion strength to 35% of the untreated surface, even after 100 days. Cyclic icing/deicing of the samples showed that the ice adhesion strength of the thin film after 50 cycles of icing/deicing is about five times lower than non-treated glass sample.

The behavior of the assembled SLIPS on a microfluidic device was evaluated to observe its effect on the hydrodynamic cavitation. It has been shown that presence of SLIPS on the surface of the channel is an effective method for earlier generation of cavitating flows, which is essential to decrease the input energy and increase the efficiency in microfluidic devices utilizing bubble clouds. The results show that the supercavitation condition is visible for all the microchannels for the D3 coating (with SLIPS), while this flow regime cannot be even recorded in some of the plain surface microchannels including the larger ones (e.g. CH2 and CH4). In addition, the supercavitation condition can be seen at a much lower upstream pressure for the D3 coating. The findings of this study will assist in facile cavitating flow generation with the aid of the cheap and facile surface modification techniques and utilization of cavitating flows in biomedical and energy applications. The low upstream pressures for intense cavitation generation expand the potential applications of hydrodynamic cavitation. Introducing the cellulose nanofiber-stabilized perfluoropentane droplets to the cavitating flow, which were tested within a surface tailored microfluidic device to generate cavitation bubbles in a facile way showed that the flow pattern with the highest intensity, i.e. supercavitation, was observed at a low upstream pressure of 1.7 MPa. As the CNFs are not damaged, droplets can be regenerated; this study proposes an important approach towards a closed-loop device that can store energy, then release and be “recharged” on demand.

5-2 Outlook

The facile, scalable, low cost and transparent SLIPS, which have been applied on the partially charged substrates using layer-by-layer technique, have developed the application fields for this type of films. The applying methods that have been used in this dissertation, enable the scientists to assemble SLIPS on any partially charge substrate regardless of the geometry, accessibility and the material type. The icephobic properties of SLIPS have been investigated in the first chapter of this thesis thoroughly. The high durability and transparency of these thin films showed that they can be used in harsh conditions like wind turbines, air planes wing and fuselage, windows of cars and buildings, and etc. For depositing SLIPS on large surfaces, layer-by-layer spray coating method is proposed.

The interactions of these surfaces with air bubbles and water within microfluidic devises showed that SLIPS can be used in the devices that are designed to separate gas and liquid. Based on the outcomes of this thesis a TUBITAK project has been proposed and accepted for a bubble separation device. “Engineering and Fabrication of Bubble / Gas Separation Filters Based on SLIPS Architecture” project has been accepted by TUBITAK to prepare a bubble separation device which its walls are coated by SLIPS to transport the separated bubbles to the exhaust pipe as show in the Figure 5-1 and Figure 5-2.

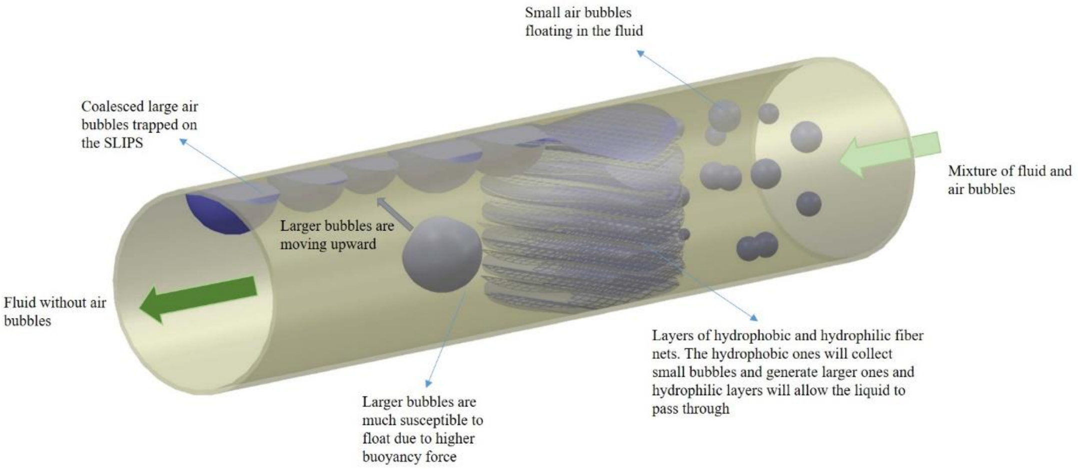

Figure 5-1 The trapping of air toward the walls of the tube and wrapping by the lubricant of the SLIPS

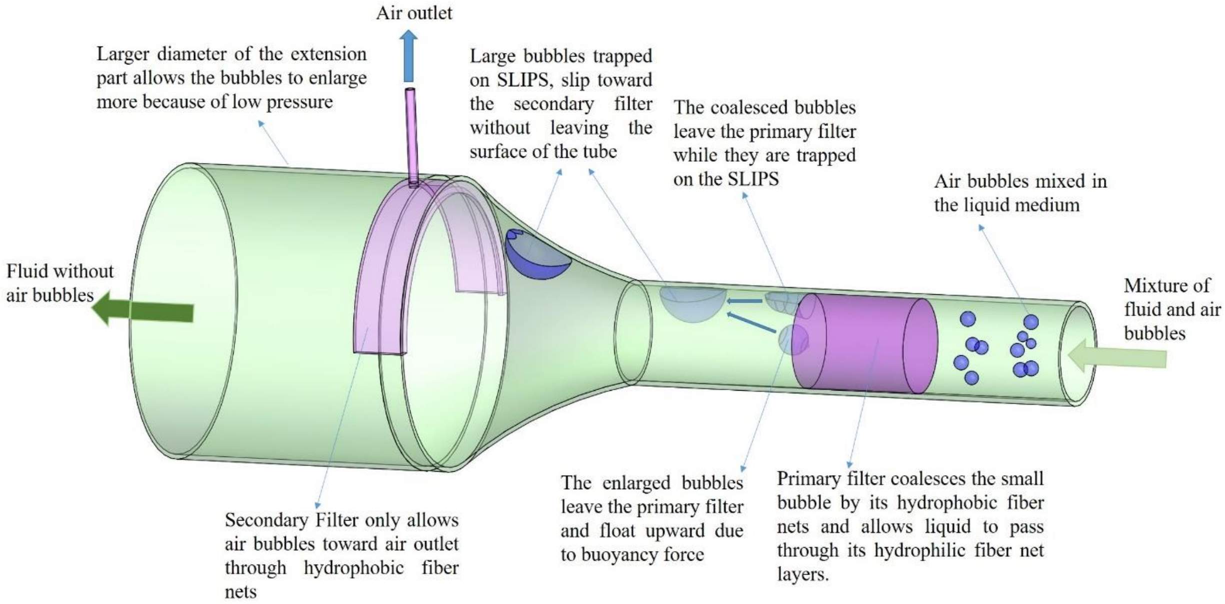

Figure 5-2 Schematic illustration of the mechanism of bubble separation and conduction process

5-3 Research Outcomes

- Aghdam, A. S., & Cebeci, F. Ç. (2020). Tailoring the Icephobic Performance of Slippery Liquid-Infused Porous Surfaces through the LbL Method. Langmuir, 36(46), 14145-14154, doi.org/10.1021/acs.langmuir.0c02873.
- Aghdam, A. S., Ghorbani, M., Deprem, G., Cebeci, F. Ç., & Koşar, A. (2019). A new method for intense cavitation bubble generation on layer-by-layer assembled slips. Scientific Reports, 9(1), 1-13, doi.org/10.1038/s41598-019-48175-4.
- Ghorbani, M., Aghdam, A. S., Gevari, M. T., Koşar, A., Cebeci, F. Ç., Grishenkov, D., & Svagan, A. J. (2020). Facile hydrodynamic cavitation ON CHIP via cellulose nanofibers stabilized perfluorodroplets inside layer-by-layer assembled SLIPS surfaces. Chemical Engineering Journal, 382, 122809, doi.org/10.1016/j.cej.2019.122809.
- Abbasiasl, T., Niazi, S., Aghdam, A. S., Chen, H., Cebeci, F. Ç., Ghorbani, M., Grishenkov, D. , Koşar, A. (2020). Effect of intensified cavitation using poly(vinyl alcohol) microbubbles on spray atomization characteristics in microscale. AIP Advances, 10(2), 025318. doi:10.1063/1.5142607.
- Araz Sheibani Aghdam; Deniz Koken; Fevzi C. Cebeci. Investigation of Ice Adhesion Strength on Novel Polyelectrolyte Thin Films Assembled by Layer By Layer Approach. 2017 MRS Fall Meeting, Boston, USA.
- Araz Sheibani Aghdam; Fevzi Ç. Cebeci. Investigation of The Relationship Between Contact Angle Hysteresis And Ice Adhesion Strength of Self-Assembled Icephobic Surfaces. 2017 13th Nanoscience & Nanotechnology Conference, Antalya, Turkey